Chapter 5

Results

5.1 Results of post-stack inversion methods

In this section, model based inversion (MBI), colored inversion (CI), maximum likelihood sparse spike inversion (MLSSI) and bandlimited inversion (BLI) derived results are discussed.

5.1.1 Model based inversion method

(i) Inversion analysis at well locations

A representative illustration of inversion analysis for one of the wells within F3 block is shown in Fig. 5.1, which represents the synthetic traces computed from the inverted P-impedance. Four wells were studied it to cover the entire block. The correlation coefficient (CC) between the seismic trace and synthetic trace is above 98% for all the four wells as represented in Fig. 5.2. This indicates high-quality input data. The high correlation coefficient indicates that the inversion parameters can be confidently employed to the entire seismic volume. The figure is labeled and self-explanatory. The extracted wavelet is clearly visible in blue color.

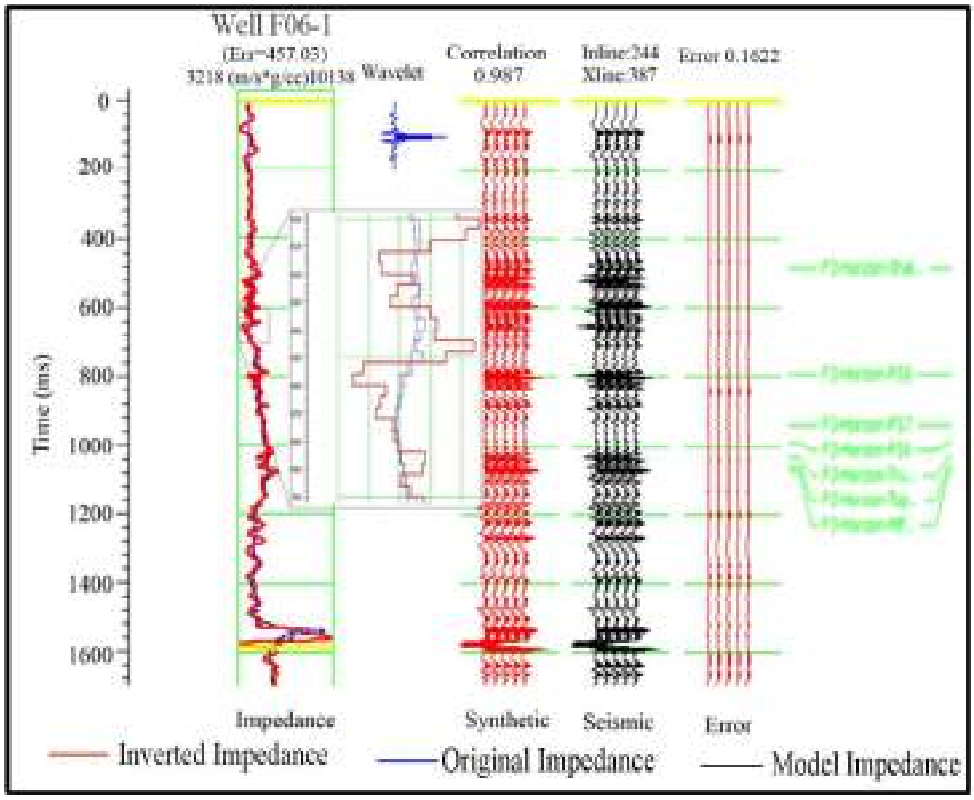

FIGURE 5.1: Inversion analysis results derived from MBI at well F06-1

For all wells, synthetic traces are generated and correlated with the seismic traces and the differences between them are measured. The correlation between seismic and synthetic trace indicated good relationships (Fig. 5.2) for all wells. The correlation coefficients are varying from 0.982 to 0.992. The residual errors are also estimated and it is varying from 232.50 (m/s*g/cc) to 457.03 (m/s*g/cc) shown in Fig. 5.3. Fig. 5.4 shows the synthetic relative error, which is varying from 0.1278 to 0.1877.

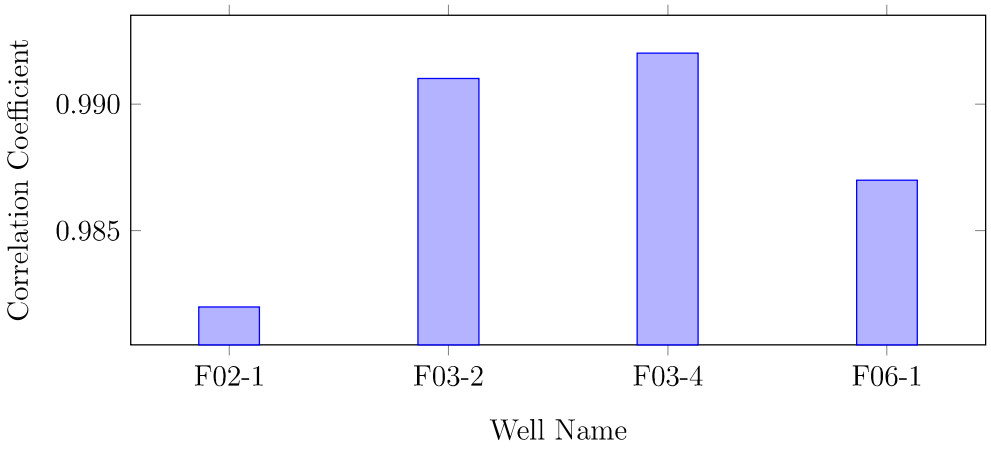

FIGURE 5.2: Variation of correlation coefficient for all wells obtained from MBI method

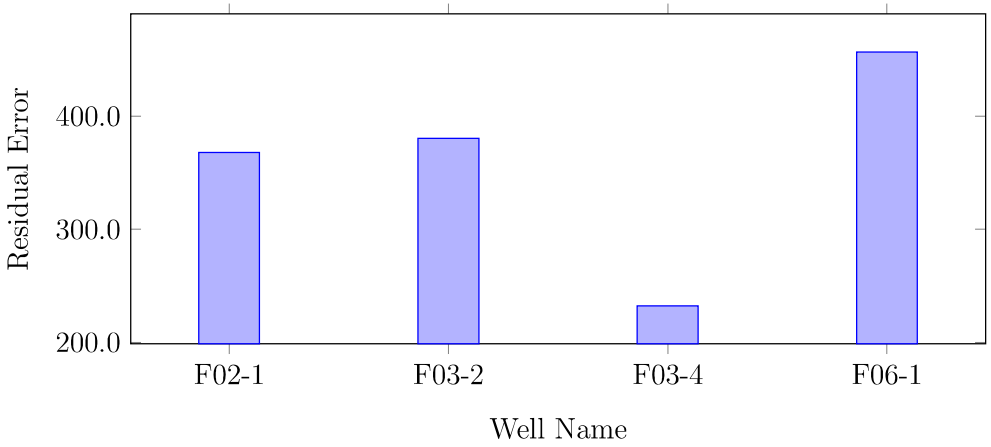

FIGURE 5.3: Variation of Residual Error for all wells obtained from MBI method

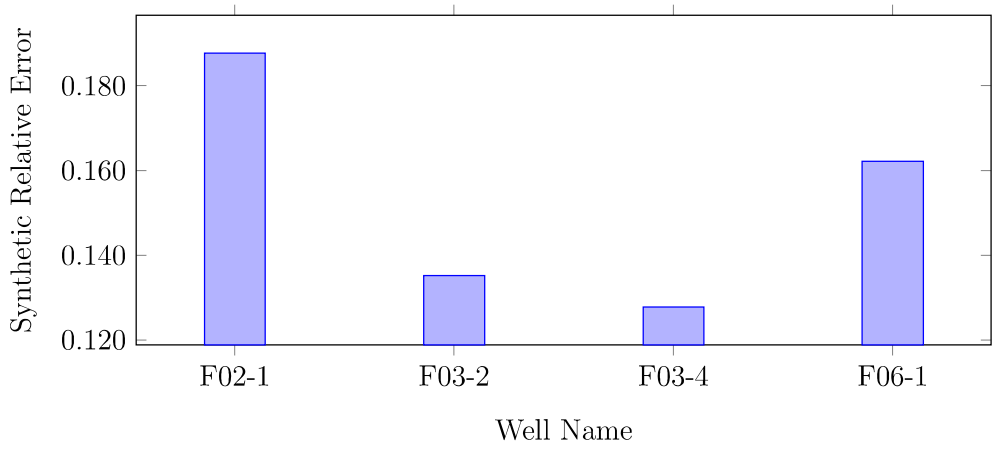

FIGURE 5.4: Variation of Synthetic Relative Error for all wells obtained from MBI method

(ii) Interpretation of results derived from MBI

A representative cross-section of MBI derived P-impedance is revealed in Fig. 5.5. The entire seismic section is inverted into P-impedance (only inline 244 is shown in Fig. 5.5 for simplicity). The impedance estimated from well F06-1(inline 244) is also shown in this figure for better comparison between inverted impedance and well log impedance. Both impedances are in good agreement. The fault planes are also visible in the same figure. A low impedance zone near 1700ms (as highlighted by an ellipse in the figure) level is clearly visible in Fig. 5.5.

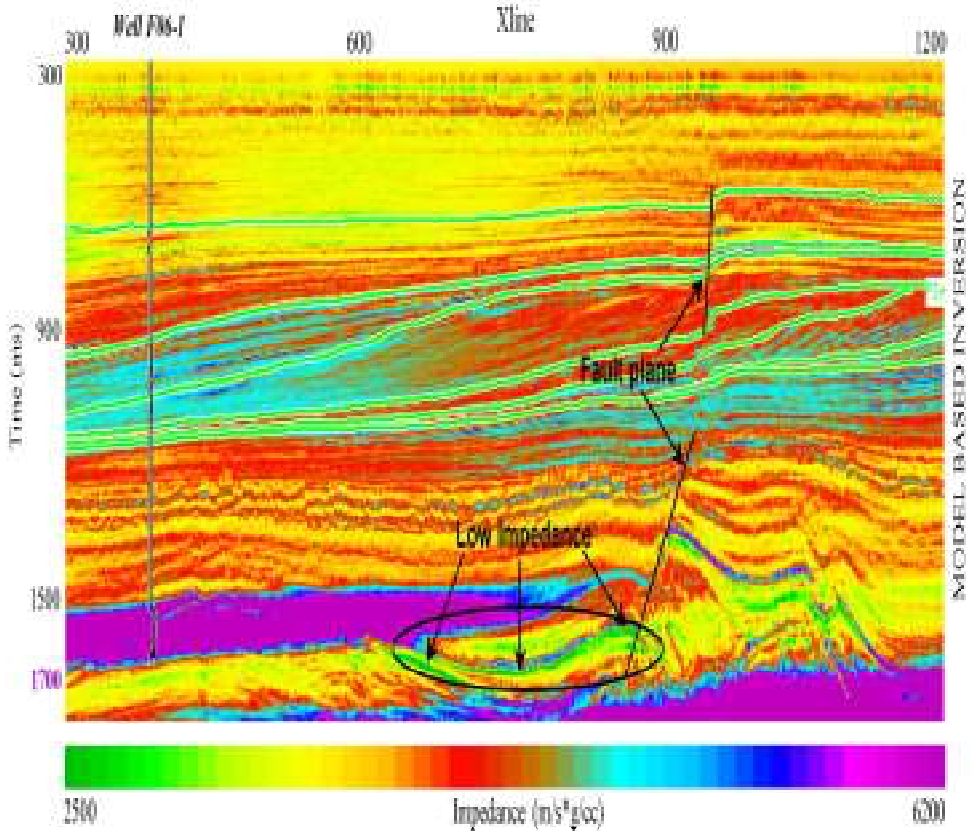

FIGURE 5.5: Cross-section (at Inline 244) of inverted P-impedance derived from MBI method

Fig. 5.6 shows the crossplot between original P-impedance and inverted P-impedance. The data points for all four wells are represented by different colors. The scatter data lies near to best fit line which reveals that the inverted results closely agree with the original results.

Fig. 5.7 shows a data slice at a 1700ms time interval. This figure demonstrates the horizontal variation of impedance at 1700ms two-way travel time. The ellipse highlights the low impedance zones.

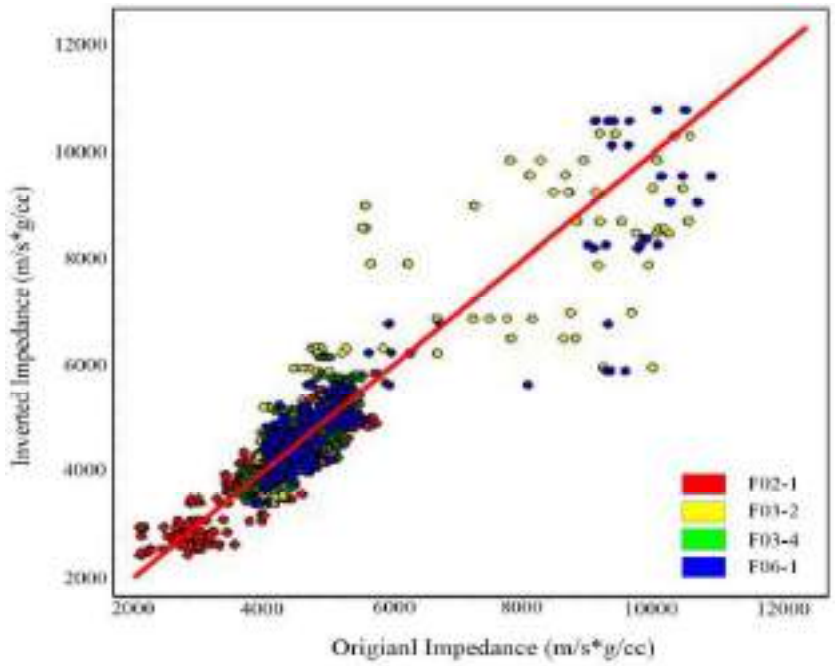

FIGURE 5.6: Crossplot between original P-impedance and predicted P-impedance obtained from MBI method

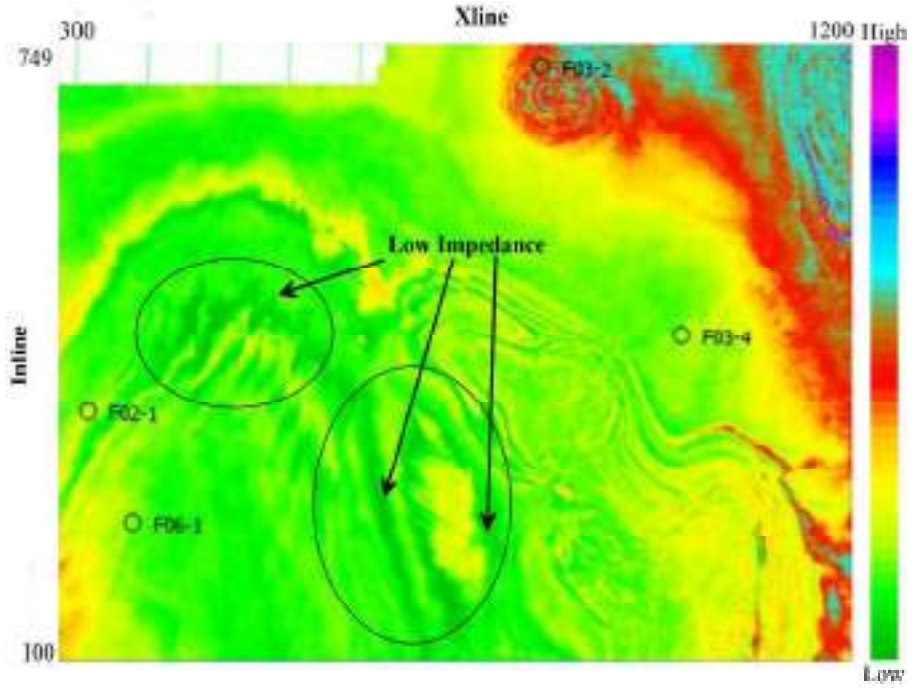

FIGURE 5.7: P-impedance slice centered at 1700ms obtained from MBI method

The seismic section amplitude spectra and MBI derived amplitude spectra are displayed in Fig. 5.8. Both the amplitude spectra do agree with each other for the entire frequency range. The correlation between synthetic derived from inverted amplitude and seismic section amplitude is 0.97.

Fig. 5.9 shows the 3D volume of P-impedance derived from MBI at a 1700ms time interval.

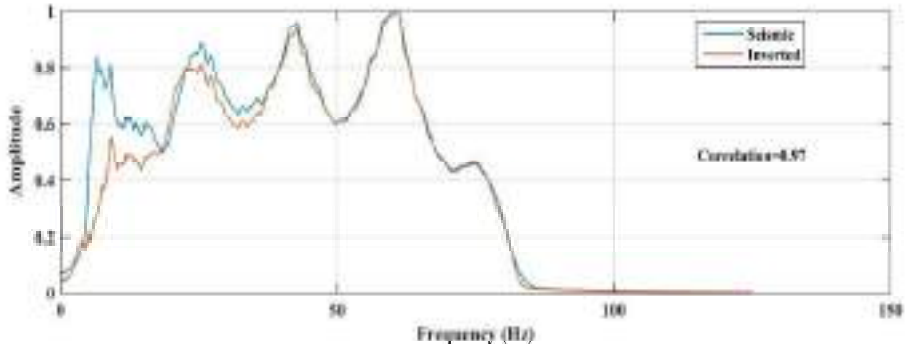

FIGURE 5.8: Comparison of amplitude spectra between seismic and MBI derived synthetic data

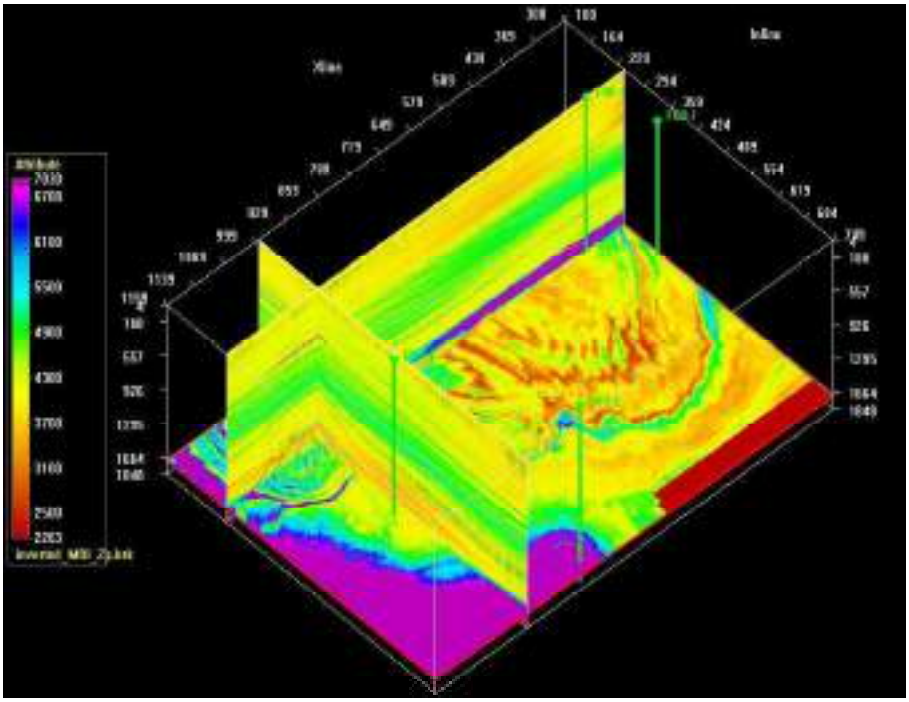

FIGURE 5.9: 3D volume of P-impedance obtained from MBI at 1700ms time interval

A simple method to measure the acoustic impedance is presented in the above section. This method can be employed for a fast evaluation of reservoir characteristics. Impedance volumes were estimated using MBI algorithms. The result shows that a consistent 3D acoustic impedance model can be configured if high-quality well logs and seismic data are available. The inverted result shows a very high correlation coefficient between seismic and synthetic data. The high correlation coefficient signifies that the inverted outcomes are decent and the estimated outcomes can be understood as a real subsurface model. Residual error and synthetic relative error were estimated and have been found to be very low. A low impedance zone has been found in between 1680ms and 1700ms two-way travel time which is interpreted as an anomalous zone. The impedance of the anomalous zone has been varied from 2500 to 6200 (m/s*g/cc) which indicates very low values. A data slice at 1700ms time shows the variation of this anomalous zone in the subsurface. The inverted amplitude spectrum derived synthetic and amplitude spectrum of the seismic section agree for the entire frequency range, which shows that the frequency is not distorted by MBI method. The crossplot between original P-impedance and predicted impedance has revealed the good performance of MBI in estimating the anomalous zone.

5.1.2 Colored inversion method

(i) Inversion analysis at well locations

CI method has been implemented for all the wells existing in the study region. A representative Fig. 5.10 represents inverted findings for one well F06-1. The correlation coefficient between the seismic trace and synthetic trace is above 72% for all the four wells as represented in Fig. 5.11. This indicates high-quality input data. The high correlation coefficient indicates that the inversion parameters can be confidently employed to the entire seismic volume. The figure has been labelled and is self-explanatory. The extracted wavelet is highlighted in blue.

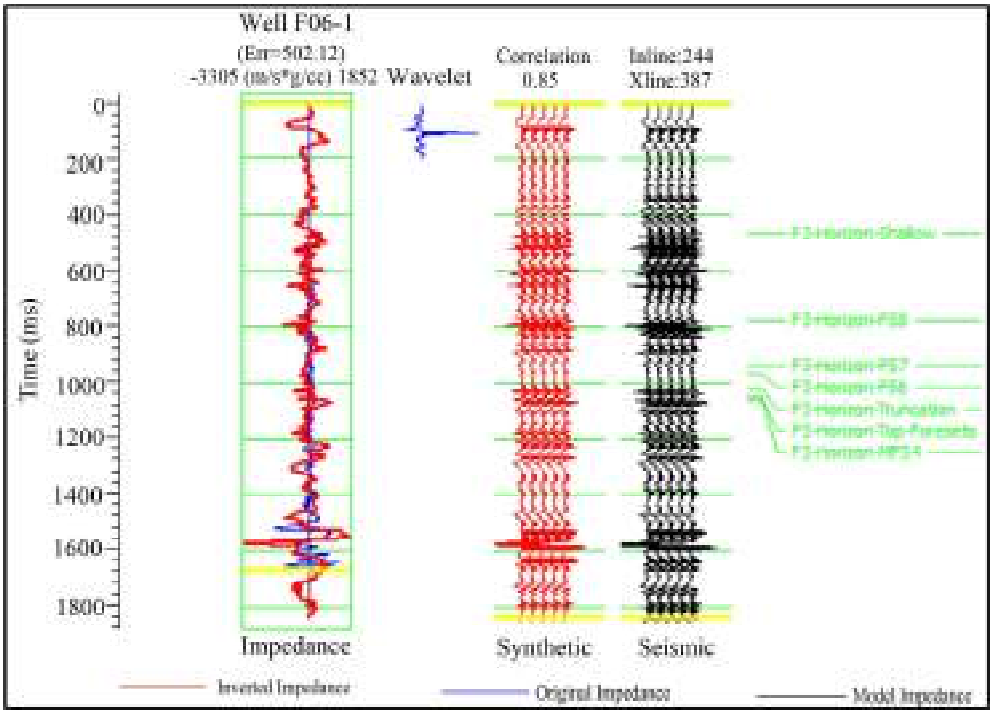

FIGURE 5.10: Inversion analysis results derived from CI method at well F06-1

The synthetic trace extracted at each borehole location is compared with seismic impedance as well as the correlation coefficients are determined along with the error. The correlation between the seismic and synthetic trace indicated good relationships (Fig. 5.11) for all wells. The correlation coefficients (CC) are varying from 0.72 to 0.88. The residual errors are also estimated and it is varying from 404.86 (m/s*g/cc) to 612.50 (m/s*g/cc) shown in Fig. 5.12.

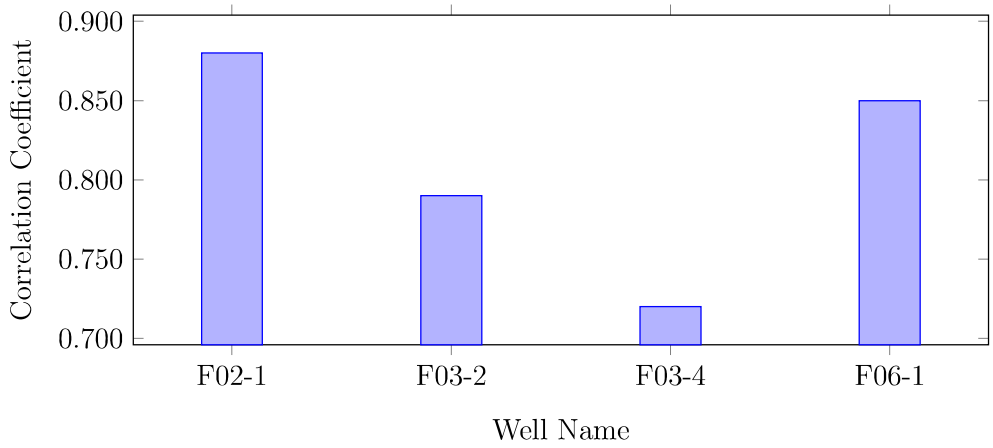

FIGURE 5.11: Variation of correlation coefficient for all boreholes obtained from CI method

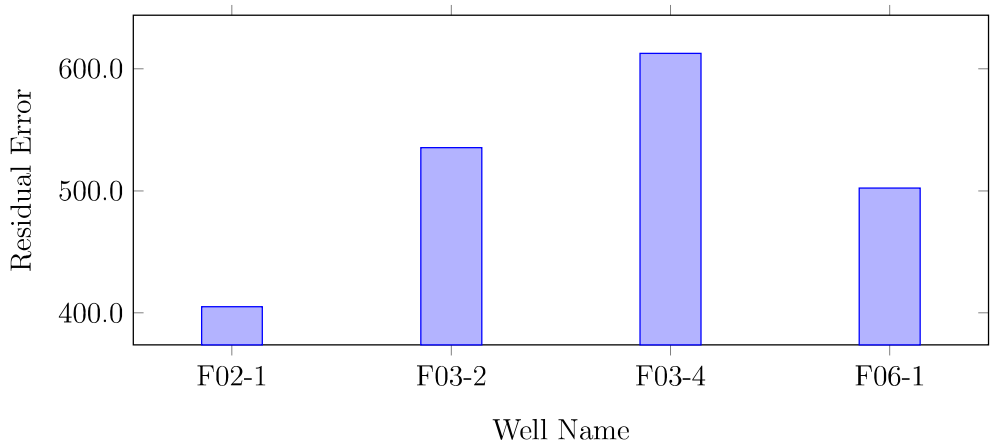

FIGURE 5.12: Residual Error variation for all boreholes obtained from CI method

(ii) Interpretation of results derived from CI

A representative cross-section of CI derived P-impedance is revealed in Fig. 5.13. The entire seismic section is inverted into P-impedance (only inline 244 is shown in Fig. 5.13 for simplicity). The impedance estimated from well F06-1(inline 244) is also shown in this figure for better comparison between inverted impedance and well log impedance. Both impedances are in good agreement. The fault planes are also visible in the same figure. A low impedance zone near 1700ms (as highlighted by an ellipse in the figures) level is clearly visible in Fig. 5.13.

Fig. 5.14 shows the crossplot between original P-impedance and inverted P-impedance. The data points for all four wells is represented by different colors. The scatter data lies near to best fit line which reveals that the inverted results closely agree with the original results.

Fig. 5.15 shows a data slice at a 1700ms time interval. This figure demonstrates a horizontal variation of impedance at 1700ms two-way travel time. The ellipse highlights the low impedance zones.

The seismic section amplitude spectra and CI derived amplitude spectra are displayed in Fig. 5.16. Both the amplitude spectra do agree with each other for the entire frequency range. The correlation between synthetic derived from inverted amplitude and seismic section amplitude is 0.92. The correlation between synthetics derived from inverted P-impedance and seismic section amplitude is 0.92 which is less than MBI. In the algorithm, the inability to agree may be due to the use of an operator in place of a wavelet. An operator simply convolves with the seismic data to produce the volume of impedance while the wavelet is precisely derived from well log and seismic data, allowing it more accurate for its use.

Fig. 5.17 shows a 3D volume of P-impedance derived from CI method at a 1700ms time interval.

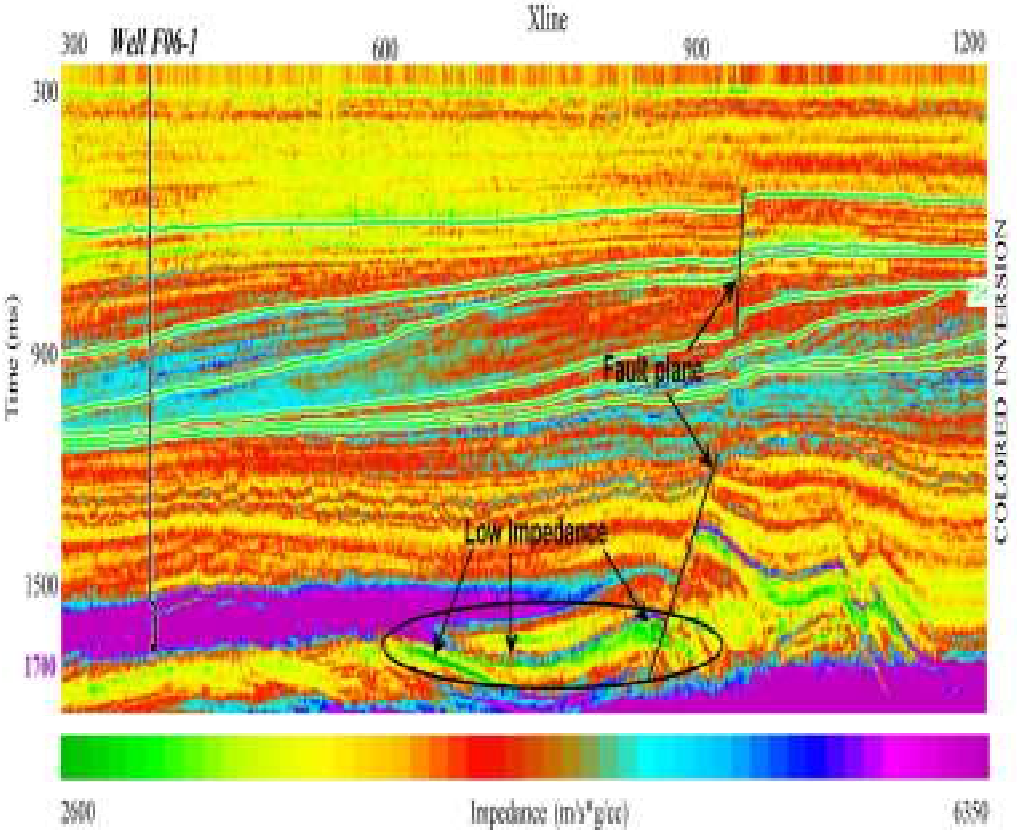

FIGURE 5.13: Cross-section of inverted P-impedance volume (at inline 244) using CI method

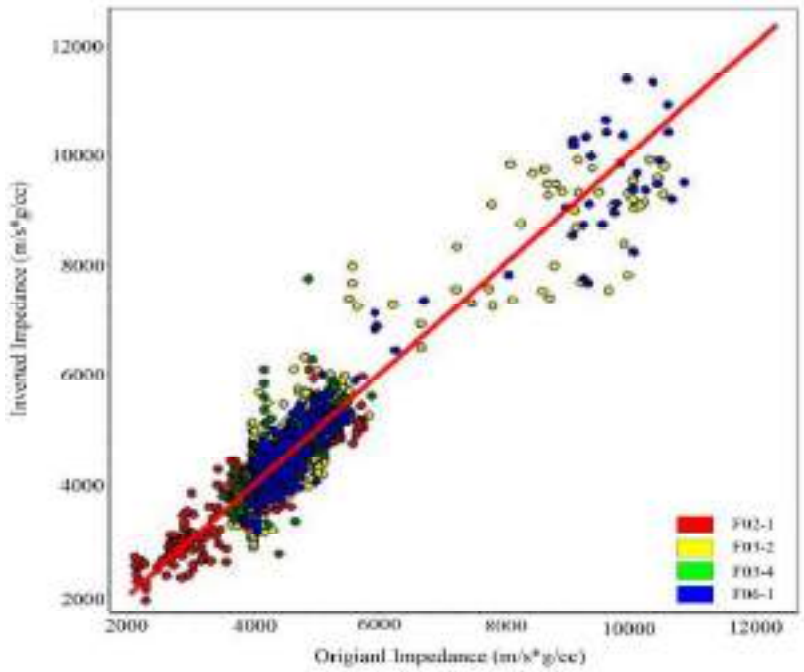

FIGURE 5.14: Crossplot between original P-impedance and predicted impedance using CI method

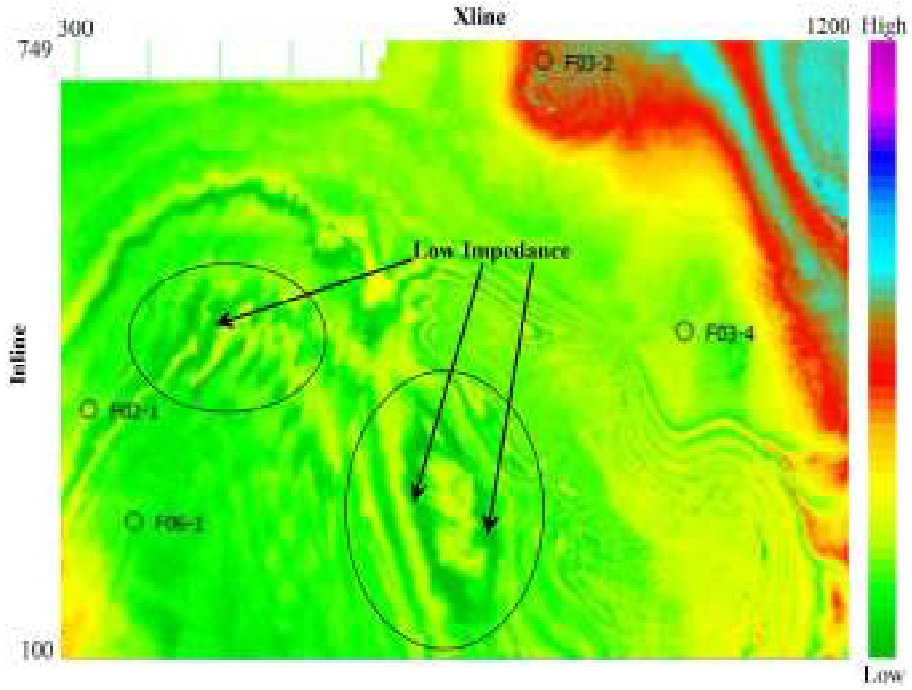

FIGURE 5.15: Data slice for inverted P-impedance derived from CI method at 1700ms time interval

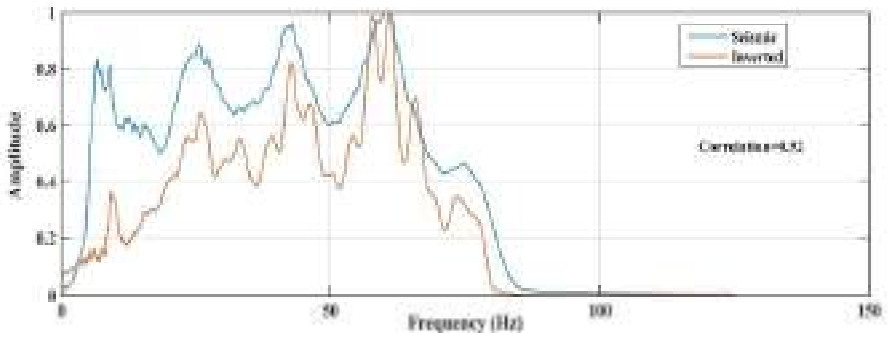

FIGURE 5.16: Comparison of amplitude spectra between seismic and CI derived synthetic data

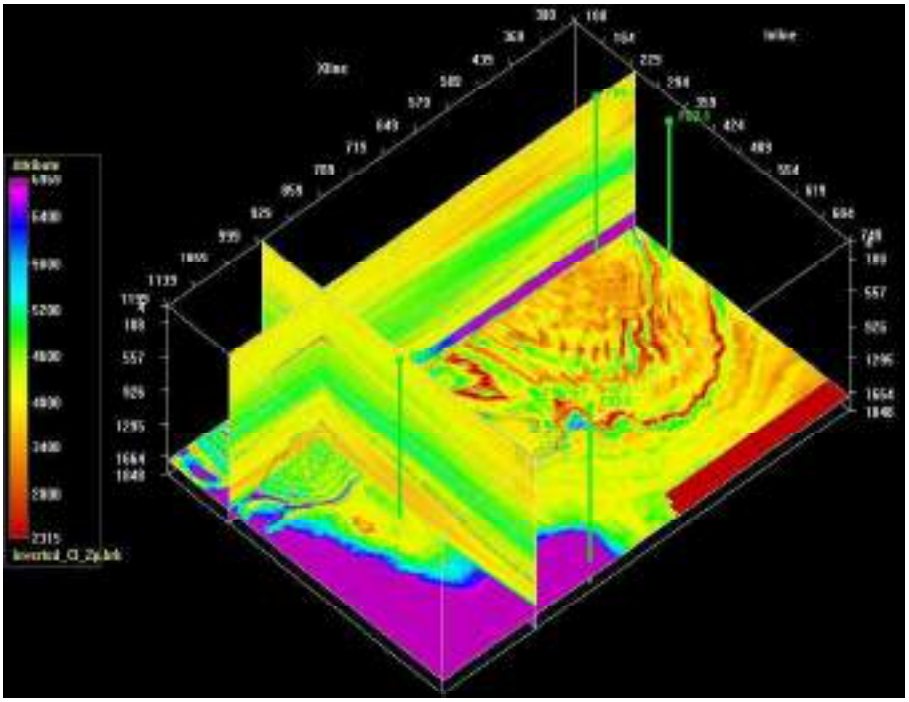

FIGURE 5.17: 3D volume of P-impedance derived from CI method at 1700ms time interval

CI method estimated the low-impedance values within reservoir zones ranging from 2600 to 6350(m/s*g/cc) which confirmed the existence of an anomalous zone. The acoustic impedance variation slice along all inline and crossline illustrated the existence and low impedance distribution between 1680ms and 1700ms two-way travel time which is interpreted as an anomalous zone. The estimated impedance volume shows a high-resolution subsurface image as compared to the seismic data. In addition,

the difference between seismic section amplitude spectra and synthetics derived from inverted P-impedance may be due to the use of an operator in place of a wavelet. The CC between inverted and seismic amplitude spectra is 0.92. A data slice at 1700ms time shows the variation of this anomalous zone in the subsurface. The inverted amplitude spectrum derived synthetic and amplitude spectrum of the seismic section agree for the entire frequency range, which shows that the frequency is not distorted by CI method. The crossplot between original P-impedance and predicted impedance has revealed the good performance of CI in estimating the anomalous zone.

5.1.3 Maximum likelihood sparse spike inversion method

(i) Inversion analysis at well location

A representative illustration of inversion analysis results derived from MLSSI method for one of the wells (F06-1) within the F3 block is shown in Fig. 5.18. Four wells were studied to cover the entire block. Using the inverted P-impedance at the well location, a synthetic seismic trace is generated and correlated with the seismic section data near the well location. The correlation coefficient between the seismic trace and synthetic trace is above 86% for all the four wells as represented in Fig. 5.19. This indicates high-quality input data. The high correlation coefficient indicates that the inversion parameters can be confidently employed to the entire seismic volume. The illustration is clearly labelled and self-explanatory. In blue, the extracted wavelet can be seen clearly.

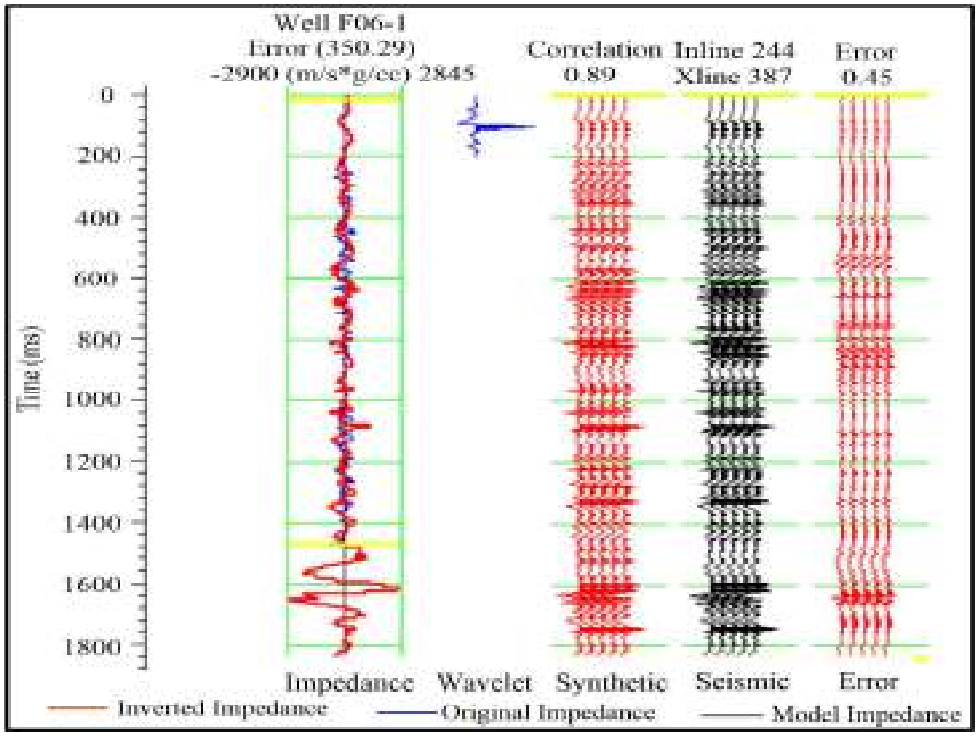

FIGURE 5.18: Inversion analysis results derived from MLSSI method at well F06-1

For all wells, synthetic traces are generated and correlated with the seismic traces and the differences between them are measured. The correlation between the seismic and synthetic trace indicated good relationships (Fig. 5.19) for all wells. The correlation coefficients are varying from 0.86 to 0.93. The residual errors are also estimated and it is varying from 375.56 (m/s*g/cc) to 361.39 (m/s*g/cc) shown in Fig. 5.20. Fig. 5.21 shows the synthetic relative error, which is varying from 0.37 to 0.49.

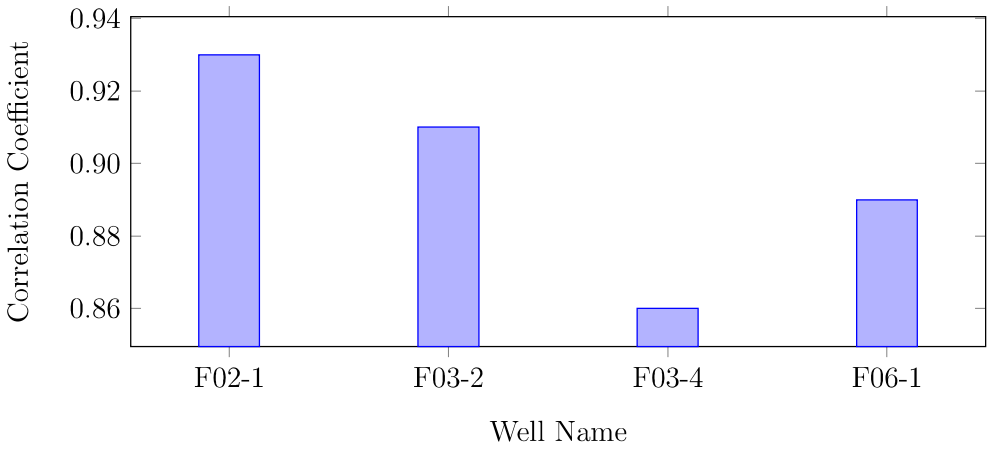

FIGURE 5.19: Variation of the correlation coefficient for all wells obtained from MLSSI method

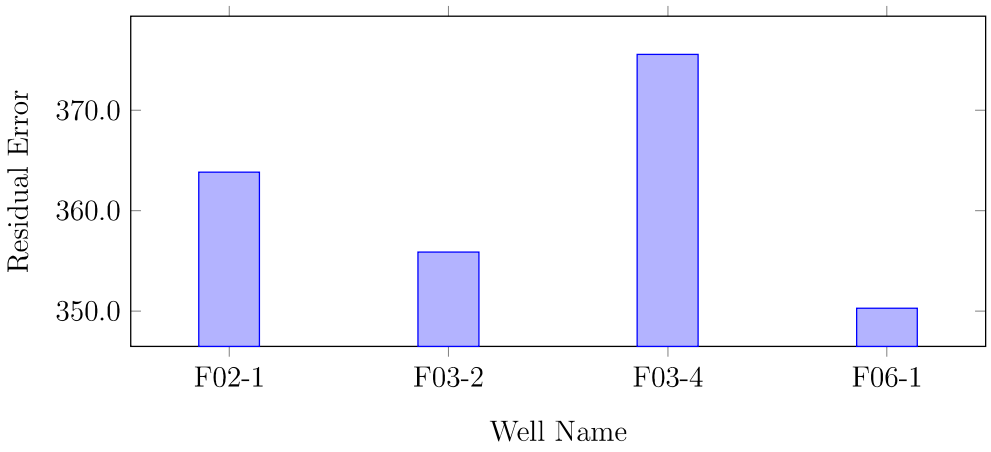

FIGURE 5.20: Residual Error variation for all boreholes obtained from MLSSI method

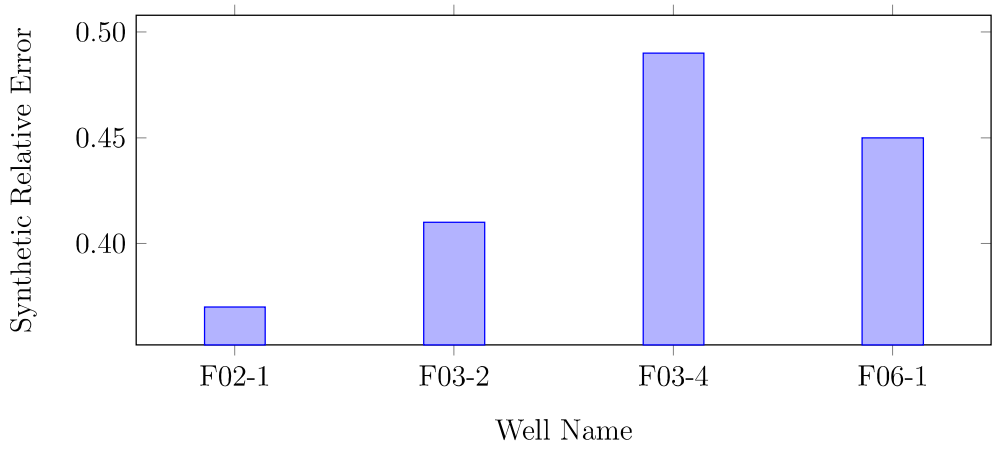

FIGURE 5.21: Synthetic Relative Error variation for all boreholes obtained from MLSSI method

(ii) Interpretation of results derived from MLLSI

A representative cross-section of MLSSI derived P-impedance is revealed in Fig. 5.22. The entire seismic section is inverted into P-impedance (only inline 244 is shown in Fig. 5.22 for simplicity). The impedance estimated from well F06-1(inline 244) is also shown in this figure for better comparison between inverted impedance and well log impedance. Both impedances are in good agreement. The fault planes are also visible in the same figure. A low impedance zone near 1700ms (as highlighted by an ellipse in the figures) level is clearly visible in Fig. 5.22.

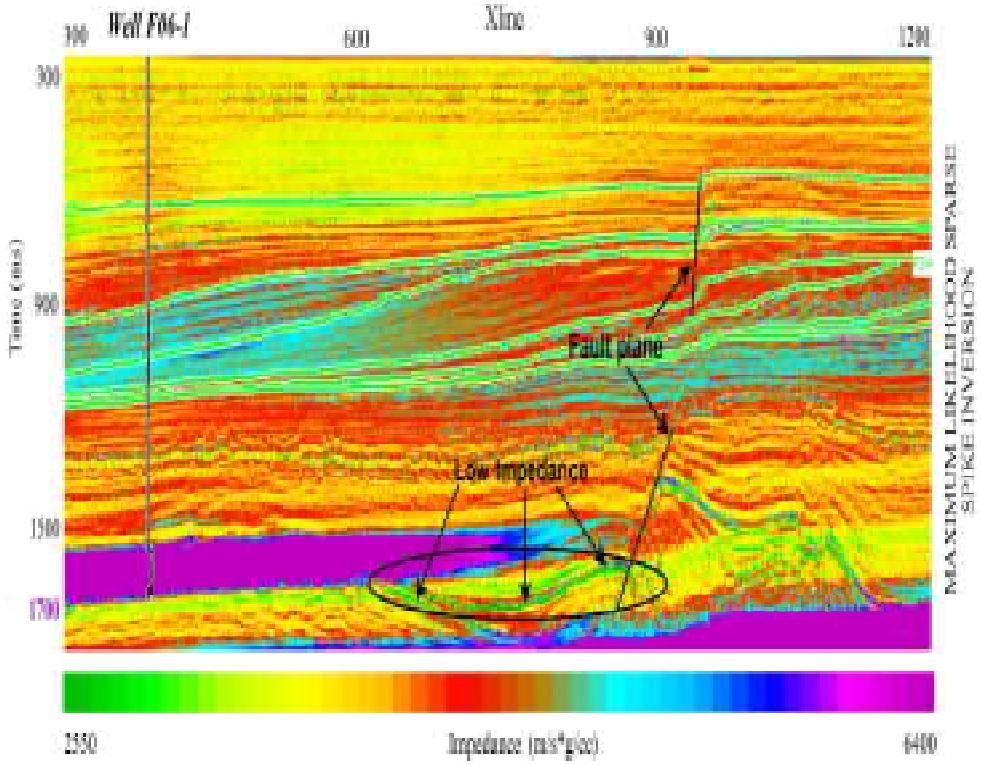

FIGURE 5.22: Inverted P-impedance cross-section (at Inline 244) is generated using MLSSI method

Fig. 5.23 shows the crossplot between original P-impedance and inverted P-impedance. The data points for all four wells is represented by different colors. The scatter data lies near to best fit line which reveals that the inverted results closely agree with the original results.

Fig. 5.24 shows a data slice at a 1700ms time interval. This figure demonstrates a horizontal variation of impedance at 1700ms two-way travel time. The ellipse highlights the low impedance zones.

The seismic section amplitude spectra and MLSSI derived amplitude spectra are displayed in Fig. 5.25. Both the amplitude spectra do agree with each other for the entire frequency range. The correlation between synthetic derived from inverted amplitude and seismic section amplitude is 0.97.

Fig. 5.26 shows a 3D volume of P-impedance derived from MLSSI at a 1700ms time interval.

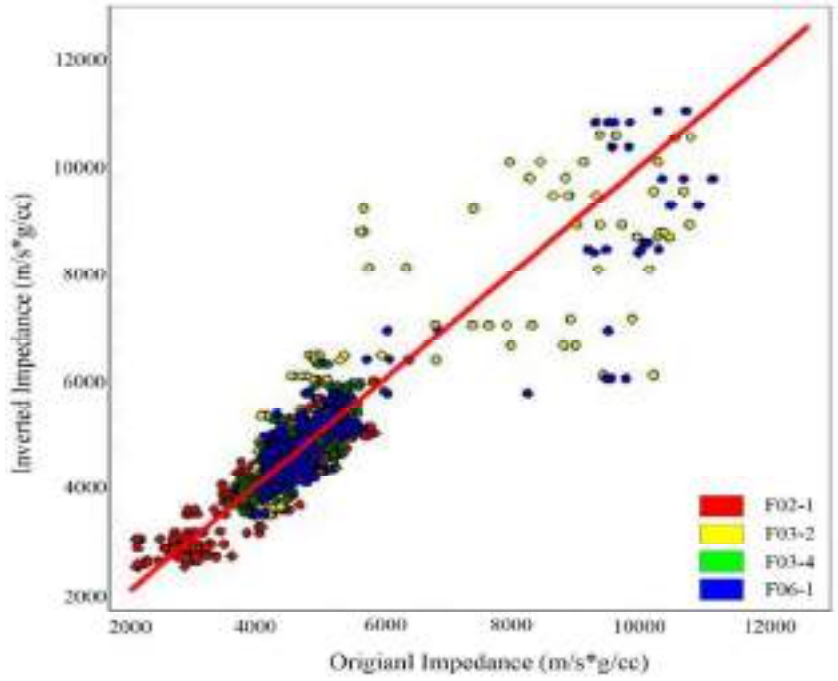

FIGURE 5.23: Crossplot between original P-impedance and inverted P-impedance obtained from MLSSI method

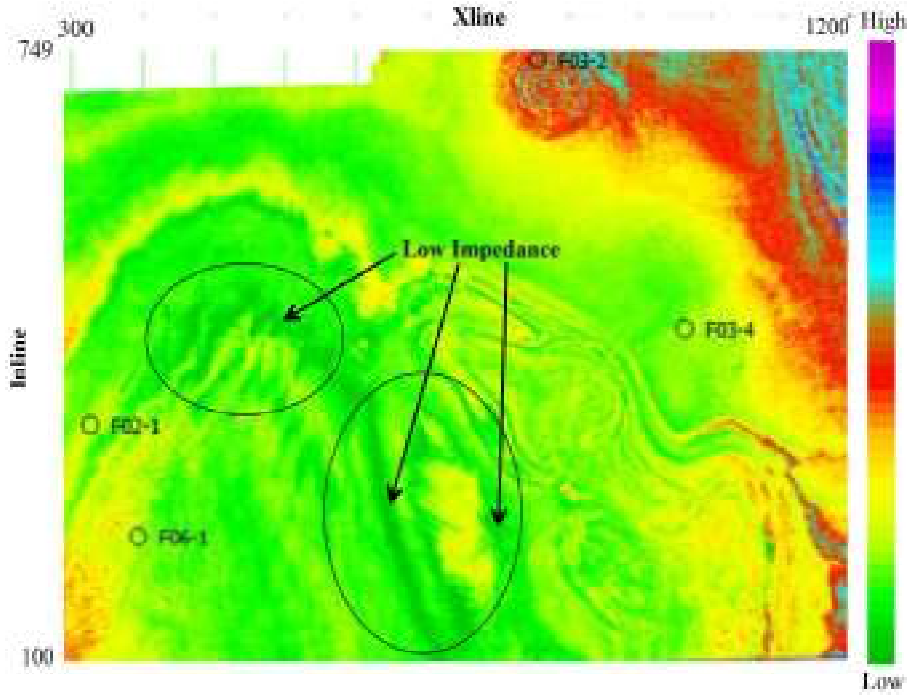

FIGURE 5.24: Data slice for MLSSI derived P-impedance at 1700ms time interval

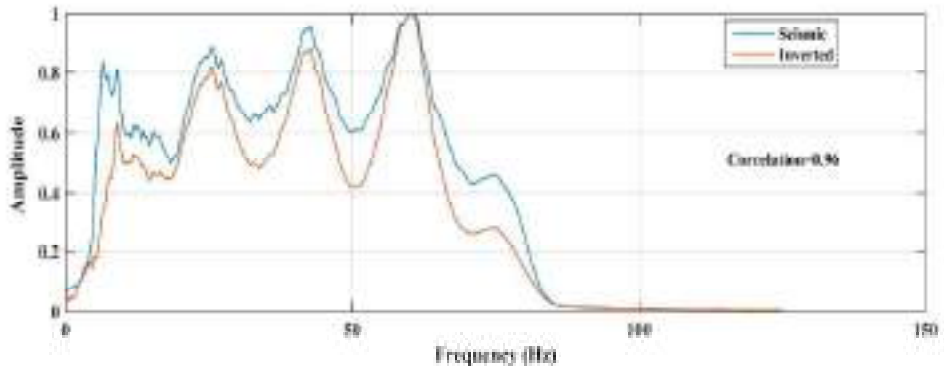

FIGURE 5.25: Comparison of amplitude spectra between seismic and MLSSI derived synthetic data

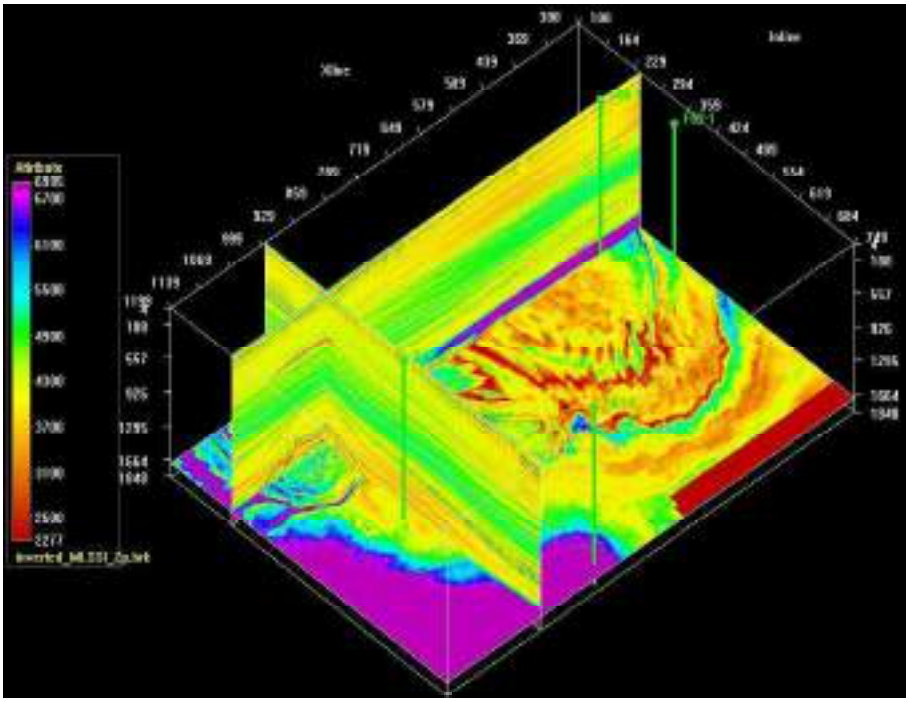

FIGURE 5.26: 3D volume of P-impedance derived from MLSSI method at 1700ms time interval

The inverted result shows a very high CC between seismic and synthetic data. The high correlation coefficient signifies that the inverted outcomes are decent and the estimated outcomes can be understood as a real subsurface model. Residual error and synthetic relative error were estimated and have been found very low. A low impedance zone has been found in between 1680ms and 1700ms two-way travel time which is interpreted

as an anomalous zone. The impedance of the anomalous zone is varying from 2550 to 6400 (m/s*g/cc) which indicates very low values. A data slice at 1700ms time shows the variation of this anomalous zone in the subsurface. The inverted amplitude spectrum derived synthetic and amplitude spectrum of the seismic section agree for the entire frequency range, which shows that the frequency is not distorted by MLSSI method. The crossplot between original P-impedance and predicted impedance has revealed the good performance of MLSSI in estimating the anomalous zone.

5.1.4 Band limited inversion method

(i) Inversion analysis at well locations

A representative illustration of inversion analysis results derived from BLI for one of the wells within the F3 block is shown in Fig. 5.27, which represents the synthetic traces computed from the inverted P-impedance. Four wells were studied to cover the entire block. The correlation coefficient between the seismic trace and synthetic trace is above 87% for all the four wells as represented in Fig. 5.28. This indicates high-quality input data. The high correlation coefficient indicates that the inversion parameters can be confidently employed to the entire seismic volume. The figure has been labelled and is self-explanatory. The extracted wavelet is clearly visible in the blue.

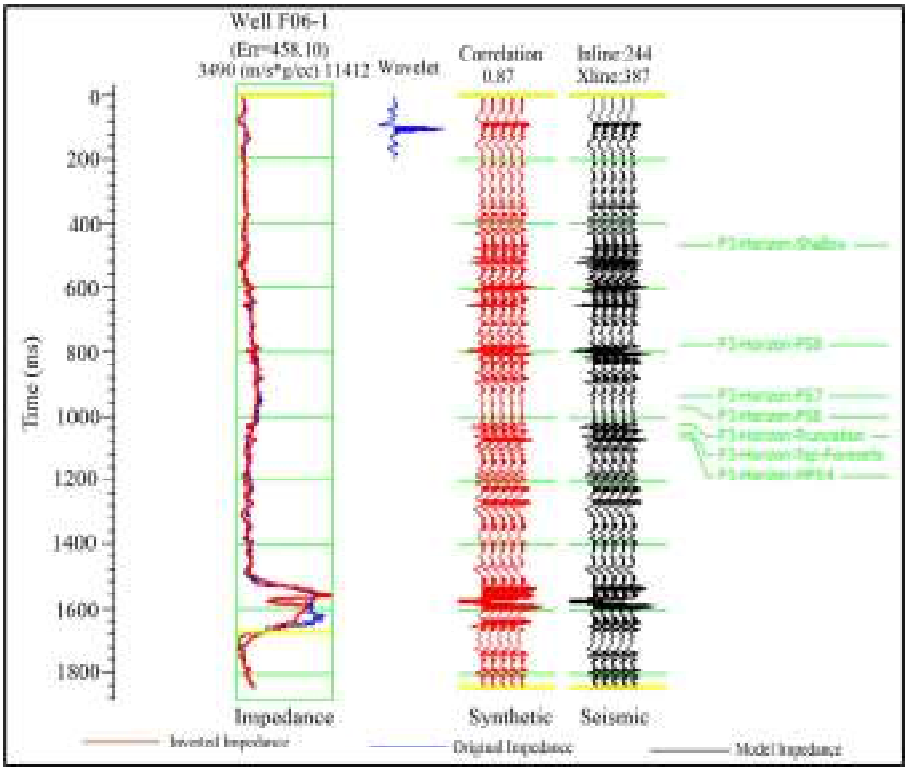

FIGURE 5.27: Inversion analysis results derived from BLI method at well F06-1

For all wells, synthetic traces are generated and correlated with the seismic traces and the differences between them are measured. The correlation between the seismic and synthetic trace indicated good relationships (Fig. 5.28) for all wells. The correlation coefficients are varying from 0.85 to 0.90. The residual errors are also estimated and it is varying from 375.56 (m/s*g/cc) to 539.08 (m/s*g/cc) shown in Fig. 5.29.

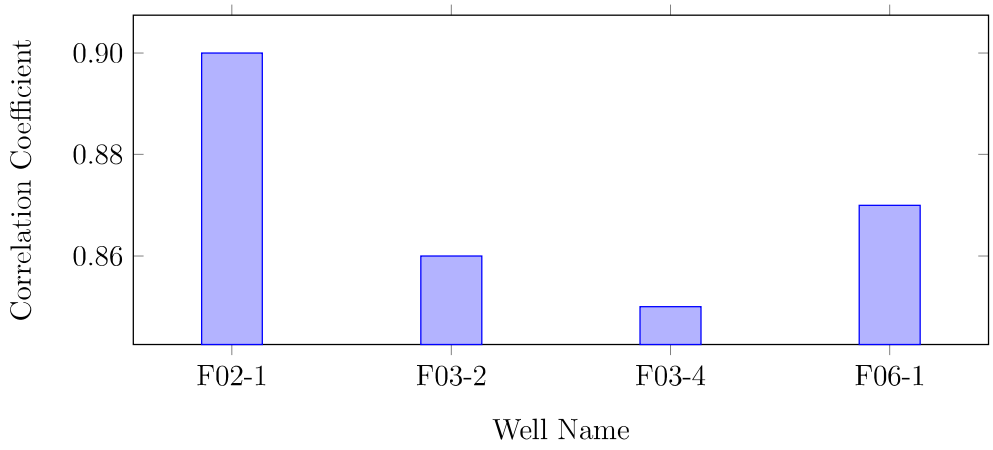

FIGURE 5.28: Variation of Correlation coefficient for all boreholes derived from BLI method

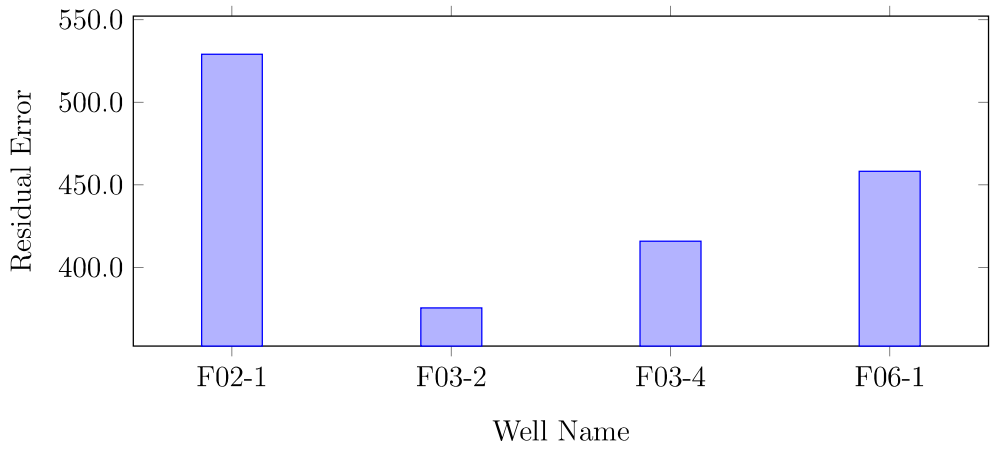

FIGURE 5.29: Residual error variation for all boreholes derived from BLI method

(ii) Interpretation of results derived from BLI

A representative cross-section of BLI derived P-impedance is revealed in Fig. 5.30. The entire seismic section is inverted into P-impedance (only inline 244 is shown in Fig. 5.30 for simplicity). The impedance estimated from well F06-1(inline 244) is also shown in this figure for better comparison between inverted impedance and well log impedance. Both impedances are in good agreement. The fault planes are also visible in the same figure. A low impedance zone near 1700ms (as highlighted by an ellipse in the figure) level is clearly visible in Fig. 5.30.

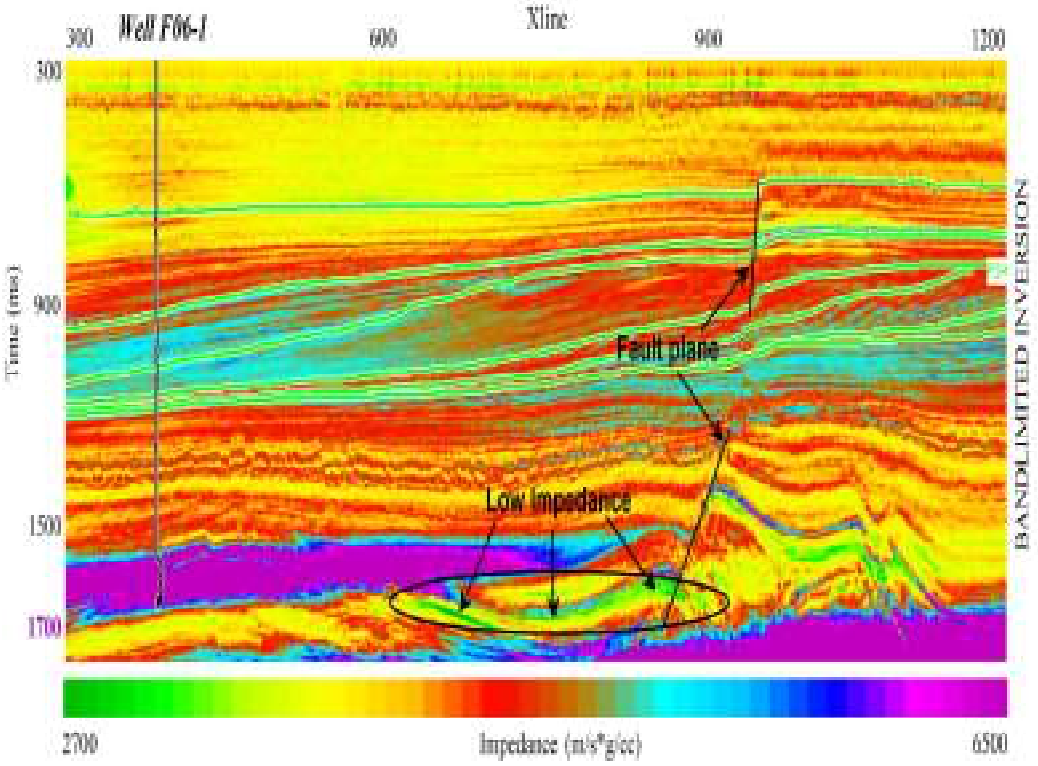

FIGURE 5.30: Inverted P-impedance cross-section derived from BLI method (at Inline 244)

Fig. 5.31 shows the crossplot between original P-impedance and inverted P-impedance. The data points for all four wells are represented by different colors. The scatter data lies near to best fit line which reveals that the inverted results closely agree with the original results.

Fig. 5.32 shows a data slice at a 1700ms time interval. This figure demonstrates a horizontal variation of impedance at 1700ms two-way travel time. The ellipse highlights the low impedance zones.

The seismic section amplitude spectra and BLI derived amplitude spectra are displayed in Fig. 5.33. Both the amplitude spectra do agree with each other for the entire frequency range. The correlation between synthetic derived from inverted amplitude and seismic section amplitude is 0.95 which is greater than CI but less than MBI and MLSSI.

Fig. 5.34 shows the 3D volume of P-impedance derived from MBI at a 1700ms time interval.

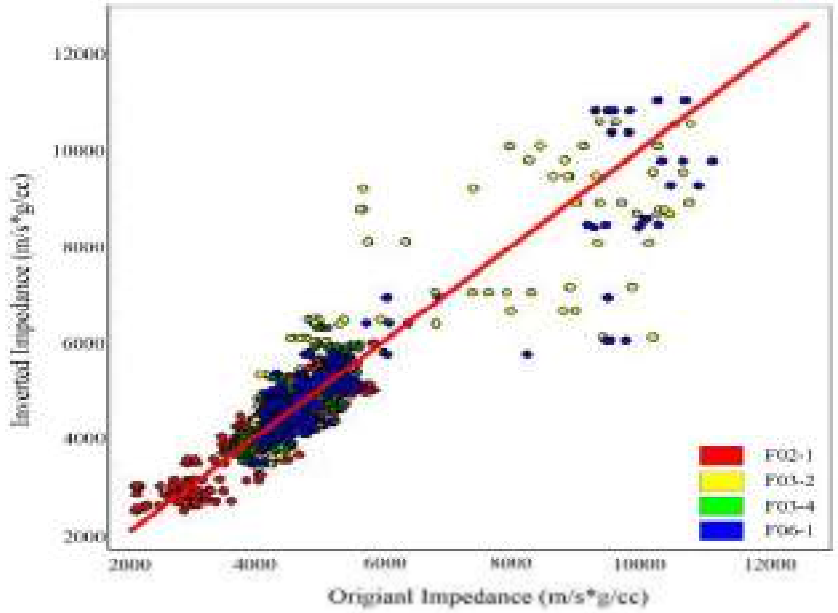

FIGURE 5.31: Crossplot between original P-impedance and inverted P-impedance derived from BLI method

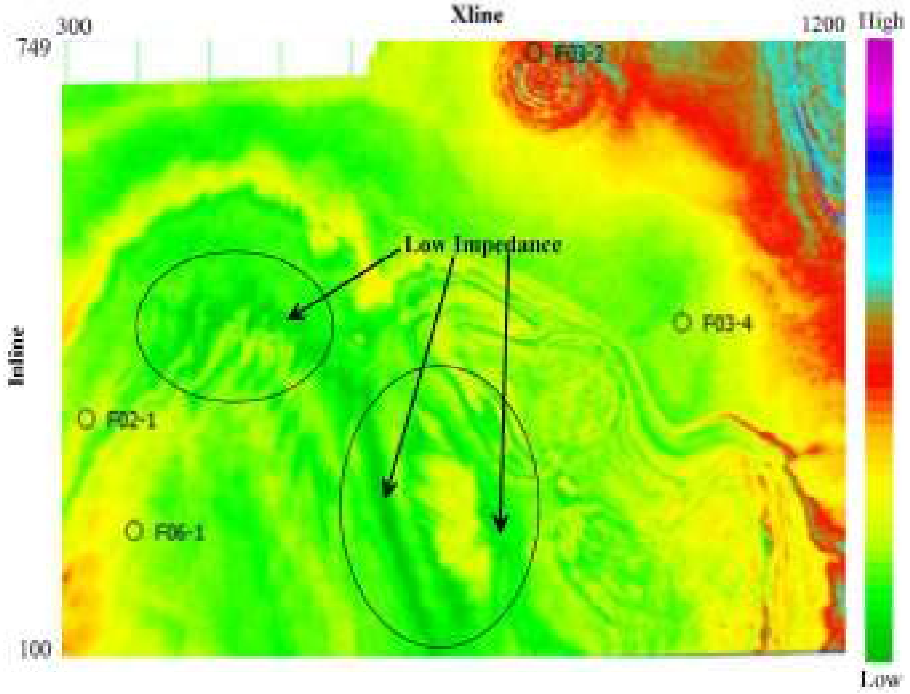

FIGURE 5.32: Data slice for BLI derived P-impedance at 1700ms time interval

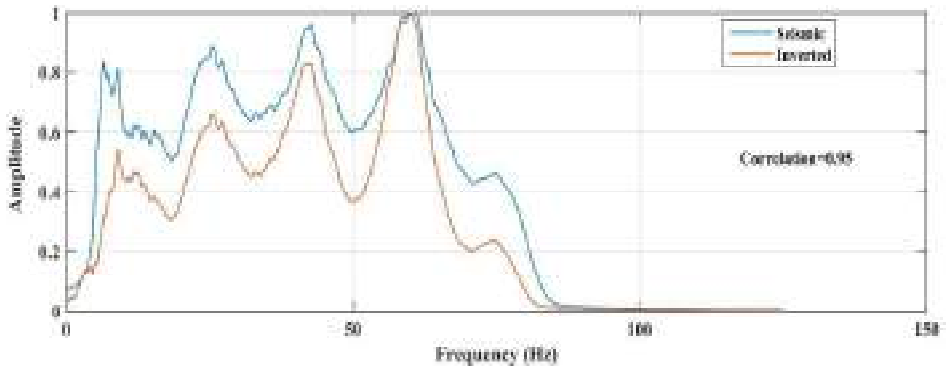

FIGURE 5.33: Comparison of amplitude spectra between seismic and BLI derived synthetic data

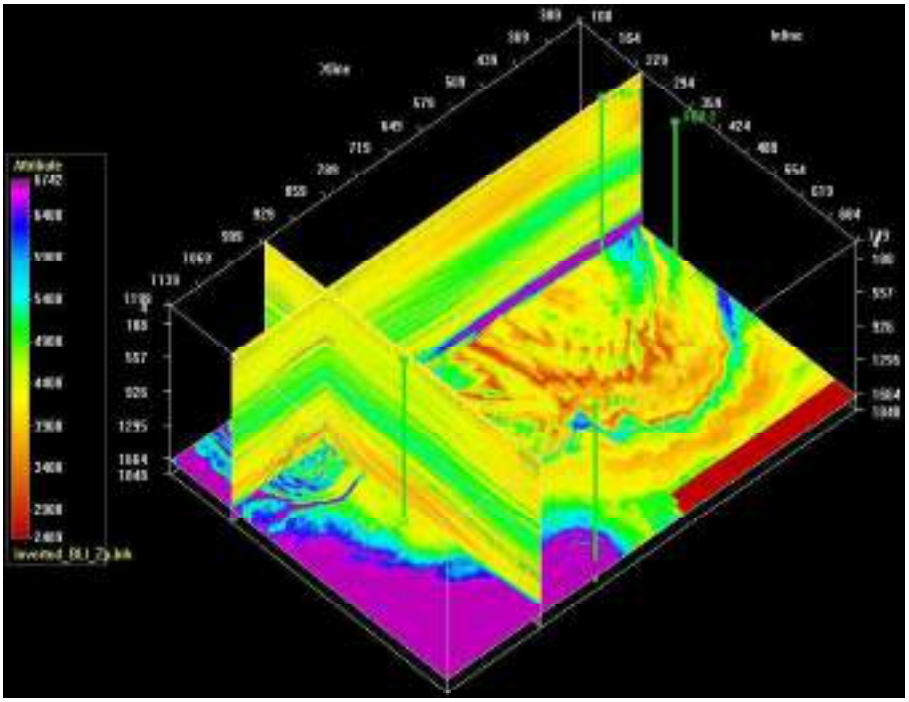

FIGURE 5.34: 3D volume of inverted P-impedance derived from BLI method at 1700ms time interval

BLI method has also been used to perform for estimation of P-impedance volume. The residual error has been estimated and found to be very low. A low impedance zone has been found in between 1680ms and 1700ms two-way travel time which is interpreted as an anomalous zone. The impedance of the anomalous zone is varying from 2700 to 6500 (m/s*g/cc) which indicates very low values. A data slice at 1700ms time

shows the variation of this anomalous zone in the subsurface. The inverted amplitude spectrum derived synthetic and amplitude spectrum of the seismic section agree for all the frequency ranges, which shows that the frequency is not distorted by BLI method. The crossplot between original impedance and predicted impedance has revealed the good performance of BLI in estimating the anomalous zone.

5.2 Results derived from pre-stack inversion methods

In this section, Penobscot 3D pre-stack data has been used for analysis. The Penobscot survey field exists on the Scotian shelf in offshore Nova Scotia, Canada. For the analysis, 200 (1200-1400) inline and 40(1161-1200) crossline has been used from the entire data.

Pre-stack inversion of seismic data for estimating elastic properties of the subsurface has been applied for seismic exploration studies. Non-uniqueness and Non-linearity, along with rigorous forward modeling techniques, make the problem challenging and difficult to solve. Pre-stack seismic waveform inversion (also sometimes referred to as Simultaneous Inversion) computes two or more lithological volumes simultaneously. The typical outcomes of this process are acoustic impedance (Z_P), shear impedance (Z_S), density (ρ), Compressional wave velocity (V_P), Shear-wave velocity (V_S) and V_P/V_S ratio. Seismic data used for pre-stack inversion have to be conditioned to eliminate as various unwanted effects. The random noise, NMO wavelet stretch, and non-flat reflections are three major unwanted effects usually eliminated by data conditioning. The obtained results from Data conditioning, Simultaneous inversion (SI), Lambda mu rho transform (LMR) and Elastic impedance inversion (EI) methods are discussed herewith.

5.2.1 Data conditioning

As mentioned before, data conditioning is a quite significant step in SI and LMR transform method. Data conditioning enhances the S/N ratio and hence increases the resolution of derived inversion results. The data conditioning was applied in the following way: First, if the data is available in the offset domain and not available in the angle domain, it needs to be converted into an angle domain (Maurya et al., 2020). The data conditioning has five major steps, namely, Bandpass filter, Muting, Super gather, Parabolic radon transforms, and Trim statics. These steps are describing in the subsequent subsection.

The bandpass filter process is the first process of data conditioning which allows applying a band-pass filter to a subset of seismic data. This filter can suppress noise and does not affect the shape of the wavelet. Figs. 5.35(a and b) show gathers before and after applying the bandpass filter process, respectively. The second step of data

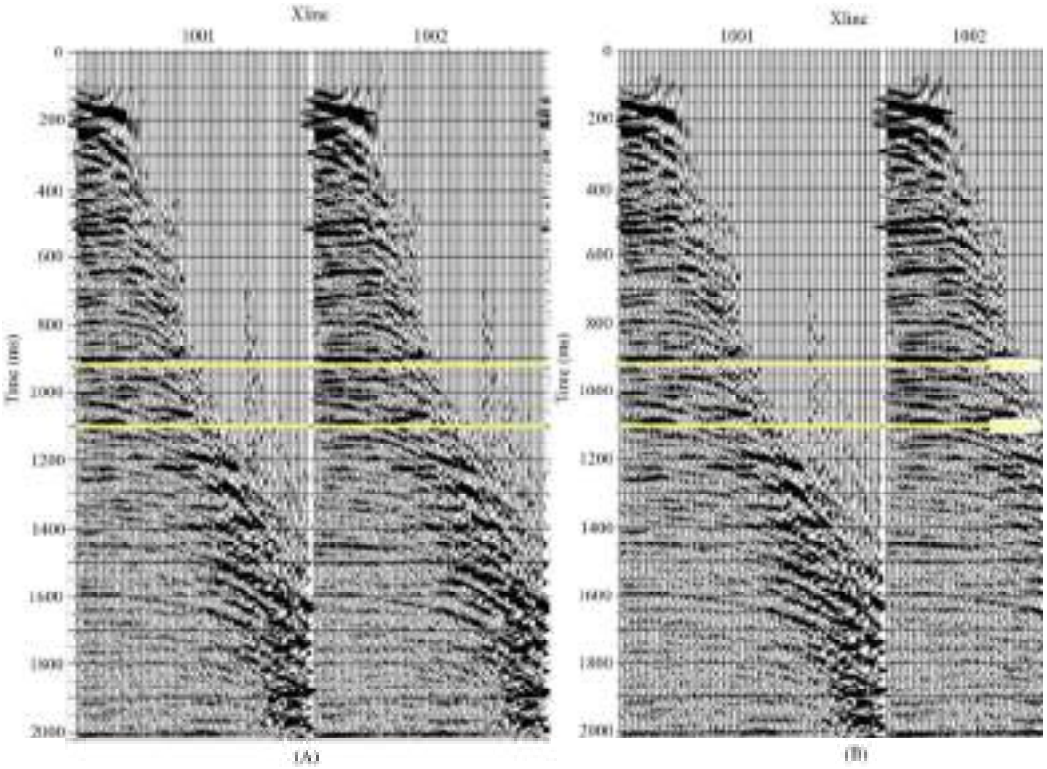

FIGURE 5.35: Cross-section of seismic data (Crossline 1001 and 1002), a) before b) after bandpass filter process

conditioning is muting. It removes faulty data from a set of gathers by setting the amplitude for this data to zero, so only the reliable data is used for the inversion. Usually, mute is applied after normal moveout (NMO) correction to eliminate the effect of NMO stretch. Figs. 5.36(a and b) show gathers before and after applying the muting process, respectively.

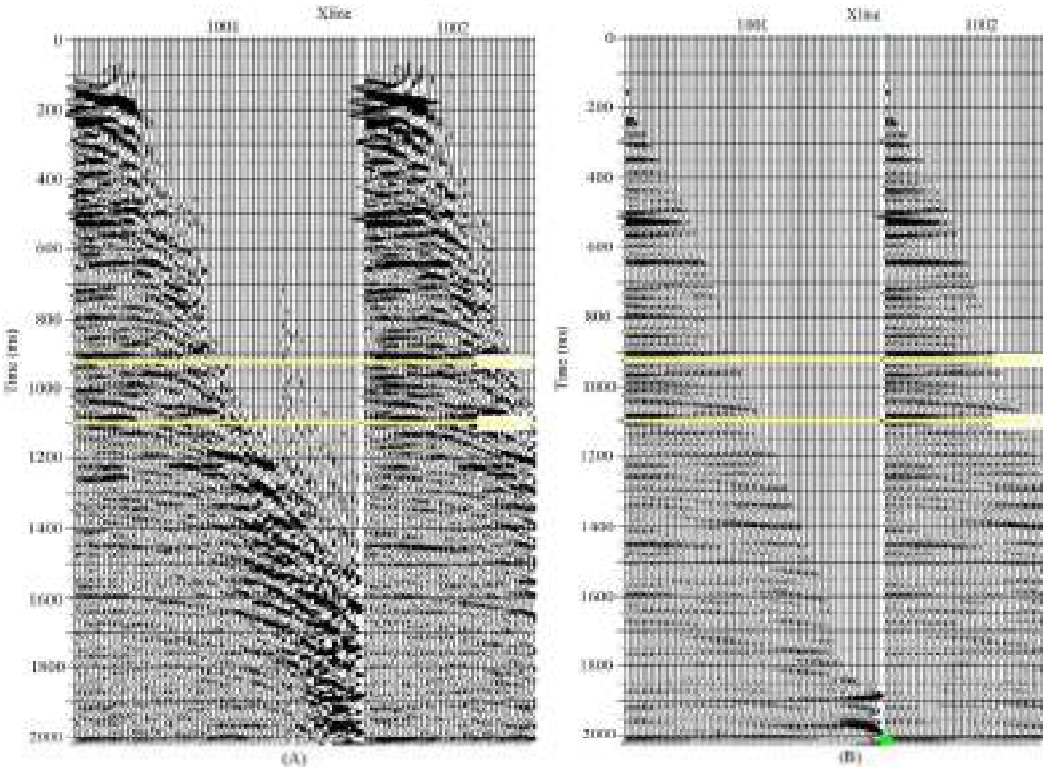

FIGURE 5.36: Cross-section of seismic data (Crossline 1001 and 1002), a) Before b) after the muting process

The third step of data conditioning is the super gather process. It creates an average CDPs to increase the S/N ratio by collecting neighboring CDPs and attaching them together (Mari et al., 1999; Singleton, 2009). Figs. 5.37(a and b) show gathers before and after applying the super gather process, respectively. The reflectors in the super gathers are more clearly visible.

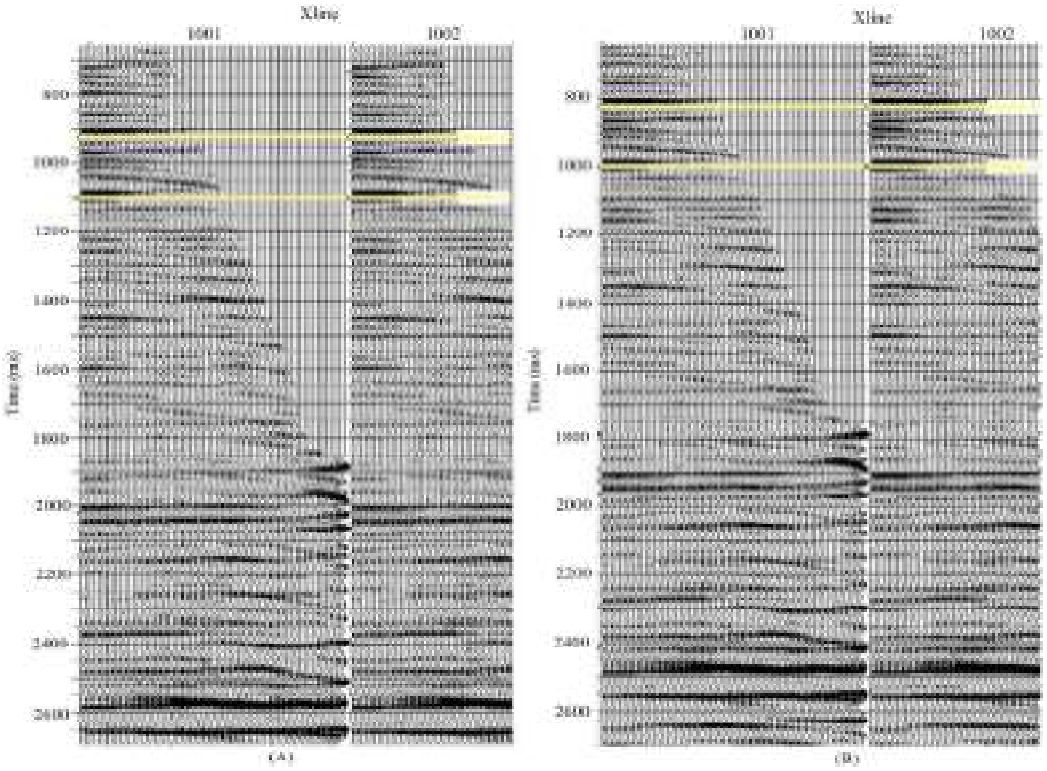

FIGURE 5.37: Cross-section of seismic data (Crossline 1001 and 1002), a) Before b) after super gather process

The fourth step of the data conditioning is the parabolic radon filter process. The process is either elimination of multiples or suppression of radon noise. When the model is generated, then Radon Transform deducts the model of these noises or multiples from the data, producing a collection of data that is significantly decreased in noise and improves the traces (Yilmaz, 1990). Figs. 5.38(a and b) show gathers before and after applying the radon transform process, respectively. The resulted gathers show a high S/N ratio.

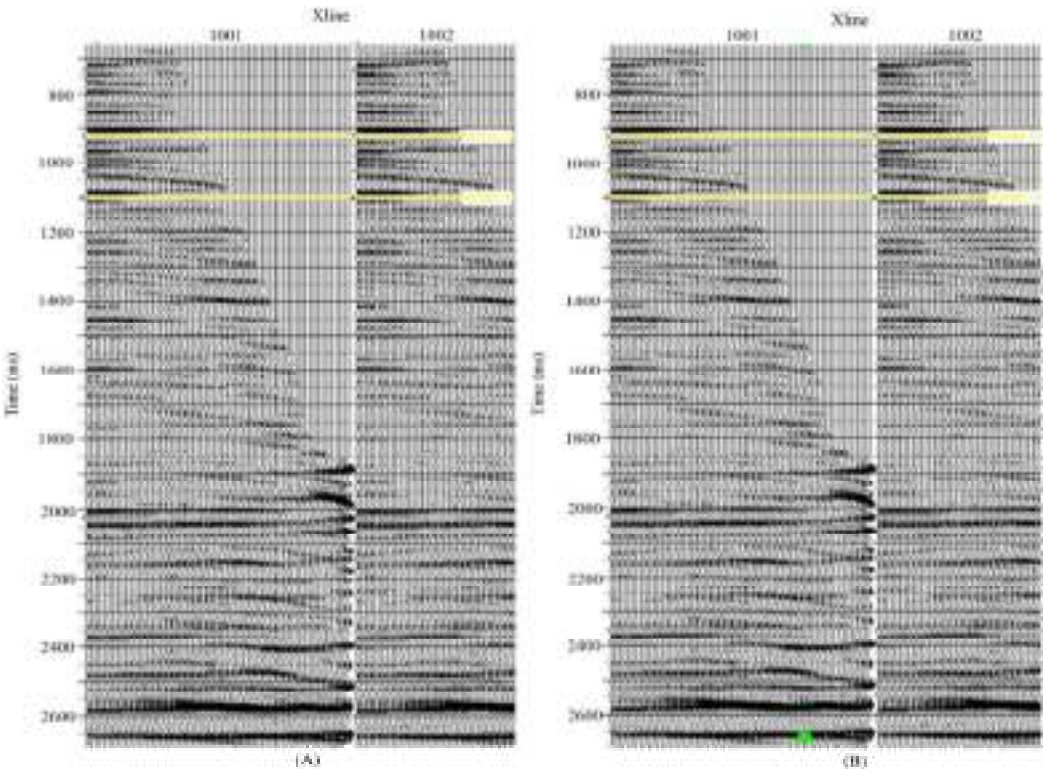

FIGURE 5.38: Cross-section of seismic data (Crossline 1001 and 1002), a) Before b) after radon transform process

The last step of data conditioning is the trim statics process. It fixes move-out difficulties of migration on pre-stack data. Its efforts to decide an appropriate shift to apply to each and every trace in a gather. Commonly, the CDP stacked trace is the reference trace. Figs. 5.39(a and b) show gathers before and after trim statics process. The resulted gathers show very flat horizons. The high ($> 60Hz$) and low frequencies ($< 10Hz$) are removed from seismic data.

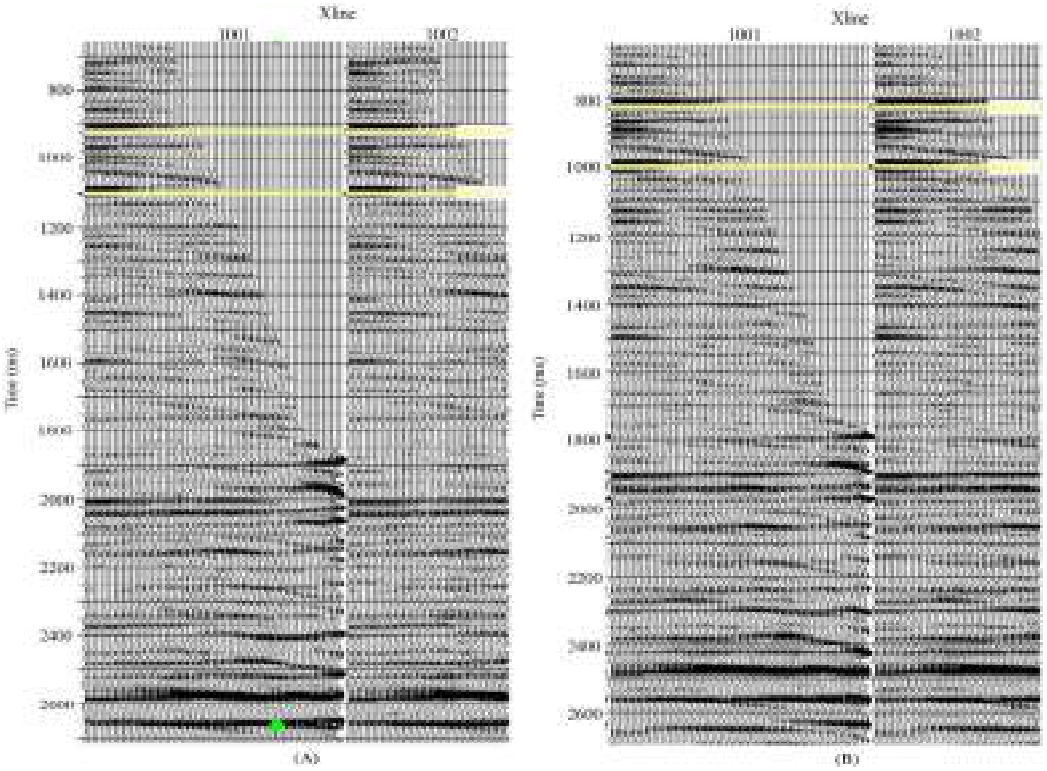

FIGURE 5.39: Cross-section of seismic data (Crossline 1001 and 1002), a) before b) after trim statics process

5.2.2 Comparative evaluation of simultaneous inversion between raw and conditioned gather

For the comparative evaluation, SI has been applied on raw gather as well as conditioned gather separately. The comparison of wavelets has been obtained from raw gather and conditioned gather is revealed in Fig. 5.40. Fig. 5.41 shows models for raw gather and conditioned gather. Fig. 5.41a shows the P-impedance model, S-impedance model and density model while P-wave, S-wave and V_P/V_S ratio models are shown in Fig. 5.41b. All the models clearly indicate the distinction between raw and conditioned data gathers.

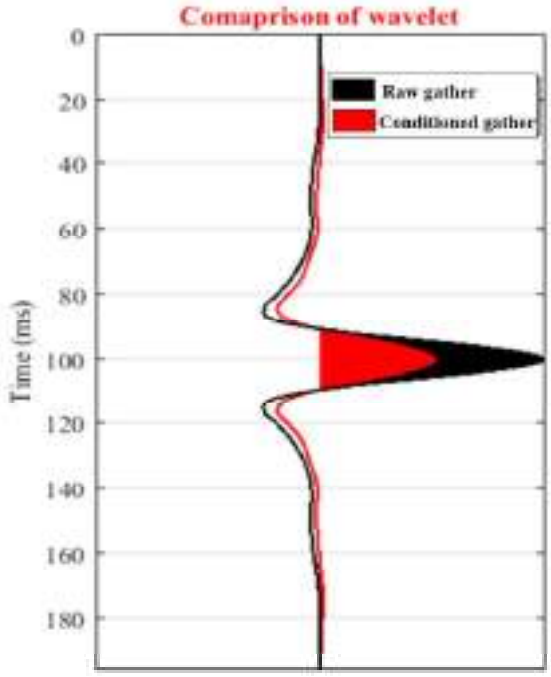

FIGURE 5.40: Comparison of wavelets obtained from SI method

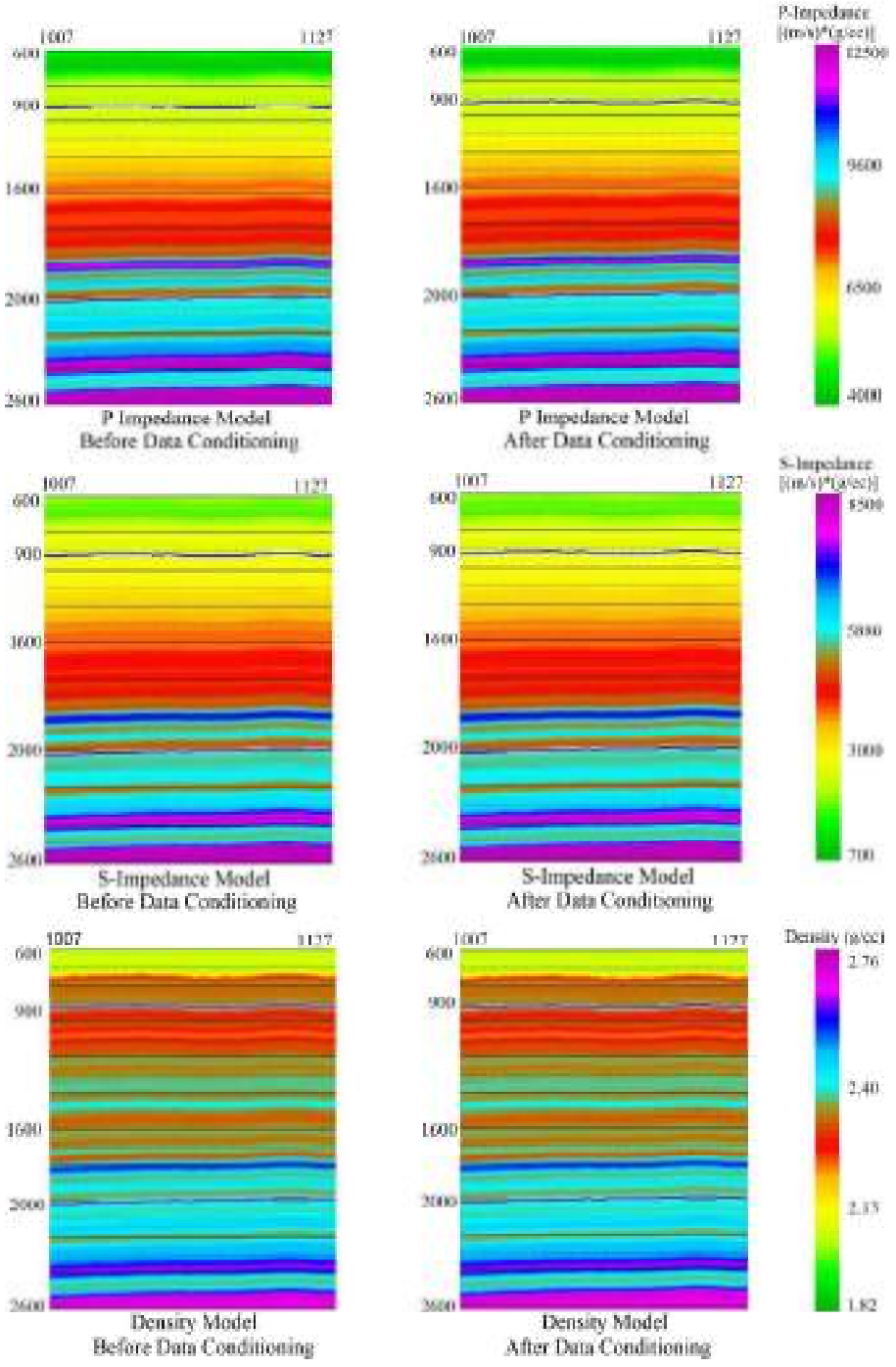
1007
1127
600
900
1600
2000
2600
P Impedance Model
Before Data Conditioning
P Impedance Model
After Data Conditioning
P-Impedance
[(m/s)*(g/cc)]
12500
9600
6500
4000
S-Impedance Model
Before Data Conditioning
S-Impedance Model
After Data Conditioning
S-Impedance
[(m/s)*(g/cc)]
8500
5000
3000
700
Density Model
Before Data Conditioning
Density Model
After Data Conditioning
Density (g/cc)
2.76
2.40
2.13
1.82

(A)

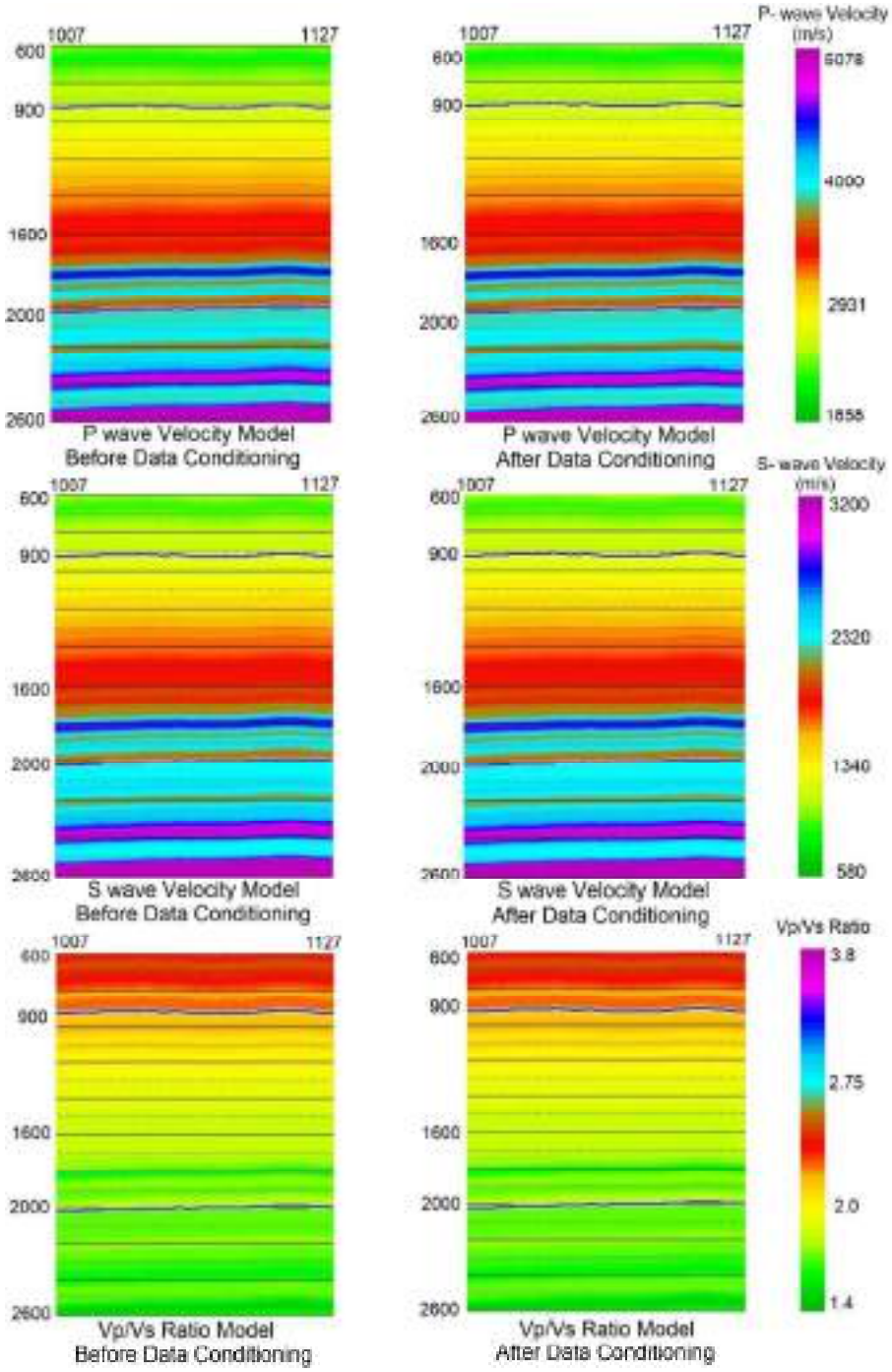

(B)

FIGURE 5.41: (a) Initial model for P-impedance, S-impedance and density and (b) Initial model for P-wave, S-wave and V_P/V_S ratio obtained from SI method

Fig. 5.42 shows the inversion outcome of the P-impedance (Z_P), S-impedance (Z_S),

density (ρ) and the V_P/V_S ratio with the corresponding parameters at well (Well: L-30). The correlation coefficient is 0.82 and 0.87 (shown in Fig. 5.42) for raw and conditioned gather, respectively. The inverted P-impedance (Track 1), S-impedance (Track 2), Density (Track 3), and V_P/V_S ratio (Track 4) from the well (green), model (black), raw gather (red) and trim gather (blue) for composite trace are revealed in Fig. 5.42. Subsequently, these values have been used for predicting the inverted petrophysical properties for the entire seismic volume. Fig. 5.43 shows parameters used for SI.

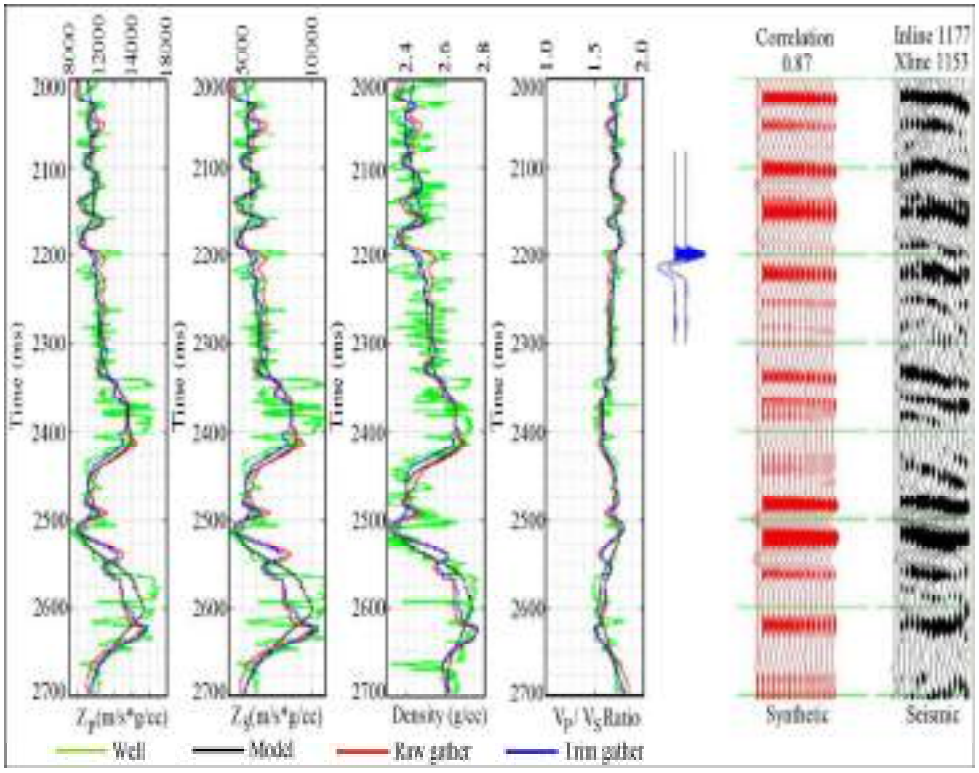

FIGURE 5.42: SI analysis for one trace

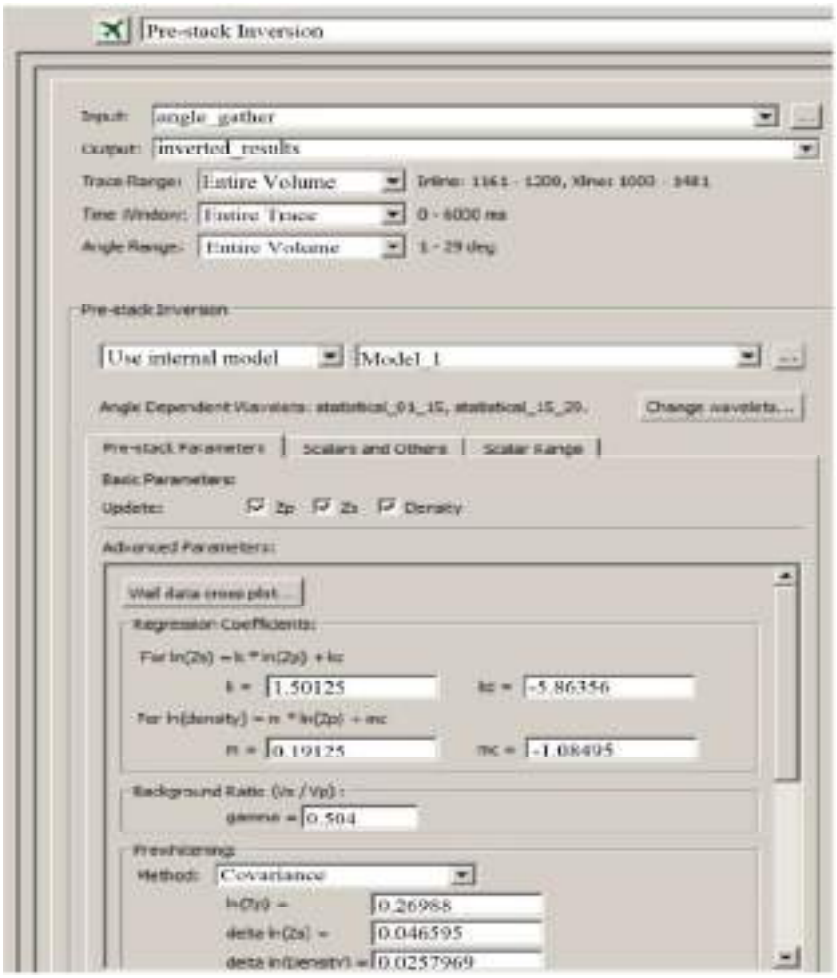

FIGURE 5.43: The parameters used in SI method

Fig. 5.44 shows a cross plot between original curves versus inverted curves for quality check of the inverted results. Fig. 5.44a shows a cross plot of original and inverted Z_P whereas Figs. 5.44b, 5.44c and 5.44d depict cross plot of original and inverted Z_S, original and inverted density (ρ) and original and inverted V_P/V_S ratio, respectively. It is observed that the scatter points for all cross plots lay adjacent to the best-fit line which indicates the adequate performance of the procedure in both the cases (conditioned and raw gather). The conditioned gather results show slightly more closeness with the best-fit line as compared to the raw gather, which is because conditioned gather shows slightly better results for the composite trace.

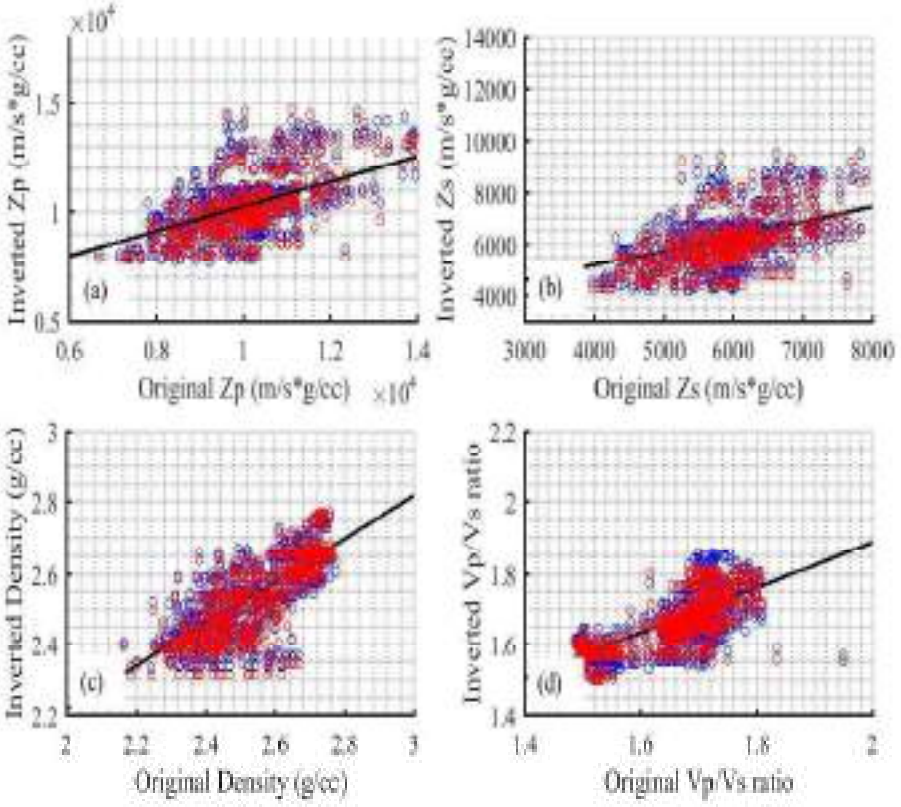

FIGURE 5.44: (a) Cross plot between Original and Inverted Z_P , (b) Cross plot between Original and Inverted Z_S, (c) Cross plot between Original Density and Inverted Density, and (d) Cross plot between Original and Inverted V_P/V_S ratio (For both raw gather and conditioned gather)

After getting acceptable results from the composite trace for both the cases, the algorithm has been applied to the entire seismic sections to estimate subsurface petrophysical parameters in the inter-well region. Figs. 5.45, 5.46, 5.47, 5.48, 5.49 and 5.50 show cross-section of inverted P-impedance, S-impedance, density, P-wave, S-wave and V_P/V_S ratio, respectively derived from pre-stack SI (both raw and conditioned gather). For simplicity, the results of only 80 traces out of 59240 traces are illustrated. The seismic amplitudes inversion produced the color-coded panel, in which low inverted value is represented by green and yellow colors, and high inverted value is represented by pink and blue colors. Figs. 5.45a, 5.46a, 5.47a, 5.48a, 5.49a and 5.50a represent cross-section of inverted acoustic impedance, S-impedance, density, P-wave, S-wave

and V_P/V_S ratio, respectively derived from raw gather while the cross-section of inverted acoustic impedance, S-impedance, density, P-wave, S-wave and V_P/V_S ratio derived from conditioned gather is shown in Figs. 5.45b, 5.46b, 5.47b, 5.48b, 5.49b, and 5.50b, respectively. Figures further show the continuous variation of density in the subsurface and the absence of any anomalous zone in the form of any major reservoir. The inverted P- and S-impedance study has been varied from 2000(m/s*g/cc) to 18000(m/s*g/cc) as shown in Figs. 5.45 and 5.46. The density study ranged from 1.8 to 2.8 g/cc as shown in Fig. 5.47. The V_P and V_S study ranged from 1500(m/s) to 6500(m/s) and 500(m/s) to 4000 (m/s) respectively as shown in Figs. 5.48 and 5.49. The V_P/V_S ratio study ranged from 1.5 to 2.8 as shown in Fig. 5.50. There are no major low impedances, density and velocity zones in inverted volume.

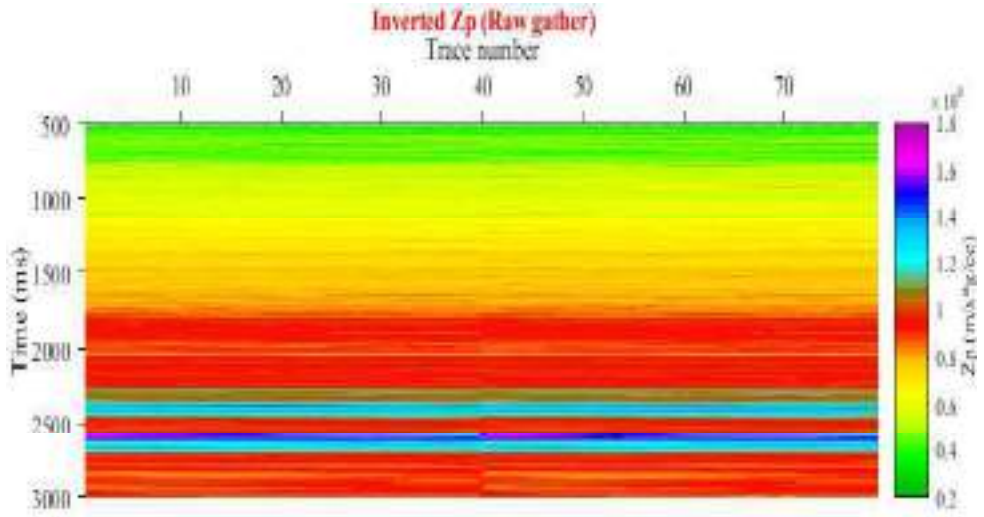

(A)

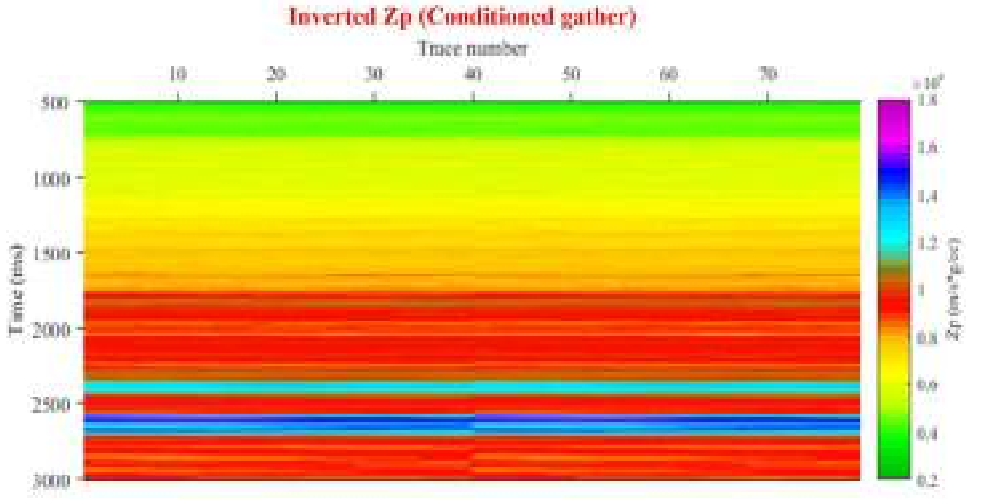

(B)

FIGURE 5.45: (a) Inverted P-impedance from raw data, (b) Inverted P-impedance from conditioned data.

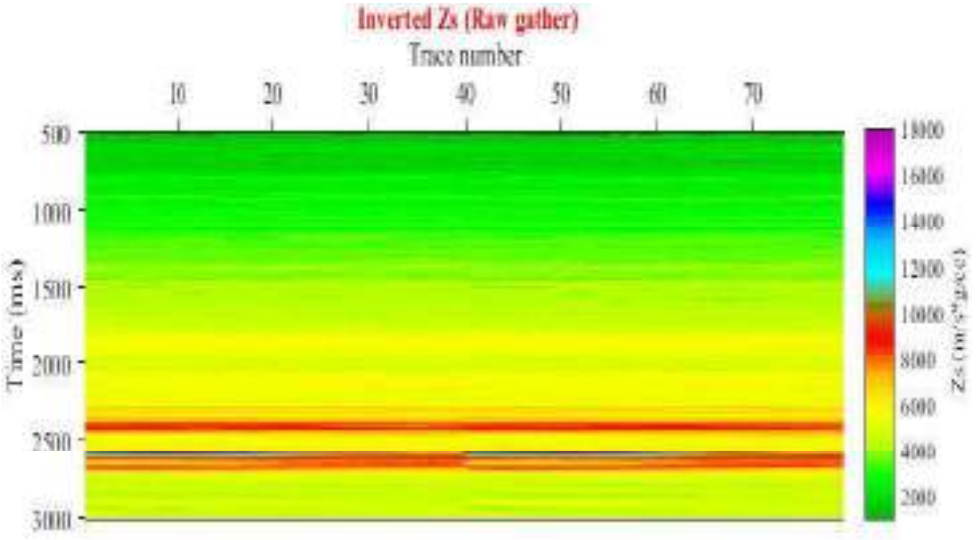

(A)

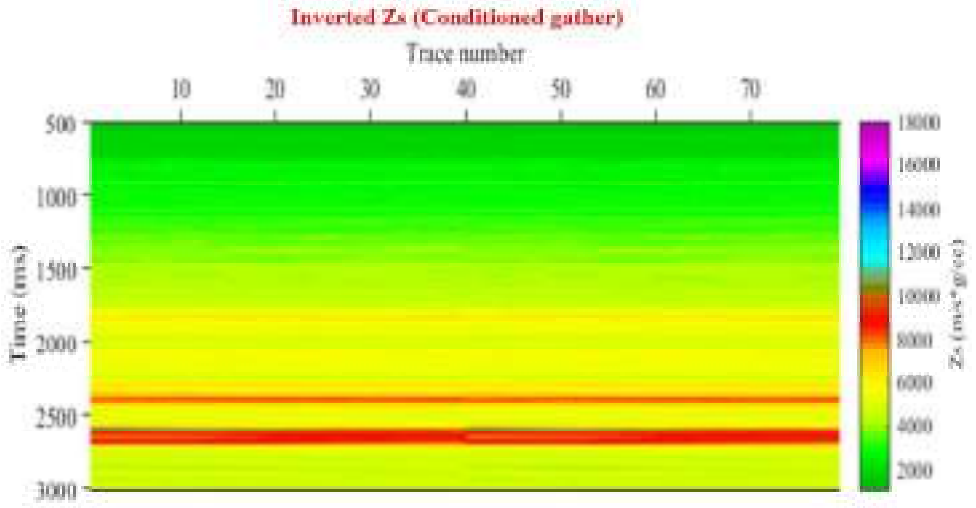

(B)

FIGURE 5.46: (a) Inverted S-impedance from raw data, (b) Inverted S-impedance from conditioned data

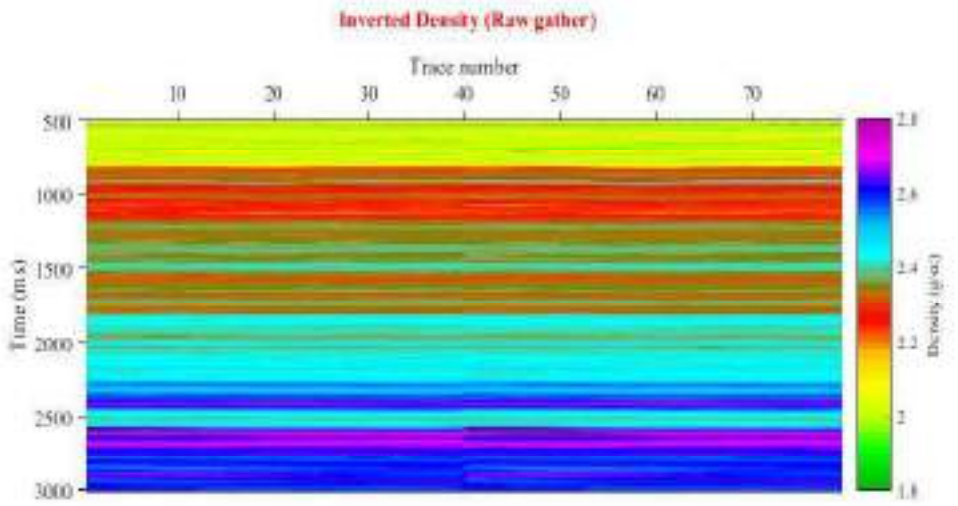

(A)

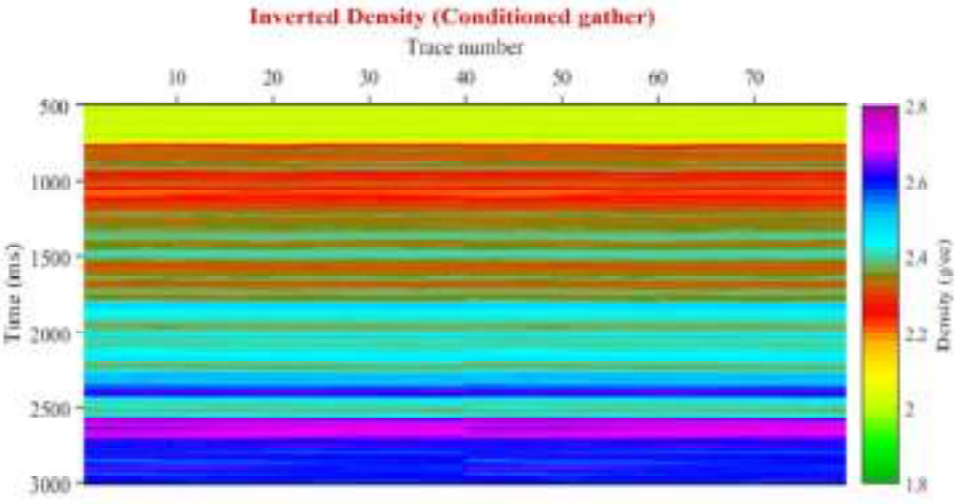

(B)

FIGURE 5.47: (a) Inverted density from raw data, (b) Inverted density from conditioned data

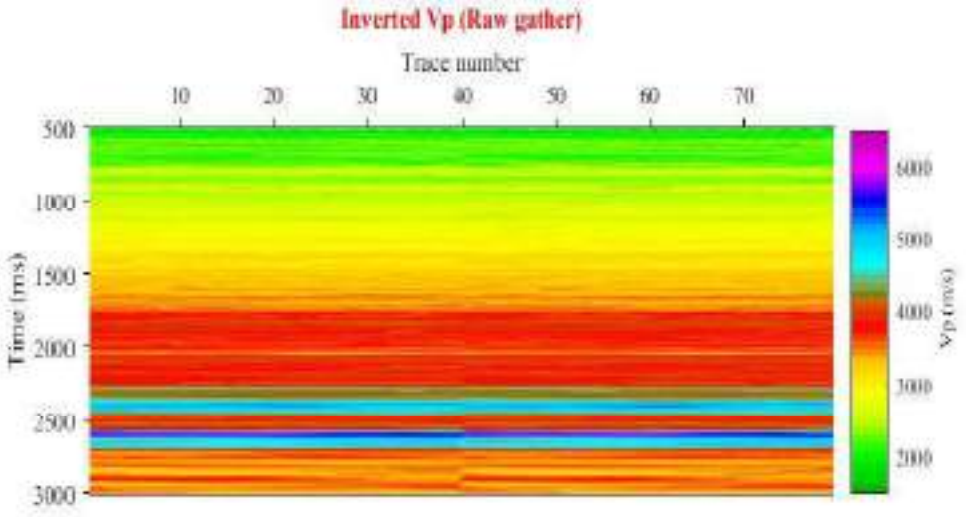

(A)

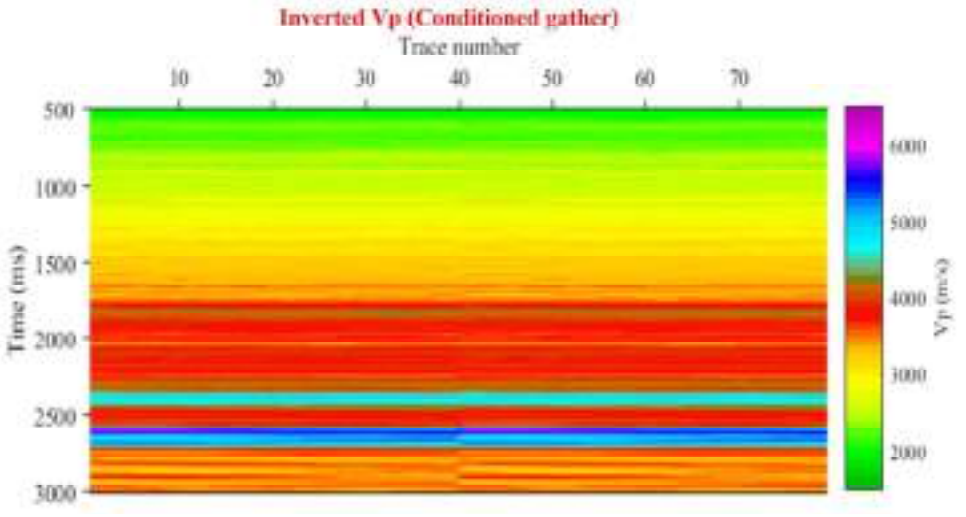

(B)

FIGURE 5.48: (a) Inverted P-wave from raw data, (b) Inverted P-wave from conditioned data

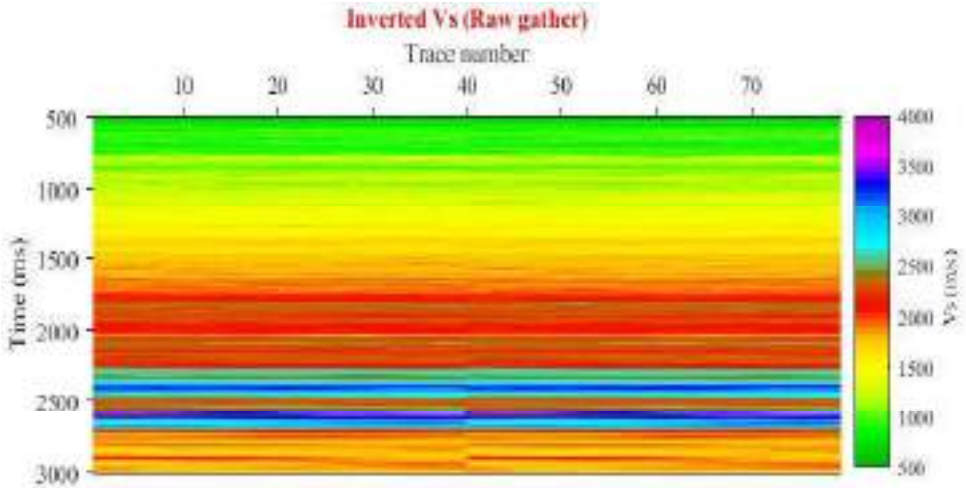

(A)

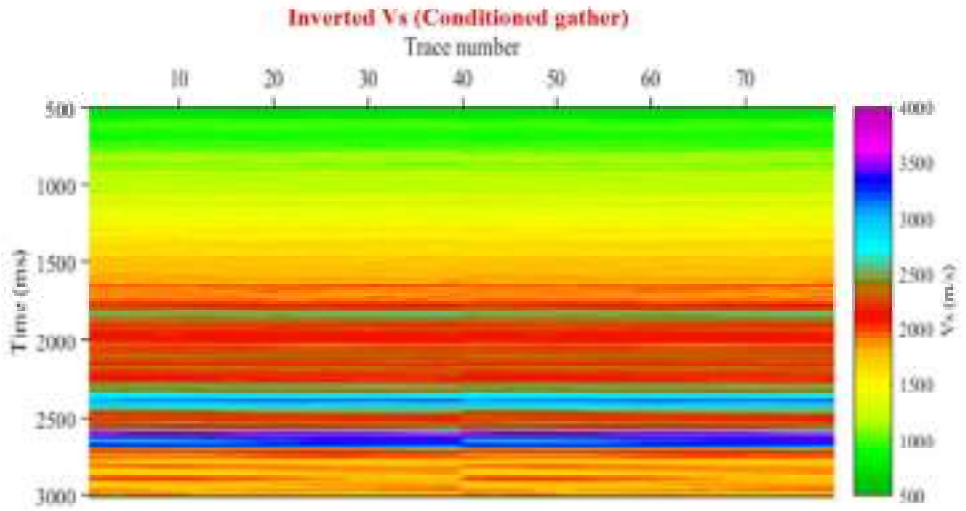

(B)

FIGURE 5.49: (a) Inverted S-wave from raw data, (b) Inverted S-wave from conditioned data

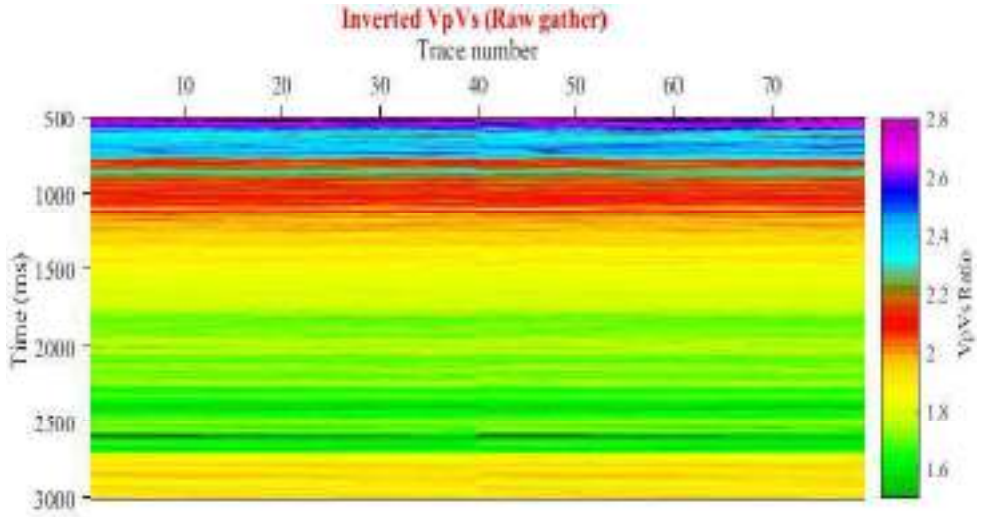

(A)

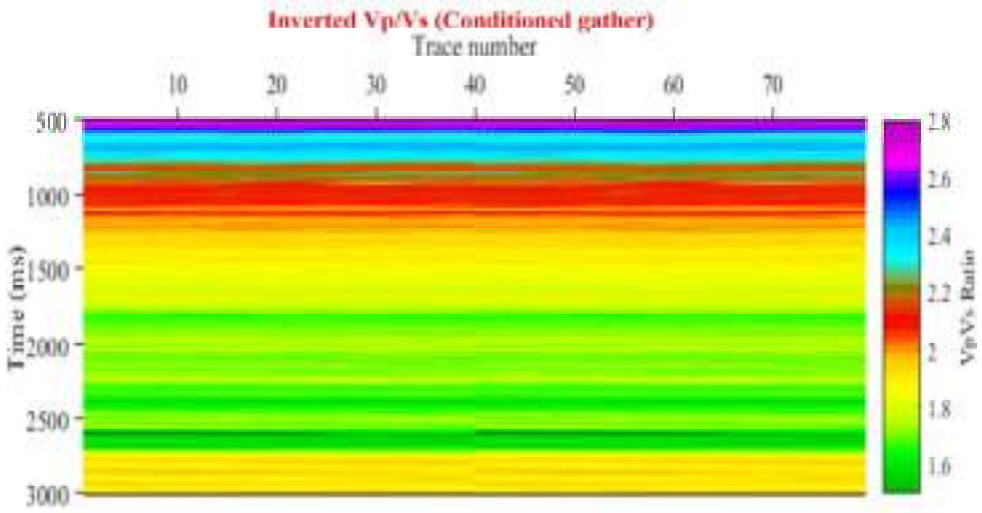

(B)

FIGURE 5.50: (a) Inverted V_P/V_S ratio from raw data, (b) Inverted V_P/V_S ratio from conditioned data

The cross plot of S-impedance vs P-impedance and density vs P-impedance on a log-log scale is one of the key indicators of the presence of an anomalous zone. Inverted results of conditioned gather are better than the inverted results of raw gather derived from SI method. The findings from the analysis indicate the absence of an anomalous zone.

5.2.3 Comparative evaluation of lambda-mu-rho transform between raw and conditioned gather

In this study, efforts have been made to explain the impact of data conditioning using LMR transform. Fig. 5.51 shows the variation of lambda-rho whereas Fig. 5.52 shows mu-rho variation. Fig. 5.51a shows inverted lambda rho derived from raw gather while Fig. 5.51b shows inverted lambda rho derived from conditioned gather. Fig. 5.52a shows inverted mu rho derived from raw gather and Fig. 5.52b shows inverted mu rho derived from conditioned gather. Both lambda-rho and mu-rho study range vary from 0-60(GPa*g/cc).

LMR parameters are very significant in the detection of gas reservoirs because LMR parameters are more sensitive compared to the impedance values. Hence, mu-rho versus lambda-rho has been cross plotted as shown in Figs. 5.53(a and b). From the figures, it is observed that there are no data points in the near vicinity of the lambda-rho and mu-rho axis. This indicates the absence of a reservoir in the study area. A similar indication was given by SI method also.

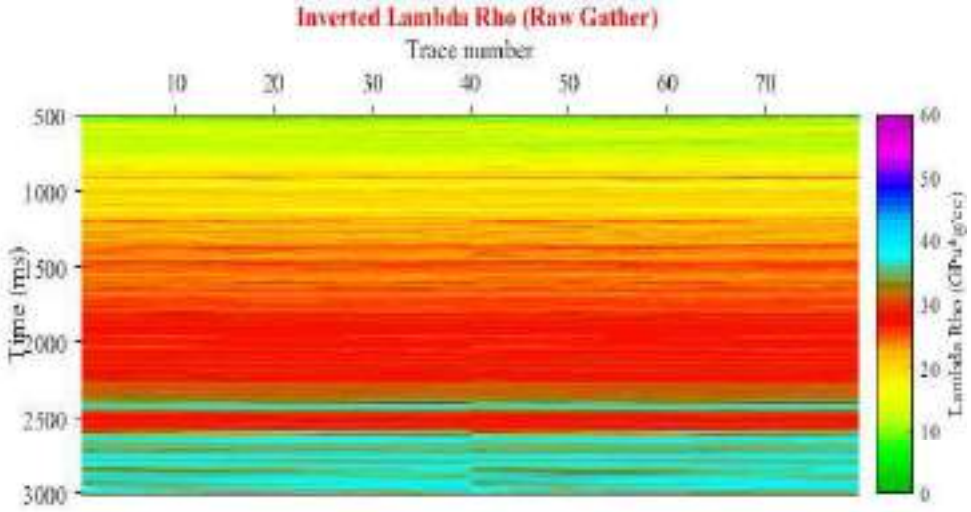

(A)

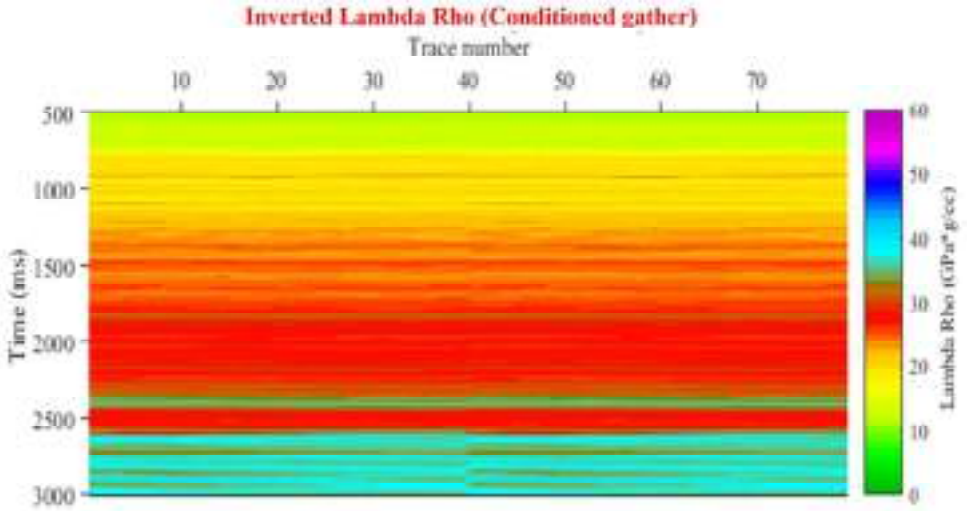

(B)

FIGURE 5.51: (a) Inverted lambda rho from raw data, (b) Inverted lambda rho from conditioned data

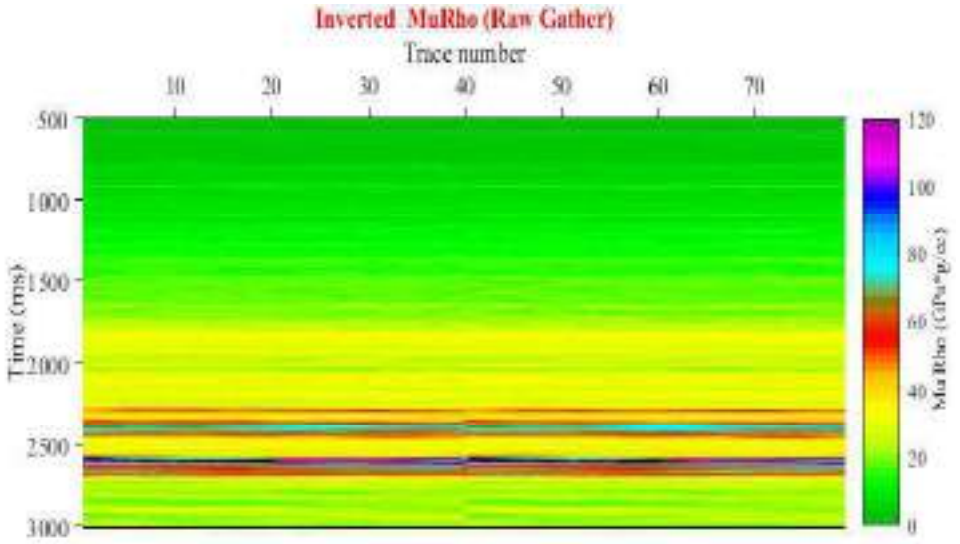

(A)

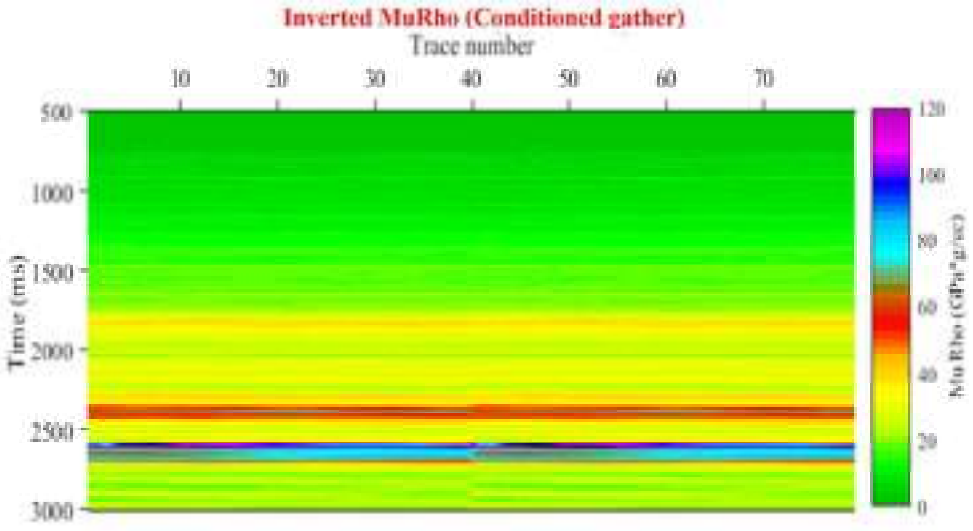

(B)

FIGURE 5.52: (a) Inverted mu rho from raw data, (b) Inverted mu rho from conditioned data

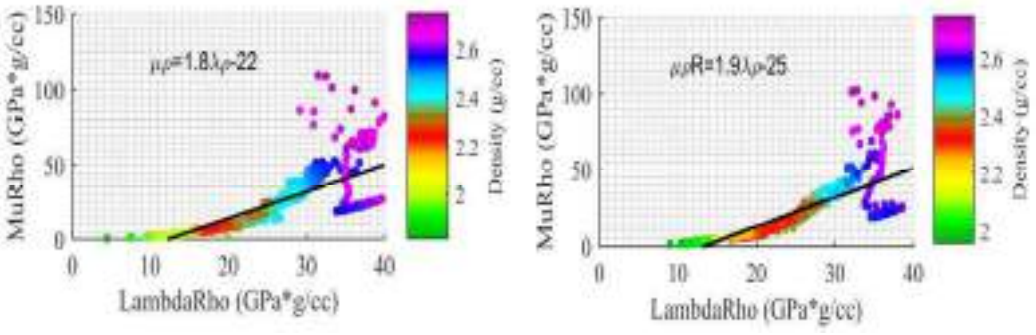

(A) (B)

FIGURE 5.53: (a) Inverted mu rho from raw data, (b) Inverted mu rho from conditioned data

5.2.4 Elastic impedance method

(i) Synthetic data example results

The effect of Gaussian noise on EI has been investigated and revealed in Figs. 5.54. Figs. 5.54a, 5.54c, 5.54e, and 5.54g display synthetic seismogram while Figs. 5.54b, 5.54d, 5.54f, and 5.54h display EI results for zero noise level, 10% noise level, 20% noise level and 30% noise level in the data, respectively. The correlation values are 0.998, 0.992, 0.984 and 0.963 and corresponding RMS error values are 0.019, 0.092, 0.190 and 0.265 for zero noise level, 10% noise level, 20% noise level and 30% noise level in the data, respectively. From the results of correlation values and error values, it may be understood that the values of elastic impedance are not much impacted by Gaussian noise levels in the data. The efficacy of EI method has been estimated to be decreasing only 3.5% with the addition of noise level up to 30%. Figs. 5.55(a and b) clearly reveal that as the RMS error increases with Gaussian noise level in the data. It is also noticeable that the error sharply increases by up to 30% noise level. There was no perceptible change beyond the 30% noise level.

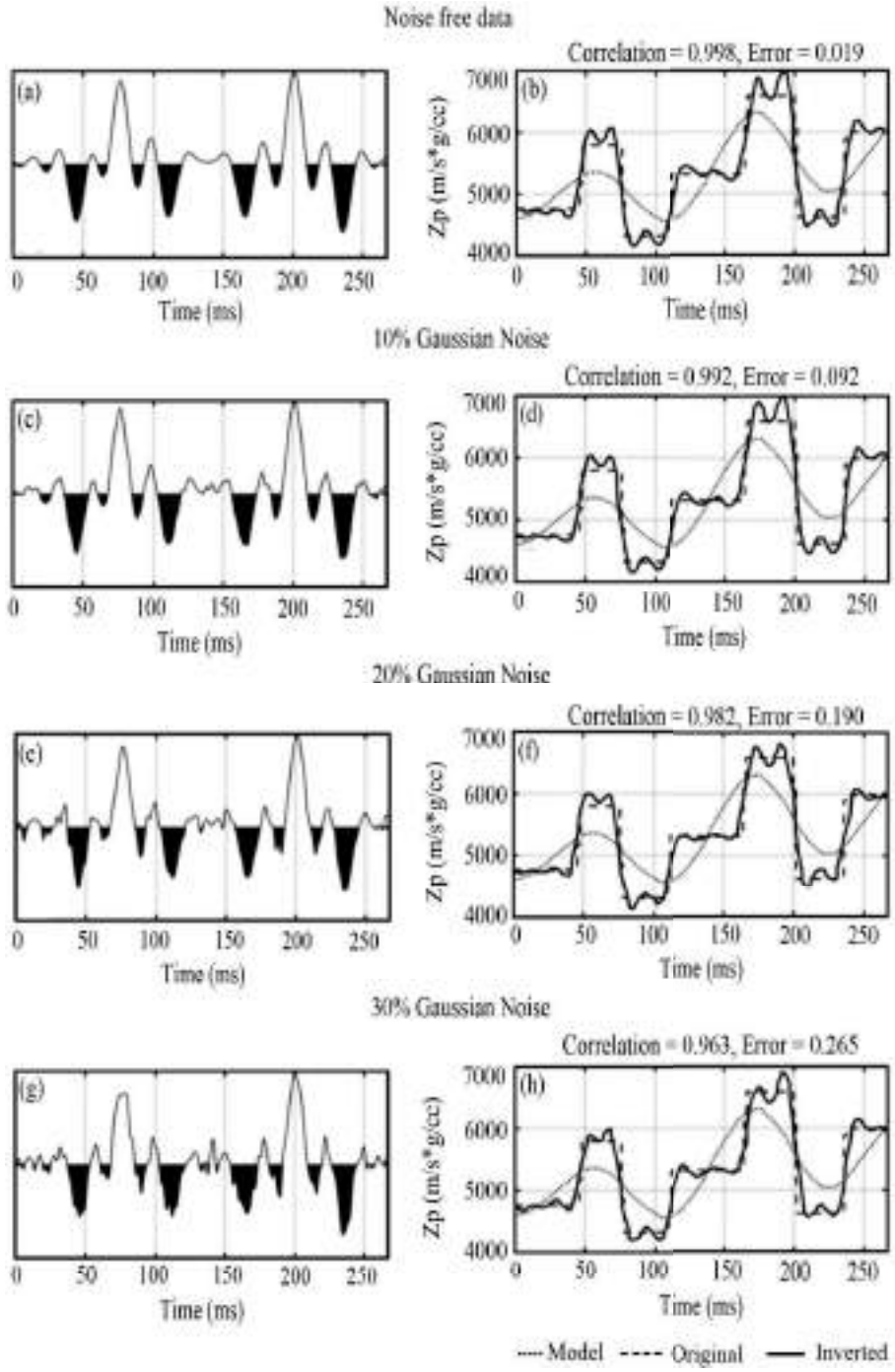

FIGURE 5.54: EI results for the synthetic case. (Left) Seismograms and (right) the corresponding inversion results (after addition of Gaussian noise)

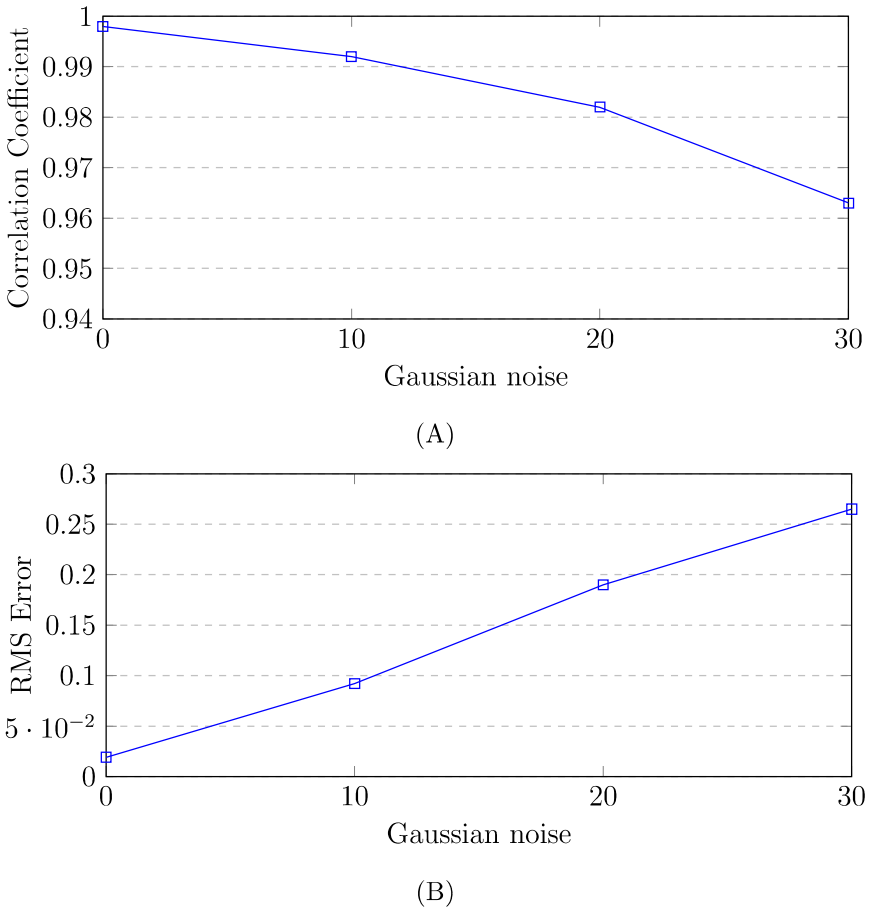

FIGURE 5.55: Variation of (a) correlation coefficient and (b) RMS error with Gaussian Noise

(ii) Results of EI on real-time data

Real-time pre-stack data from Penobscot has been used to estimate subsurface elastic properties using EI method. Figs. 5.56 shows near angle stack (left) and far angle stack (right) sections which have been used as input for elastic impedance estimation. Fig. 5.56 illustrates that the S/N ratio increases due to stacking. It is also noticeable that the resolution of the far angle stack section is higher in comparison to the near angle stack (as highlighted by the arrows in Figs. 5.56). The 0^0 to 15^0 incidence angle represented near angle stack while 15^0 to 30^0 represented far angle stack as per standards norm.

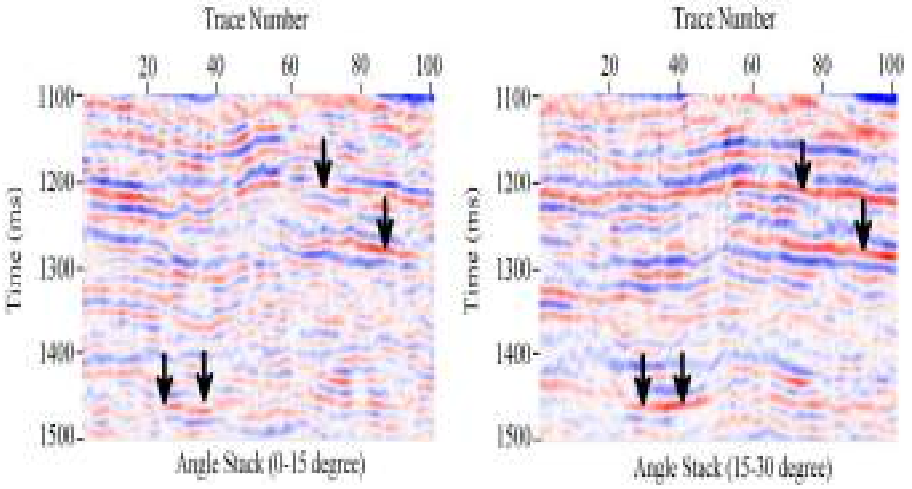

FIGURE 5.56: (Left) near-angle stack and (Right) far-angle stack sections and; the major difference between them is highlighted

The inverted elastic impedance for near angle stack, inverted elastic impedance for far angle stack and well log elastic impedance is illustrated in Fig. 5.57. It is revealed from Fig. 5.57 that the seismic and well log elastic impedance values are closely matching. This suggests the satisfactory performance of the algorithm for the determination of elastic impedance values. For the quality check, crossplot has been produced between original and inverted elastic impedance for near (left) and far angle stack (right) as shown in Figs. 5.58. The maximum number of scatter points are in very near proximity to the best fit line. This suggests good execution of the algorithm.

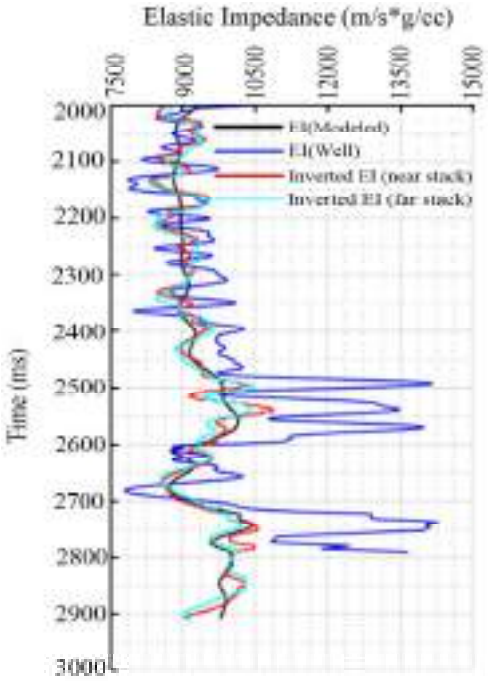

FIGURE 5.57: Comparison between Inverted and original elastic impedances for the composite trace case

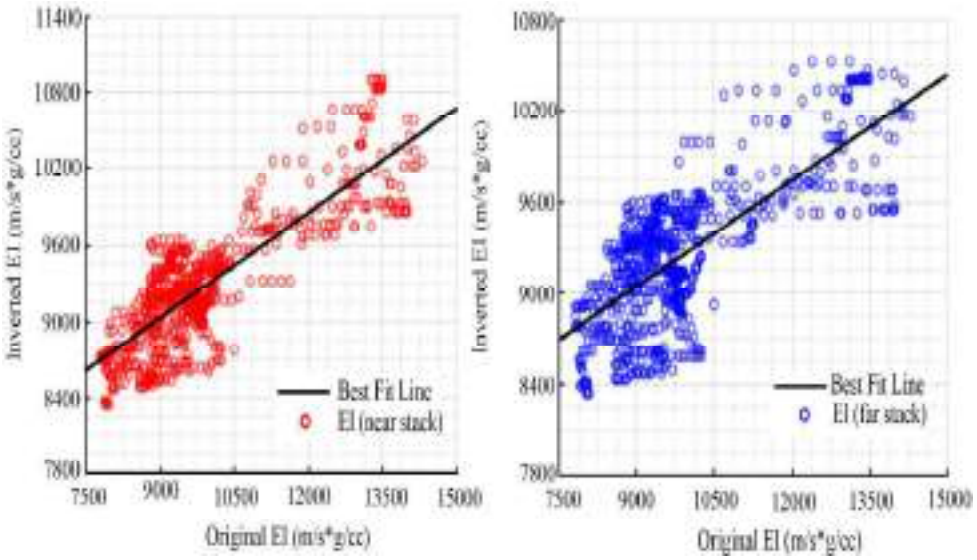

FIGURE 5.58: Crossplot between original and inverted elastic impedances for near angle stack (left) and far angle stack (right)

A comparison of inverted elastic impedance from near and far angle stack with acoustic impedance (AI) is produced and plotted in Fig. 5.59. It is observed that the

inverted elastic impedance follows the trend of AI very closely. Both inverted elastic impedance and AI variation range are different. It is observed that both inverted elastic impedances (near and far angle stack) vary in a similar way. Fig. 5.60 shows a crossplot between near angle stack and far angle stack inverted elastic impedances has been generated with a color bar of acoustic impedance. In the presence of a gas zone, some cluster points away from the best fit line should appear which is not seen from Fig. 5.60; hence the possibility of gas-bearing formation is less in this area. Still, there may chance of the presence of gas formation, but this would be minor hence cannot be detected by EI method.

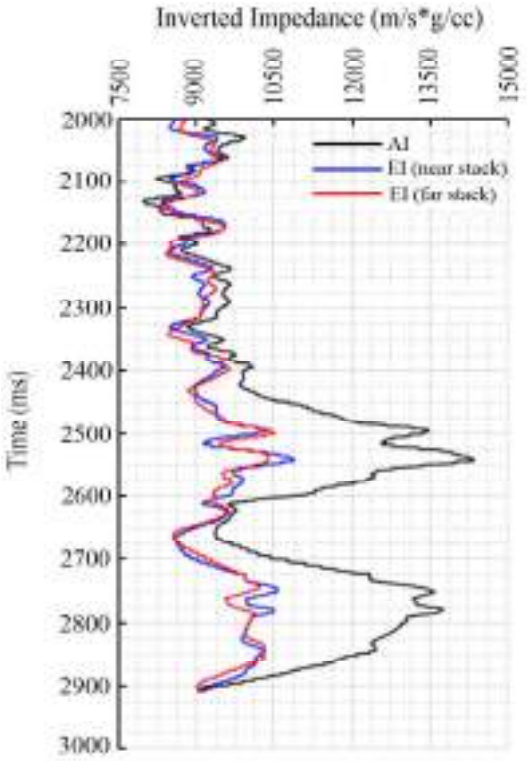

FIGURE 5.59: Comparison of elastic impedance with acoustic impedance for composite trace near a well location

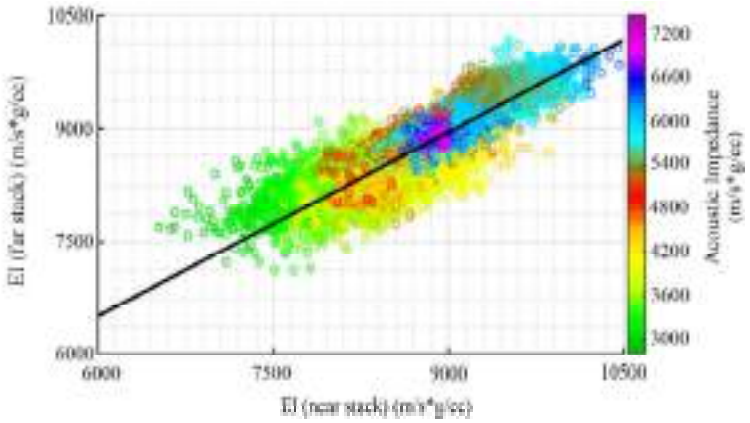

FIGURE 5.60: Cross-plot between inverted elastic impedance from near stack seismic section and far stack seismic section

Subsequently, the whole seismic section was inverted for elastic impedance and a representative cross-section is represented in Figs. 5.61. The left side of the figure depicts near angle stacks elastic impedance cross-section while far angle stack elastic impedance cross-sections are shown on the right side of the figure. The difference between the near and far angle stack elastic impedance section has been clearly noticed and highlighted by the arrow. The improved reflector resolution is higher in the far stack elastic impedance section in comparison to the near stack elastic impedance section.

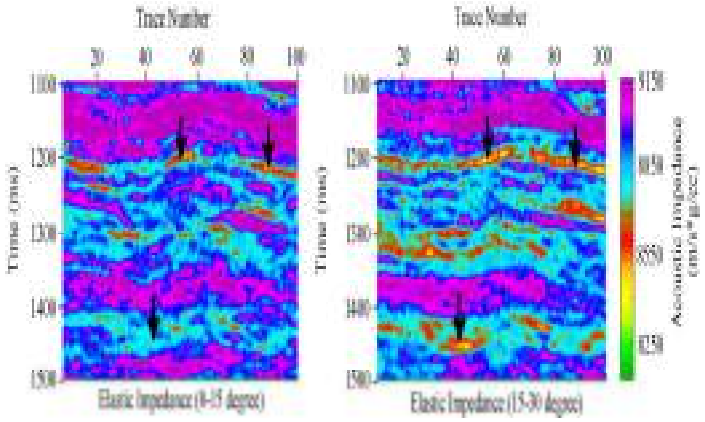

FIGURE 5.61: Cross-section of inverted elastic impedance generated for near angle stack gather (left) and far angle stack gather (right)

These analyses are performed for seismic data containing inline 1200 to 1400 and cross lines 1161 to 1200 and hence it cannot deny that the other part of the region also does not contain any gas formation or overpressure zone.

5.3 Results of geostatistical techniques

In this section, the four geostatistical analysis techniques, namely, single attribute analysis, multi-attribute analysis, probabilistic neural network (PNN) and multilinear feed forward network (MLFN) were performed in the F3 block post-stack seismic with MBI derived impedance to obtain porosity, P-wave, density and gamma ray volumes. The results are as follows:

5.3.1 Single attribute analysis technique

In the single attribute analysis process, seismic attributes are extracted for each seismic trace near well locations for the prediction of petrophysical parameters. This is very helpful to test which attribute will best predict a desired petrophysical property. The Single Attribute List evaluates external and internal attributes to choose which attributes are most suitable for predicting the petrophysical properties (Russell et al., 1997). The single attribute means that the attributes are used individually. Seismically derived attributes are used as internal attributes while MBI derived inverted impedance is used as an external attribute. The Single Attribute correlation list has been shown in Tables 5.1, 5.2, 5.3 and 5.4 for porosity, density, P-wave and gamma ray, respectively. Each table line holds information for a specific attribute. The attributes are arranged by rising prediction error, i.e., by decreasing suitability for predicting the target. The Sqrt(inverted impedance), 1/(inverted impedance), (inverted impedance)^2 and dominant frequency attributes have been used for the prediction of porosity, density, P-wave and gamma ray, respectively (as shown in Fig. 5.62). The correlation has been found very low. Therefore, single attribute analysis derived results were not used for further generation of petrophysical properties volumes.

TABLE 5.1: The single attribute analysis technique correlation results for porosity

S.No.	Target	Attribute	Error	Correlation
1	Sqrt(Porosity)	Sqrt(inverted P-impedance)	0.031456	-0.838899
2	Porosity	Log(inverted P-impedance)	0.031503	-0.853565
3	Sqrt(Porosity)	Log(inverted P-impedance)	0.031589	-0.839156
4	$(\text{Porosity})^2$	1/(inverted P-impedance)	0.031794	0.824124
5	Sqrt(Porosity)	inverted P-impedance	0.032154	-0.830579
6	Porosity	1/(inverted P-impedance)	0.032230	0.846110
7	Porosity	Sqrt(inverted P-impedance)	0.032288	-0.845513
8	Porosity	inverted P-impedance	0.033771	-0.829518
9	Sqrt(Porosity)	1/(inverted P-impedance)	0.033841	0.817183
10	Sqrt(Porosity)	$(\text{inverted P-impedance})^2$	0.035516	-0.793449
11	Porosity	$(\text{inverted P-impedance})^2$	0.037929	-0.778813
12	$(\text{Porosity})^2$	Log(inverted P-impedance)	0.041948	-0.805488
13	$(\text{Porosity})^2$	Sqrt(inverted P-impedance)	0.046069	-0.784616
14	1/(Porosity)	$(\text{inverted P-impedance})^2$	0.047386	0.058852
15	$(\text{Porosity})^2$	inverted P-impedance	0.048964	-0.756792
16	1/(Porosity)	inverted P-impedance	0.049123	0.061896
17	$(\text{Porosity})^2$	$(\text{inverted P-impedance})^2$	0.052015	-0.687359
18	Porosity	Integrated Absolute Amplitude	0.055950	-0.379310
19	Porosity	Time	0.056098	-0.373288
20	Sqrt(Porosity)	Time	0.056352	-0.379014

TABLE 5.2: The single attribute analysis technique correlation results for density

S.No.	Target	Attribute	Error	Correlation
1	(Density)^2	1 / (inverted P-impedance)	0.082672	-0.880551
2	Density	1 / (inverted P-impedance)	0.086395	-0.865310
3	Sqrt(Density)	1 / (inverted P-impedance)	0.089193	-0.854133
4	Log(Density)	1 / (inverted P-impedance)	0.093133	-0.840935
5	(Density)^2	Log(inverted P-impedance)	0.098699	0.834652
6	Density	Log(inverted P-impedance)	0.103276	0.800619
7	Sqrt(Density)	Log(inverted P-impedance)	0.106693	0.780663
8	1 / (Density)	1 / (inverted P-impedance)	0.107694	0.809897
9	(Density)^2	Sqrt(inverted P-impedance)	0.109268	0.795323
10	Log(Density)	Log(inverted P-impedance)	0.111580	0.759236
11	Density	Sqrt(inverted P-impedance)	0.113379	0.753204
12	Sqrt(Density)	Sqrt(inverted P-impedance)	0.116546	0.729597
13	(Density)^2	inverted P-impedance	0.119731	0.748188
14	Log(Density)	Sqrt(inverted P-impedance)	0.121154	0.704833
15	Density	inverted P-impedance	0.123172	0.699529
16	Sqrt(Density)	inverted P-impedance	0.125878	0.673065
17	Log(Density)	inverted P-impedance	0.129851	0.645757
18	1 / (Density)	Log(inverted P-impedance)	0.130722	-0.713680
19	(Density)^2	(inverted P-impedance)^2	0.137089	0.645968
20	Density	(inverted P-impedance)^2	0.139234	0.589468

TABLE 5.3: The single attribute analysis technique correlation results for P-wave

S.No.	Target	Attribute	Error	Correlation
1	(P-wave)^2	(inverted P-impedance)^2	172.760925	0.889590
2	Sqrt(P-wave)	inverted P-impedance	174.568436	0.900864
3	Log(P-wave)	inverted P-impedance	177.231689	0.901834
4	P-wave	inverted P-impedance	177.906540	0.895051
5	Log(P-wave)	Sqrt(inverted P-impedance)	178.565063	0.893699
6	P-wave	(inverted P-impedance)^2	179.121277	0.893528
7	Sqrt(P-wave)	Sqrt(inverted P-impedance)	183.410904	0.886374
8	1 / (P-wave)	Sqrt(inverted P-impedance)	184.905060	-0.893108
9	1 / (P-wave)	Log(inverted P-impedance)	185.604218	-0.883237
10	Sqrt(P-wave)	(inverted P-impedance)^2	190.439789	0.888554
11	P-wave	Sqrt(inverted P-impedance)	193.401093	0.874623
12	Log(P-wave)	Log(inverted P-impedance)	195.692612	0.870294
13	Sqrt(P-wave)	Log(inverted P-impedance)	203.687973	0.856668
14	Log(P-wave)	(inverted P-impedance)^2	210.555450	0.878300
15	(P-wave)^2	inverted P-impedance	214.138504	0.871939
16	P-wave	Log(inverted P-impedance)	216.974899	0.839153
17	1 / (P-wave)	inverted P-impedance	226.021912	-0.888001
18	1 / (P-wave)	1 / (inverted P-impedance)	246.583374	0.822276
19	Log(P-wave)	1 / (inverted P-impedance)	253.143204	-0.784993
20	(P-wave)^2	Sqrt(inverted P-impedance)	257.753265	0.841397

TABLE 5.4: The single attribute analysis technique correlation results for gamma ray

S.No.	Target	Attribute	Error	Correlation
1	Gamma Ray	Dominant Frequency	20.270559	0.338684
2	Gamma Ray	Average Frequency	20.439682	0.316027
3	Sqrt(Gamma Ray)	Dominant Frequency	20.490335	0.361206
4	Sqrt(Gamma Ray)	Average Frequency	20.660812	0.353073
5	Gamma Ray	Time	20.735250	0.271389
6	(Gamma Ray)^2	Dominant Frequency	20.819670	0.271065
7	(Gamma Ray)^2	Average Frequency	21.025812	0.237710
8	Sqrt(Gamma Ray)	Time	21.063311	0.227792
9	(Gamma Ray)^2	Time	21.067747	0.249658
10	Gamma Ray	(inverted P-impedance)^2	21.094177	-0.203235
11	Gamma Ray	Amplitude Weighted Frequency	21.108538	0.199997
12	Gamma Ray	Instantaneous Frequency	21.228804	0.170377
13	Sqrt(Gamma Ray)	Amplitude Weighted Frequency	21.360216	0.188550
14	Log(Gamma Ray)	Dominant Frequency	21.376907	0.351893
15	Gamma Ray	inverted˙Zp	21.387899	-0.120084
16	Gamma Ray	1 / (inverted P-impedance)	21.465540	-0.085157
17	Sqrt(Gamma Ray)	Instantaneous Frequency	21.467482	0.192200
18	Gamma Ray	Amplitude Envelope	21.472549	0.081260
19	Gamma Ray	Sqrt(inverted P-impedance)	21.492933	-0.068675
20	Gamma Ray	Filter 5/10-15/20	21.523998	-0.042862

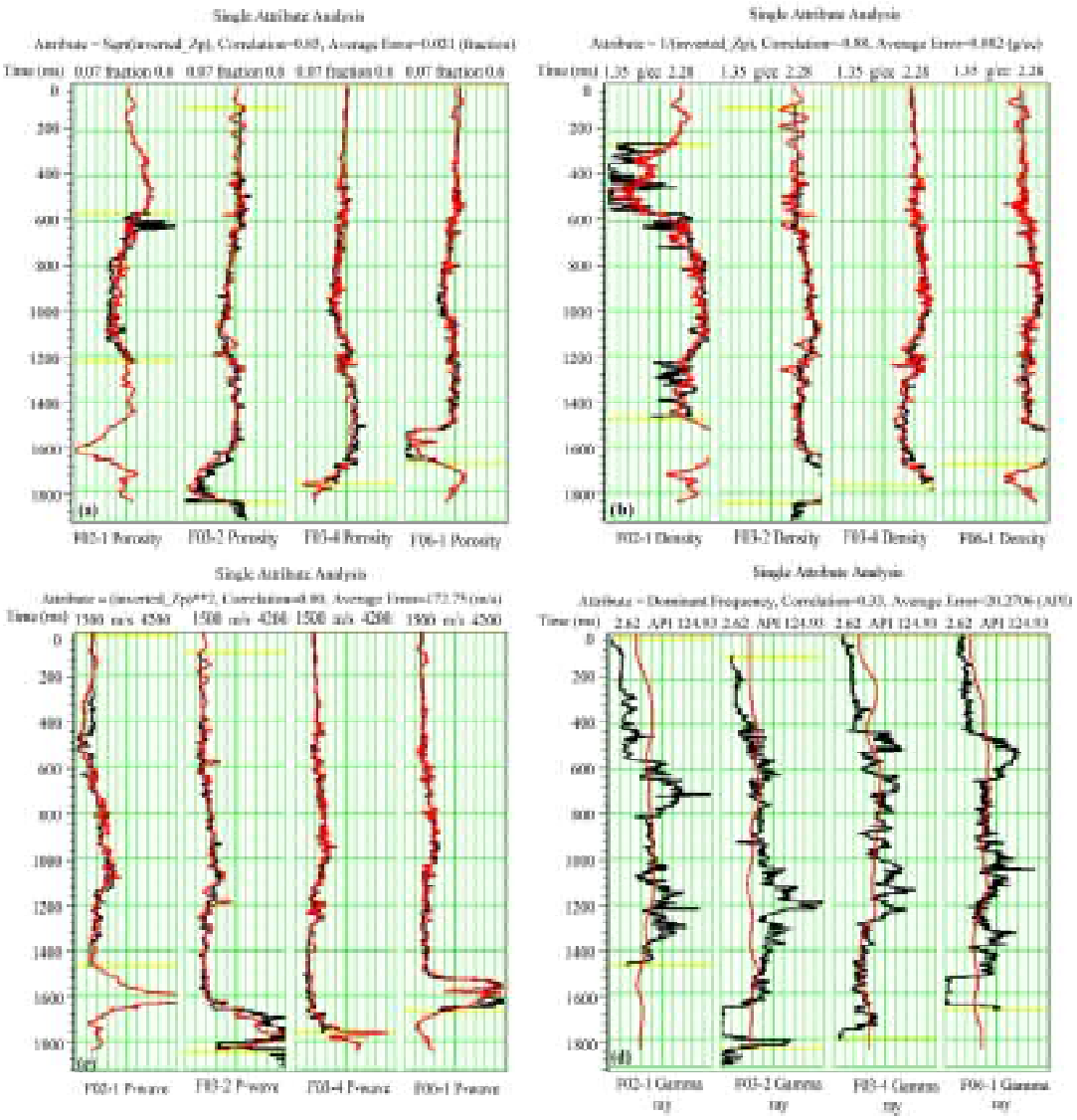

FIGURE 5.62: The well log prediction analysis using single attribute analysis technique for (a) porosity, (b) density, (c) P-wave, and (d) gamma ray

5.3.2 Multi attribute analysis technique

The input parameters for multi-attribute analysis comprise of internal (from well log and 3D seismic data) and external (from MBI derived impedance) attributes.

Fig. 5.63 shows the result of the implemented step-wise regression utilizing a 6-point convolution operator. In the figures, the Y-axis shows average error (according to the

unit of the parameter) whereas the X-axis denotes the number of attributes utilized for prediction. The red-colored curve in the figure denotes validation error curve and the black colored curve represents all well error curve. Precisely, this curve should show continuous reduction with the addition of attributes. It is also true that the multi-attribute analysis will predict better target data by adding more and more attributes. The validation error curve concludes that how many attributes are to be added. The error decreases from a theoretical perspective, with the introduction of newer attributes. However, it is observed that but can notice that by introducing the sixth attribute, the error increases. So it is decided to use five attributes for analysis. In the validation error, each point has been computed by 'hiding' each of the wells and predicting its values utilizing the operator estimated from the rest of the wells in the study region.

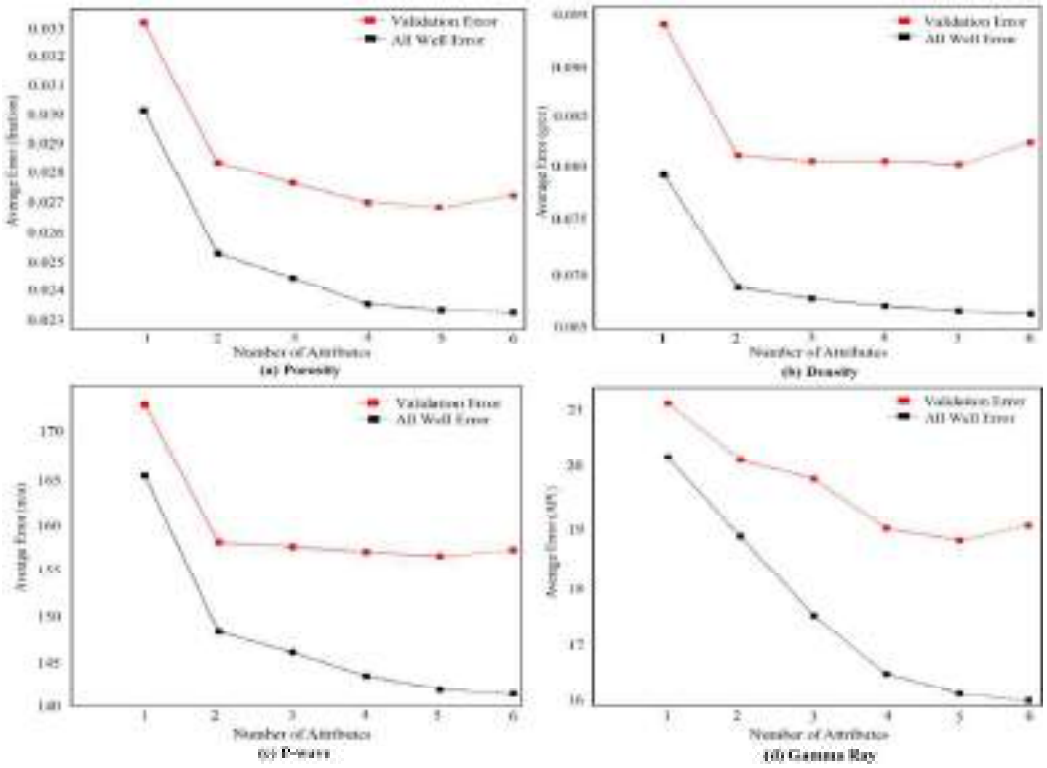

FIGURE 5.63: Graphical representation of multi attribute analysis technique derived results using 6-point convolutional operator

Figs. 5.64, 5.65, 5.66, and 5.67 show crossplot (original vs predicted) of the target log (porosity, density, P-wave and gamma ray). For the crossplot, all four wells have been

used. The X-axis represents real values and Y-axis depicts predicted values for porosity, density, P-wave and gamma ray, respectively. The correlation coefficient found to be 0.95, 0.94, 0.93 and 0.79 and corresponding error is 0.015(fraction), 0.048(g/cc), 78.44(m/s) and 13.18(API) for porosity, density, P-wave and gamma ray, respectively. The correlation coefficients derived from multi attribute analysis are very good which indicates the good performance of algorithms.

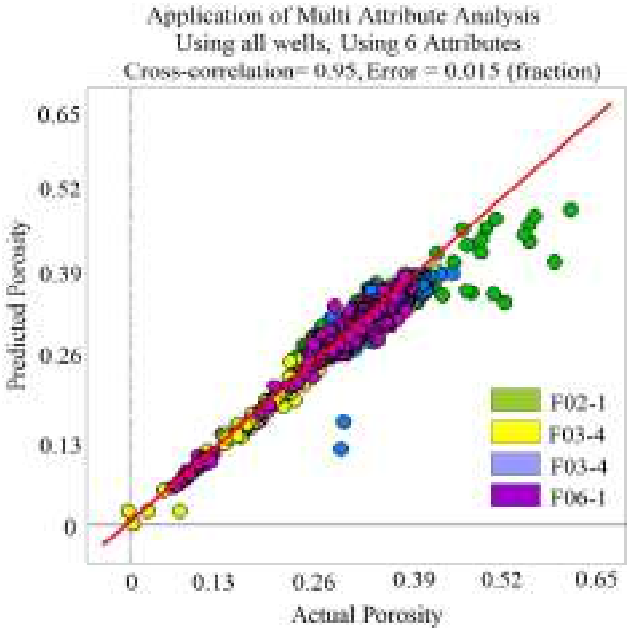

FIGURE 5.64: Crossplot between actual porosity and predicted porosity using multi attribute analysis technique

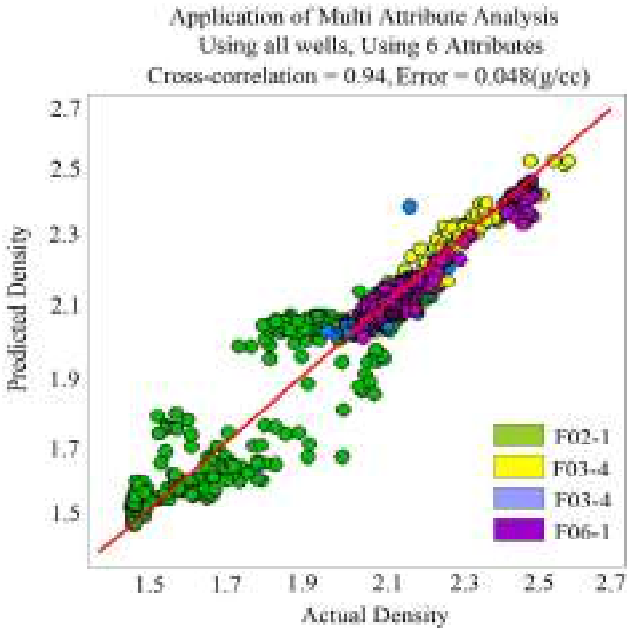

FIGURE 5.65: Crossplot between actual density and predicted density using multi attribute analysis technique

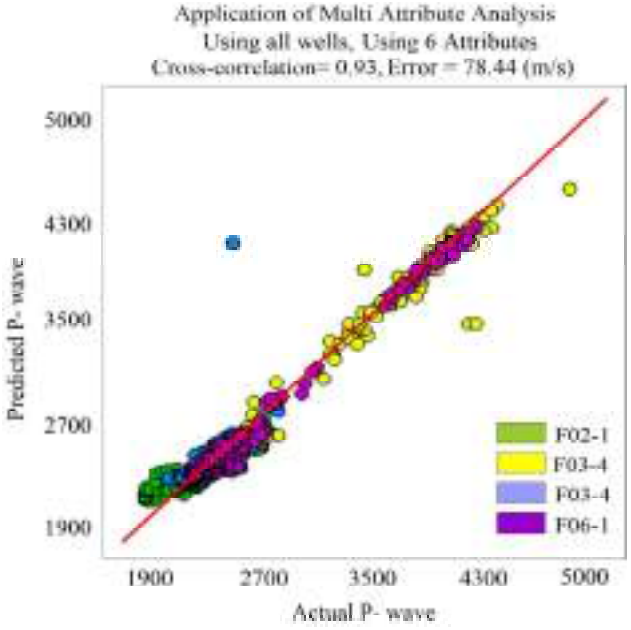

FIGURE 5.66: Crossplot between actual P-wave and predicted P-wave using multi attribute analysis technique

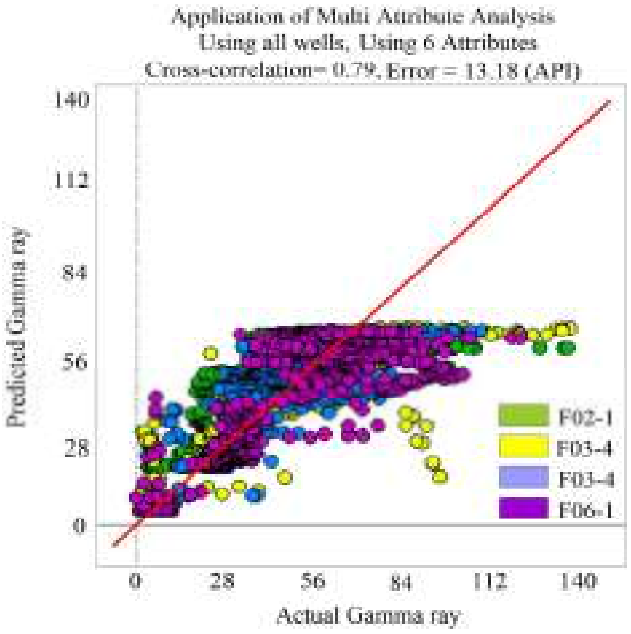

FIGURE 5.67: Crossplot between actual gamma ray and predicted gamma ray using multi attribute analysis technique

Fig. 5.68 shows the well log prediction analysis using multi attribute linear regression using MBI method for each well (F02-1, F03-2, F03-4 and F06-1), respectively, which is very important for the prediction of petrophysical parameters. The matching of original well logs with predicted well logs is very crucial for better prediction of petrophysical parameters which is clearly visible in Fig. 5.68.

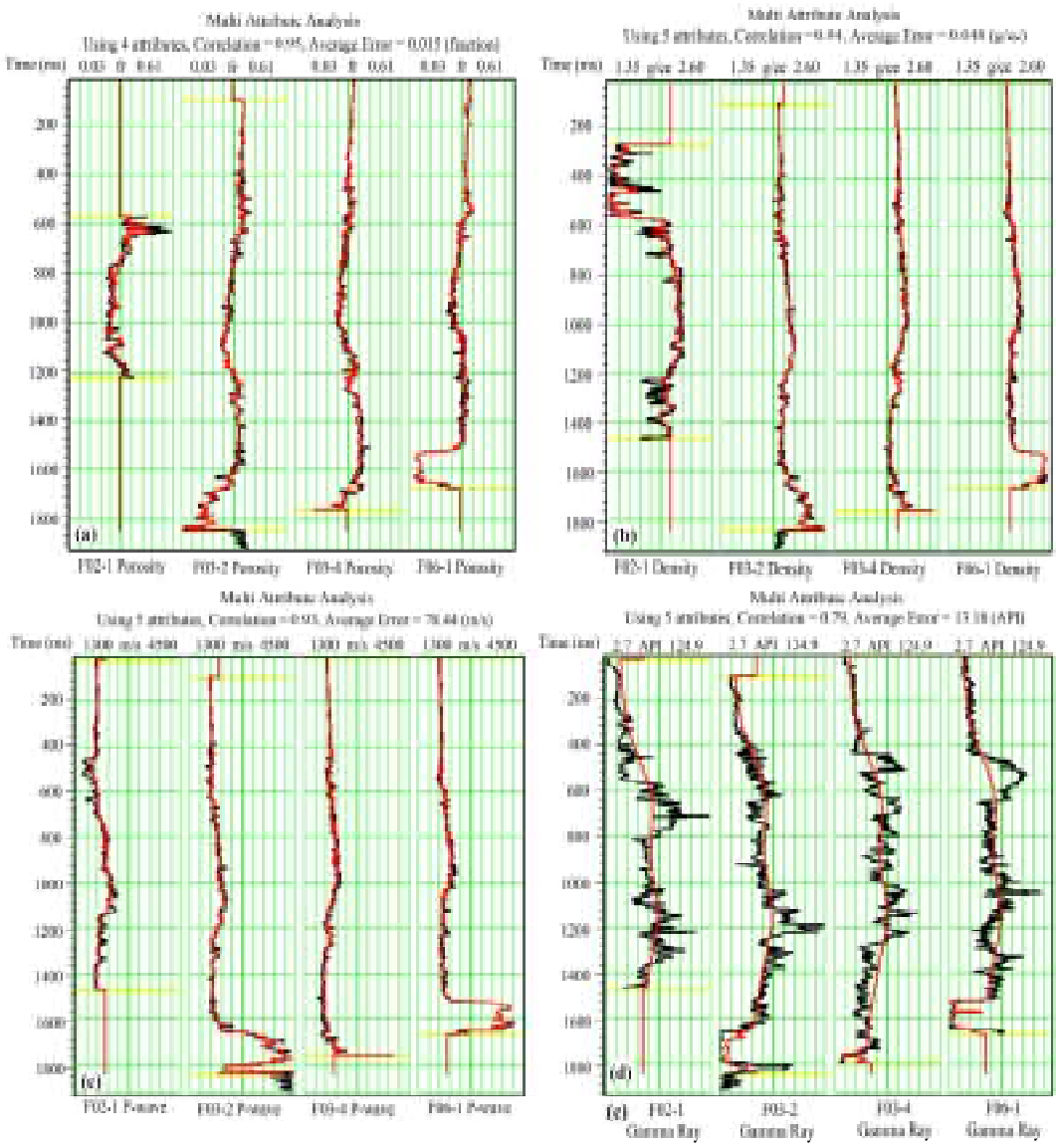

FIGURE 5.68: The well log prediction analysis using multi attribute analysis technique for (a) porosity, (b) density, (c) P-wave, and (d) gamma ray

Fig. 5.69 shows predicted volumes of porosity, density, P-wave and gamma ray using multi attribute analysis technique.

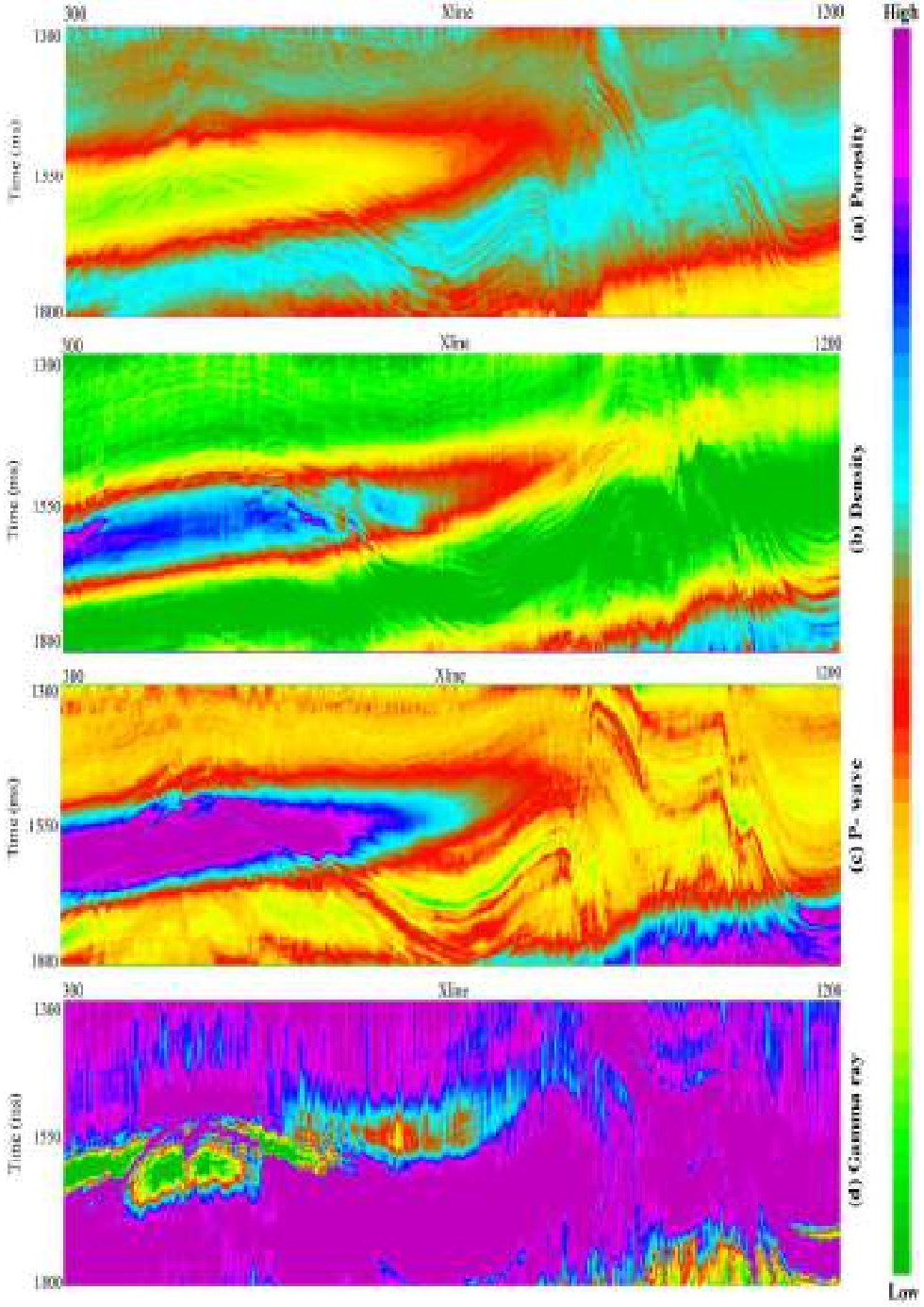

FIGURE 5.69: Cross-section of predicted (a) porosity, (b) density, (c) P-wave and (d) gamma ray using multi attribute analysis technique

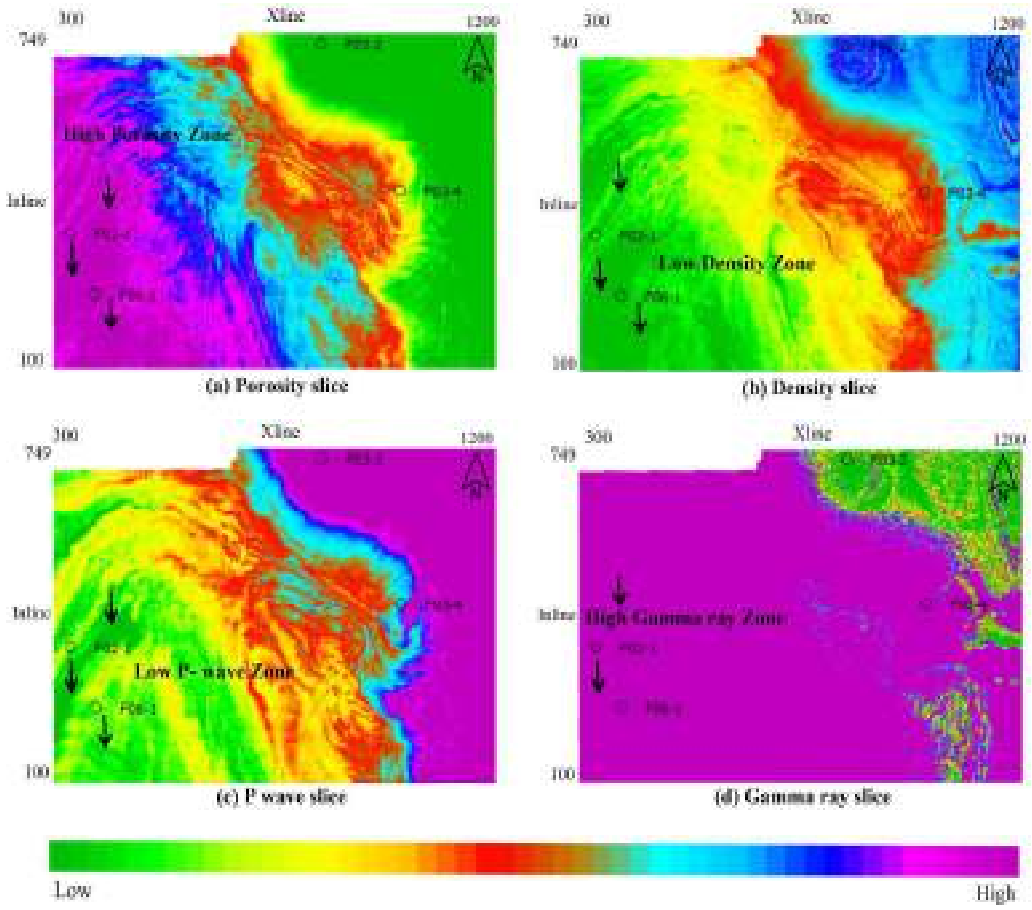

FIGURE 5.70: Predicted data slices performing multi-attribute analysis technique for (a) porosity, (b) density, (c) P wave velocity and (d) gamma ray at 1700ms time interval

Fig. 5.70 shows predicted porosity, density, P-wave and gamma ray slices at 1700ms. These slices show the horizontal distribution of predicted petrophysical parameters at a 1700ms time interval. The anomalous zone is highlighted by the arrow. From the Figs. 5.69 and 5.70 it has been noticed that the prediction results using multi-attribute analysis and MBI as an external attribute not precise for interpretation. The attributes derived from multi attribute analysis has been further used in PNN and MLFN techniques. For comparison of prediction results, PNN and MLFN with MBI derived inverted impedance as an external attribute has been used for prediction as described in the next sections.

5.3.3 Probabilistic neural network technique

PNN was performed firstly on the composite trace and then on the entire seismic volume. The data for PNN analysis was acquired from four wells in terms of porosity, density, P-wave and gamma ray logs. Furthermore, the seismic volume and inverted results of MBI have also been used in PNN based analysis. The impedance values obtained from MBI have been precisely used in PNN algorithm as an external attribute. Salient results are illustrated in Figs. 5.71- 5.74 in the form of cross-plots between the actual and predicted values for the porosity, density, P-wave and gamma ray as obtained from PNN. The Y-axis, in the cross-plots, represents predicted value and the X-axis represents actual values of the aforementioned petrophysical parameters as obtained from well log data. In the Figs. 5.71-5.74 red-colored line is the regression line. It is a line with zero intercepts and slope one which is indicative of a perfect correlation between actual and predicted attributes.

The values of cross-correlation and error for each petrophysical property as obtained from the cross-plots is tabulated in Table 5.5.

TABLE 5.5: Correlation coefficients along with error for predicted properties derived from PNN technique

Parameters	Correlation coefficient	Error
Porosity	0.97	0.0147
Density	0.96	0.046
P-wave	0.95	70.88
Gamma ray	0.82	13.05

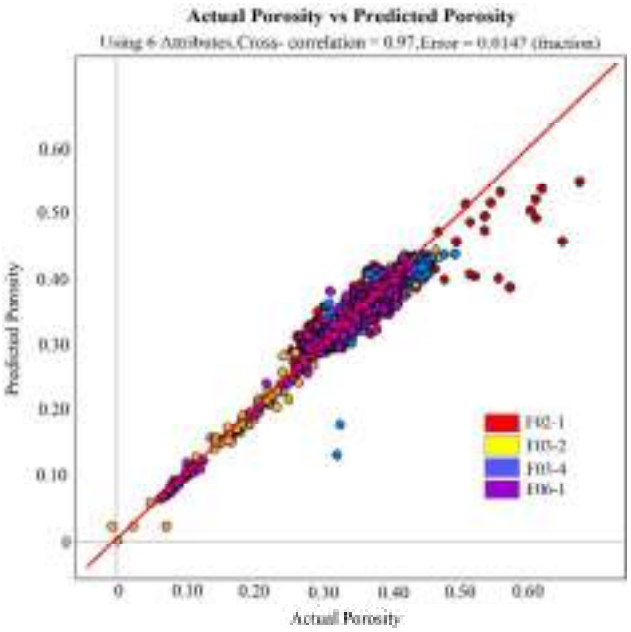

FIGURE 5.71: Crossplot between actual porosity and predicted porosity using PNN technique

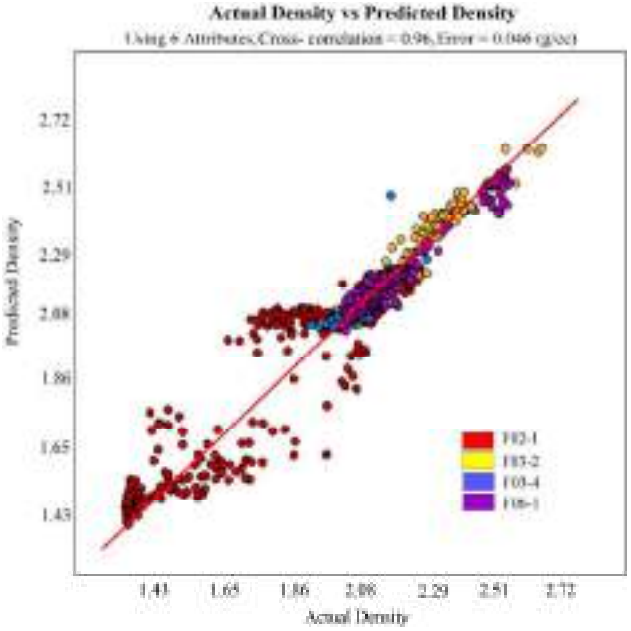

FIGURE 5.72: Crossplot between actual density and predicted density using PNN technique

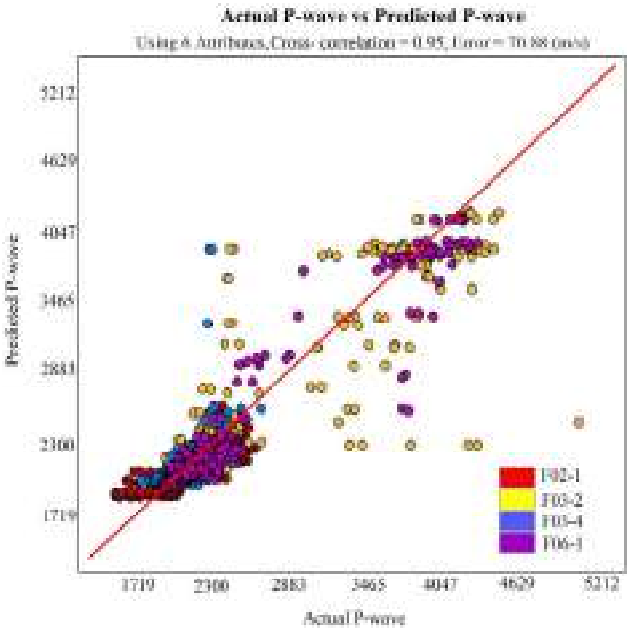

FIGURE 5.73: Crossplot between actual P-wave and predicted P-wave using PNN technique

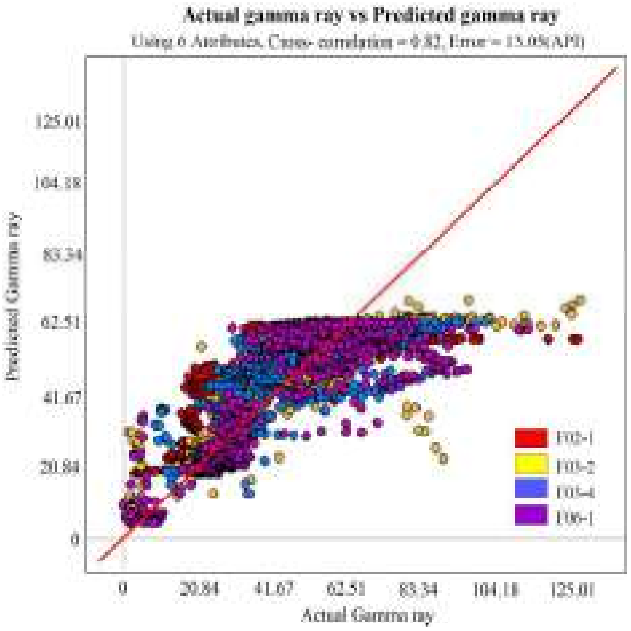

FIGURE 5.74: Crossplot between actual gamma ray and predicted gamma ray using PNN technique

The correlation coefficient values obtained from PNN technique are better for all the petrophysical parameters (porosity, density, P-wave and gamma ray) in comparison

to the multi attribute analysis using MBI impedance values as an external attribute. Therefore, it may be assumed that PNN approach performs better geostatistical analysis in comparison to multi attribute analysis.

The comparison of actual values with predicted values for porosity, density, P-wave and gamma ray logs (only for Well F03-2) obtained from PNN are also shown in Fig. 5.75.

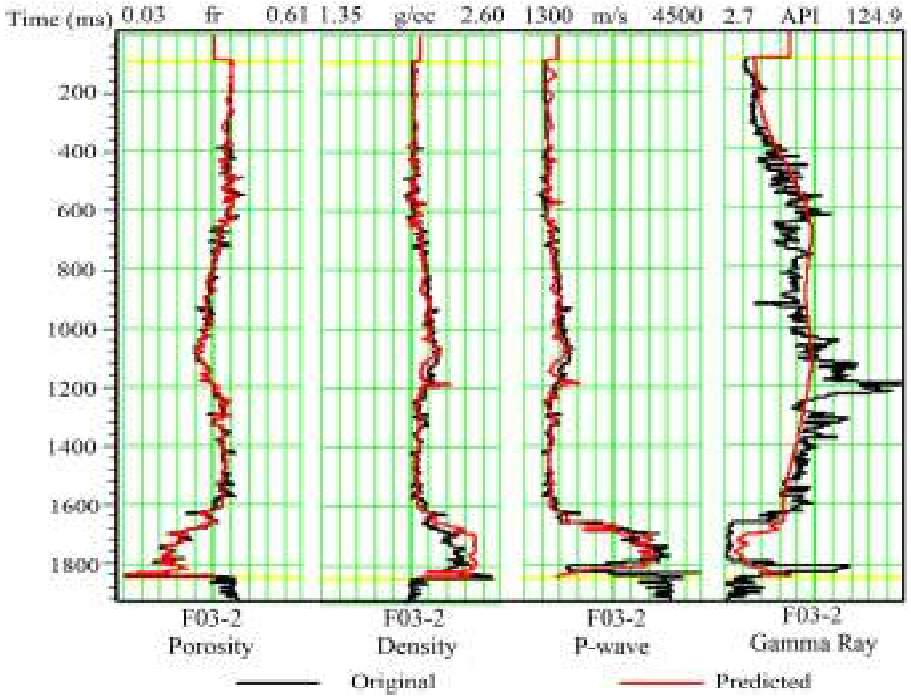

FIGURE 5.75: Prediction comparison for Well F03-2 obtained from PNN technique

The variation of the predicted porosity, density, P-wave and gamma ray by using MBI derived inverted results as external attributes are given in Figs. 5.76, 5.77, 5.78 and 5.79, respectively (only for inline 244). A close perusal of Fig. 5.76 reveals a high porosity anomaly located between 1680ms to 1700ms time intervals. The anomalies of this high porosity are visible along the Crossline 600 to Crossline 900. The low-density anomaly is visible in Fig. 5.77. The low P-wave and high gamma ray anomalies can be observed in Figs. 5.78 and 5.79, respectively. The low density, low P-wave and high gamma ray anomalies are also located between 1680ms to 1700ms time intervals like high porosity anomaly. The existence of these anomalies in the 1680-1700ms distinctly indicates the existence of a hydro-carbonaceous reservoir. The data slices at 1700ms

time interval for all the parameters are illustrated in Fig. 5.80, which is equivalent to 1680m of depth from the ground surface. The anomalous zone is clearly shown by the ellipse in Fig. 5.80. On both the vertical section and the time slice, the anomalous zone is very easy to interpret as the relevant petrophysical properties are violet-bluish in color for higher magnitudes and in greenish color for the low value of the relevant petrophysical property.

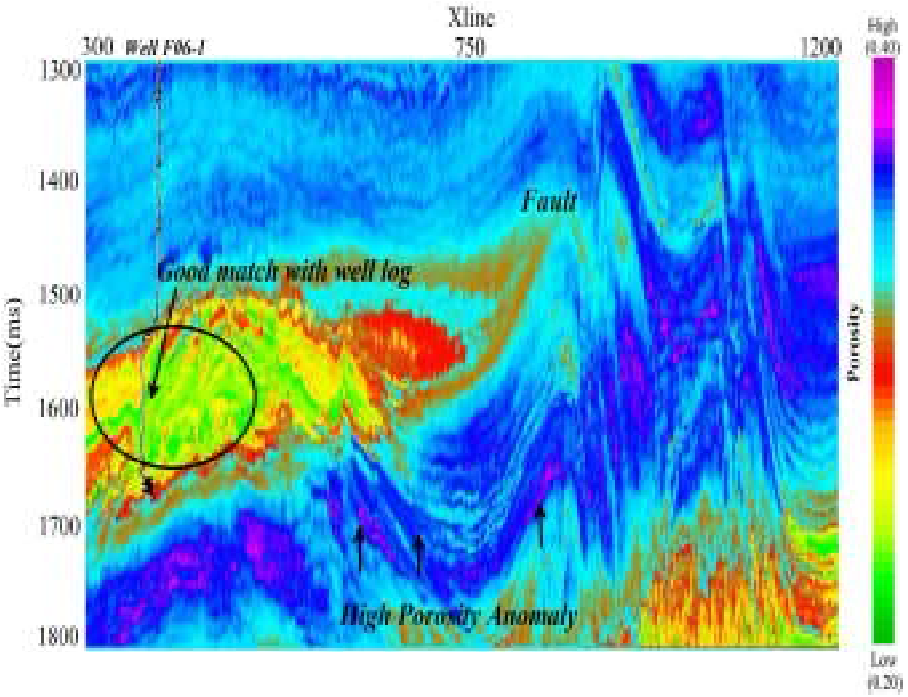

FIGURE 5.76: Porosity volume predicted by PNN technique (at inline 244)

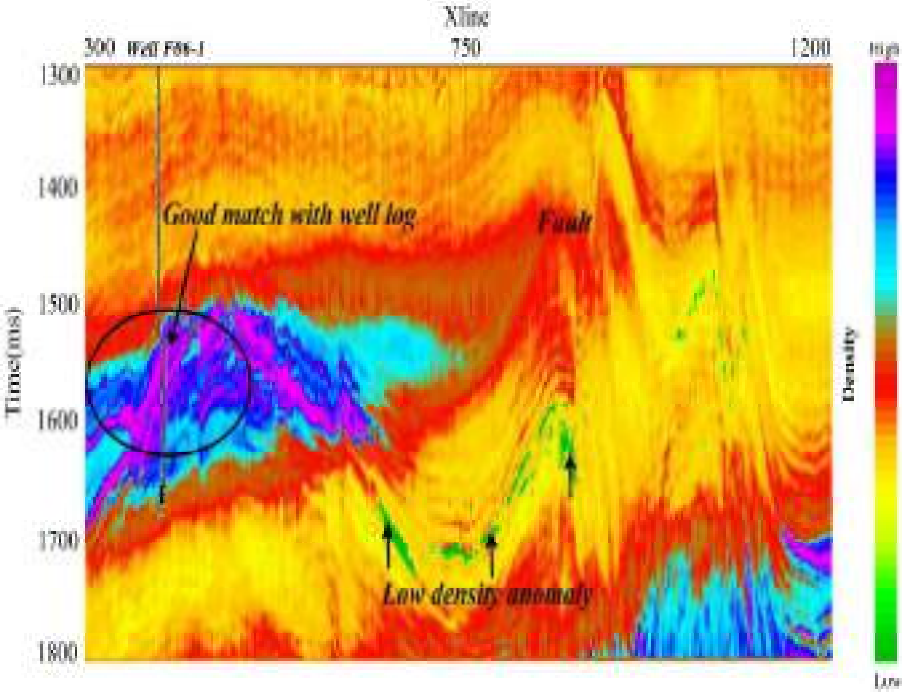

FIGURE 5.77: Density volume predicted by PNN technique (at inline 244)

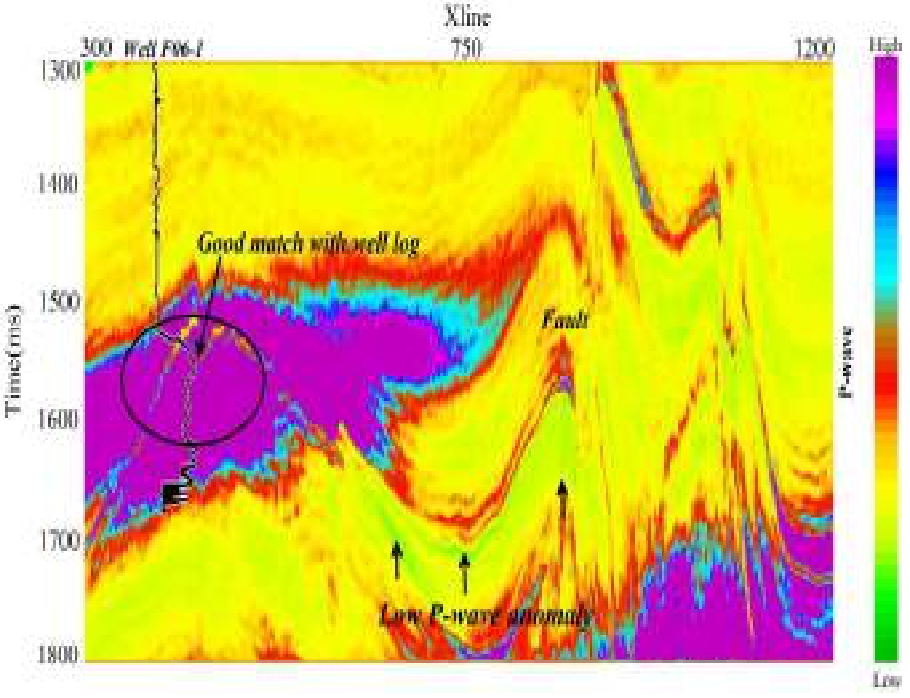

FIGURE 5.78: Predicted P-wave volume derived from PNN technique (at inline 244)

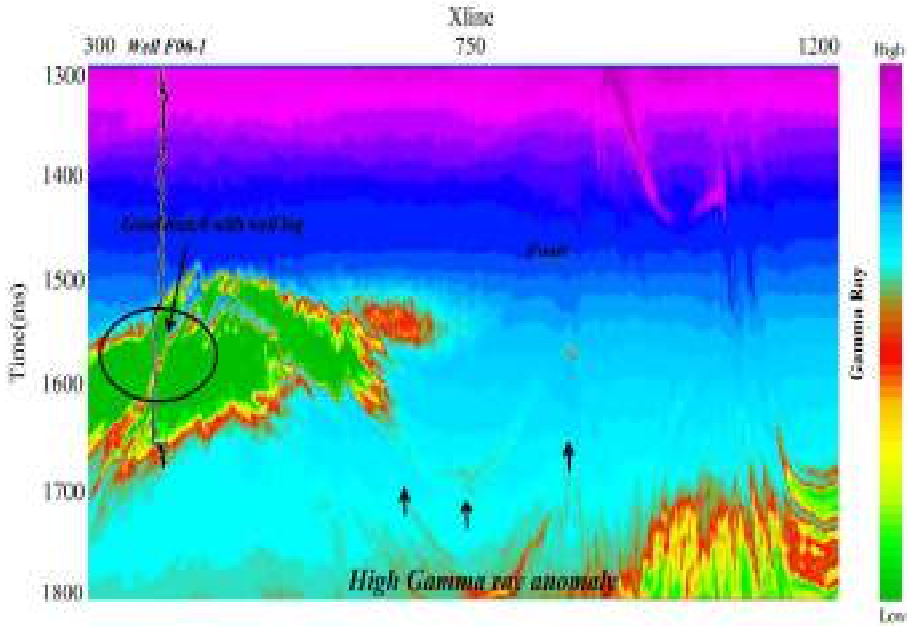

FIGURE 5.79: Predicted gamma ray volume from PNN technique (at inline 244)

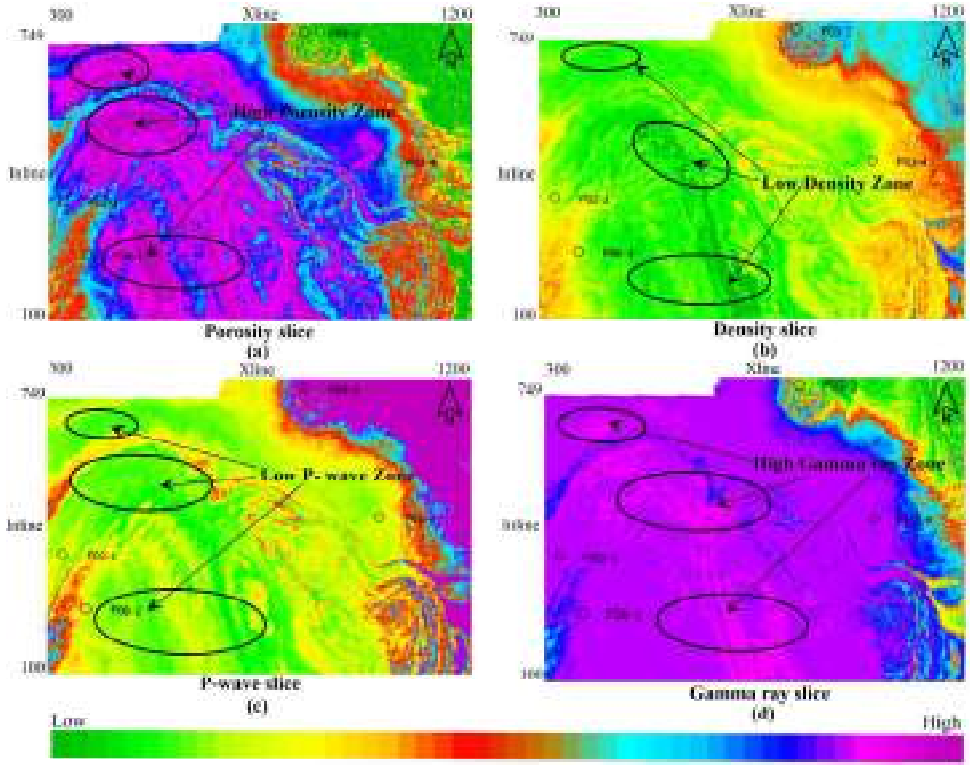

FIGURE 5.80: Predicted data slices using PNN technique for (a) porosity, (b) density, (c) P-wave and (d) gamma ray at 1700ms time interval

5.3.4 Multilinear feed forward neural network technique

The MLFN was performed firstly on the composite trace and then on the entire seismic volume. The data for the MLFN analysis was acquired from four wells in terms of porosity, density, P-wave and gamma ray logs. Furthermore, the seismic volume and inverted results of MBI have also been used in the MLFN based analysis. The impedance values obtained from MBI have been precisely used in the MLFN algorithm as an external attribute.

Salient results are illustrated in Figs. 5.81- 5.84 in the form of cross-plots between the actual and predicted values for the porosity, density, P-wave and gamma ray as obtained from MLFN. The Y-axis, in the cross-plots, represents predicted value and the X-axis represents actual values of the aforementioned petrophysical parameters as obtained from well log data. In the Figs. 5.81-5.84 red-colored line is the regression line. It is a line with zero intercepts and slope one which is indicative of a perfect correlation between actual and predicted attributes.

The values of cross-correlation and error for each petrophysical property as obtained from the cross-plots is tabulated in Table 5.6.

TABLE 5.6: Correlation coefficients along with error for predicted properties derived from MLFN technique

Parameters	Correlation coefficient	Error
Porosity	0.96	0.020
Density	0.95	0.051
P-wave	0.94	73.00
Gamma ray	0.80	13.13

The correlation coefficient values obtained from the MLFN technique are better for all the petrophysical parameters (porosity, density, P-wave and gamma ray) in comparison to the multi-attribute analysis. Therefore, it may be assumed that the MLFN approach performs better geostatistical analysis in comparison to multi attribute analysis.

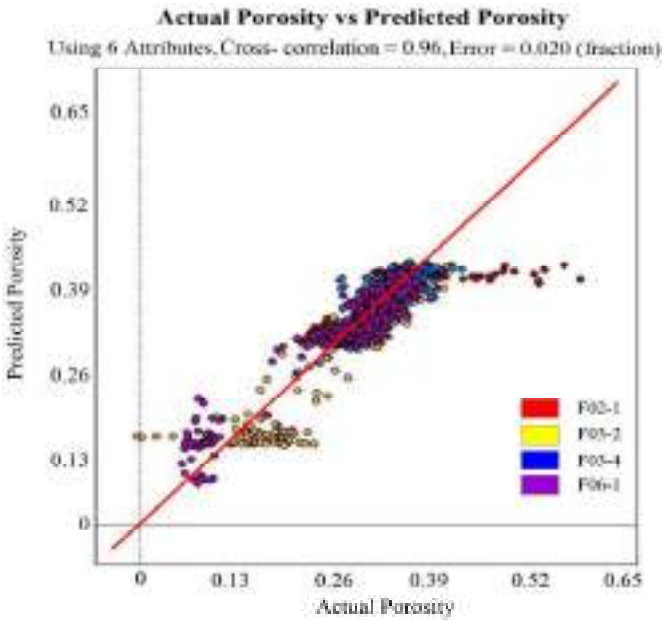

FIGURE 5.81: Crossplot between actual and predicted porosity obtained from MLFN technique

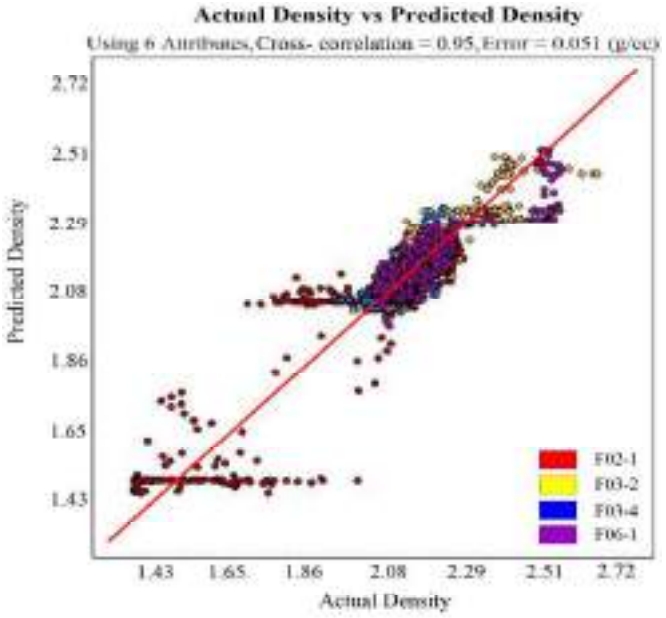

FIGURE 5.82: Crossplot between actual and predicted density obtained from MLFN technique

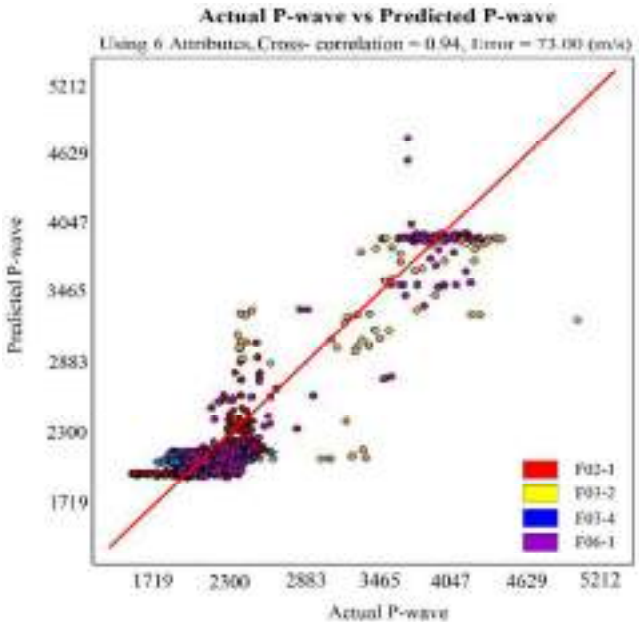

FIGURE 5.83: Crossplot between actual and predicted P-wave obtained from MLFN technique

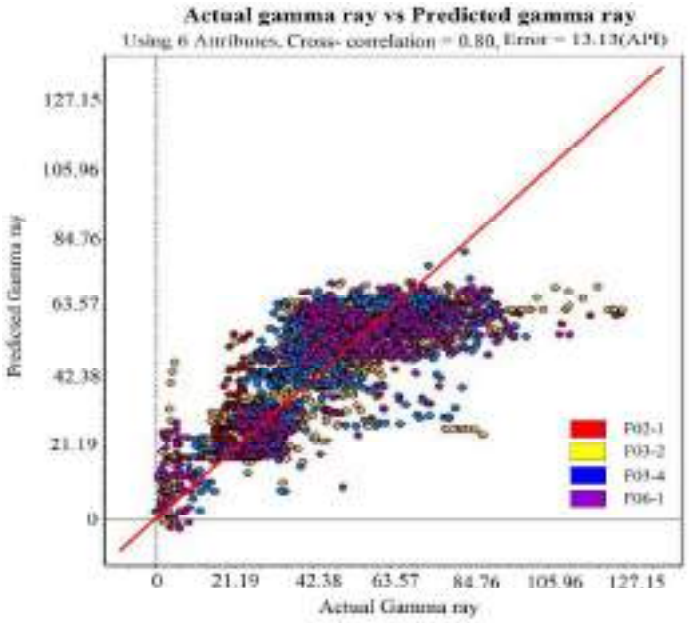

FIGURE 5.84: Crossplot between actual and predicted gamma ray obtained from MLFN technique

The variation of the predicted porosity, density, P-wave and gamma ray by using MBI derived inverted results as external attributes are given in Figs. 5.85, 5.86, 5.87 and

5.88, respectively (only for inline 244). A close perusal of Fig. 5.86 reveals a high porosity anomaly located between 1680ms to 1700ms time intervals. The anomalies of this high porosity is visible along the Crossline 600 to Crossline 900. The low-density anomaly is visible in Fig. 5.86. The low P-wave and high gamma ray anomalies can be observed in Figs. 5.87 and 5.88, respectively. The low density, low P-wave and high gamma ray anomalies are also located between 1680ms to 1700ms time intervals like high porosity anomaly. The existence of these anomalies in the 1680-1700ms distinctly indicates the existence of a hydro-carbonaceous reservoir. The data slices at 1700ms for all the parameters are illustrated in Figs. 5.89, which is equivalent to 1680m of depth from the ground surface. The anomalous zone is clearly shown by the ellipse in Fig. 5.89. On both the vertical section and the time slice, the anomalous zone is very easy to interpret as the relevant petrophysical properties are violet-bluish in color for higher magnitudes and in greenish color for the low value of the relevant petrophysical property.

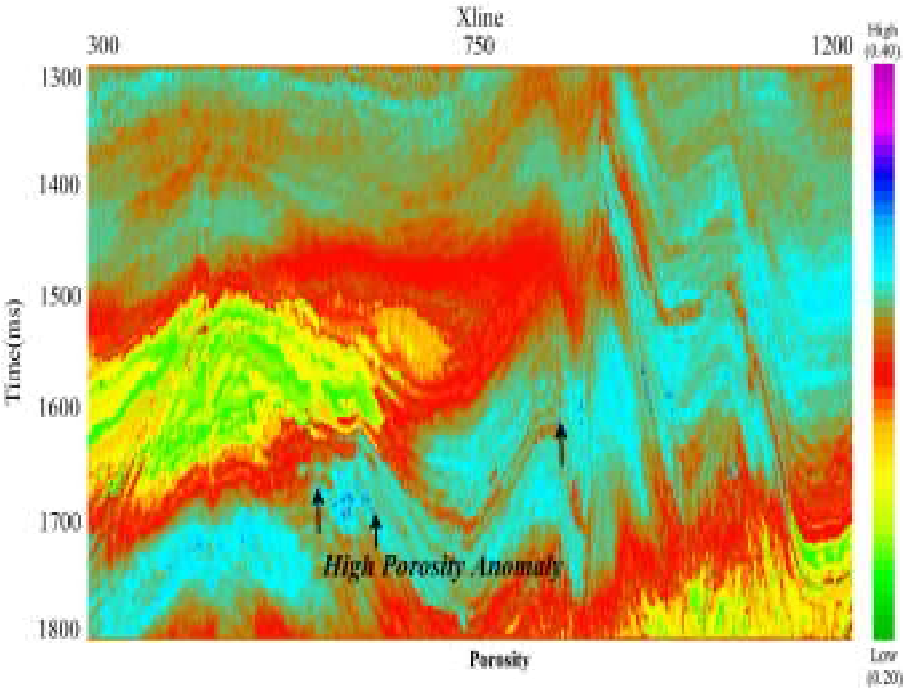

FIGURE 5.85: Predicted porosity (at Inline 244) using MLFN technique

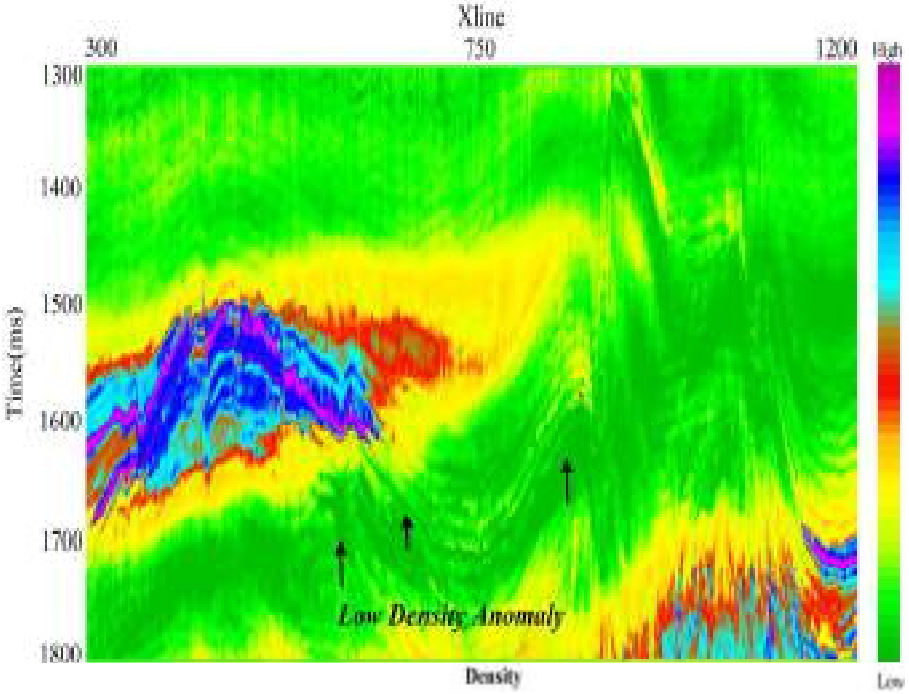

FIGURE 5.86: Predicted density (at Inline 244) using MLFN technique

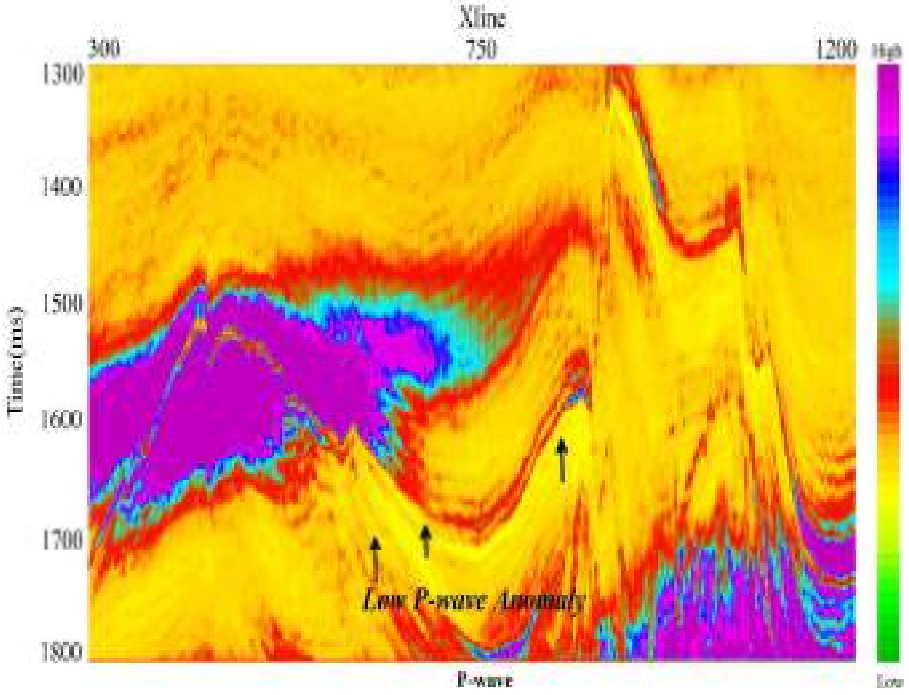

FIGURE 5.87: Predicted P-wave (at Inline 244) using MLFN technique

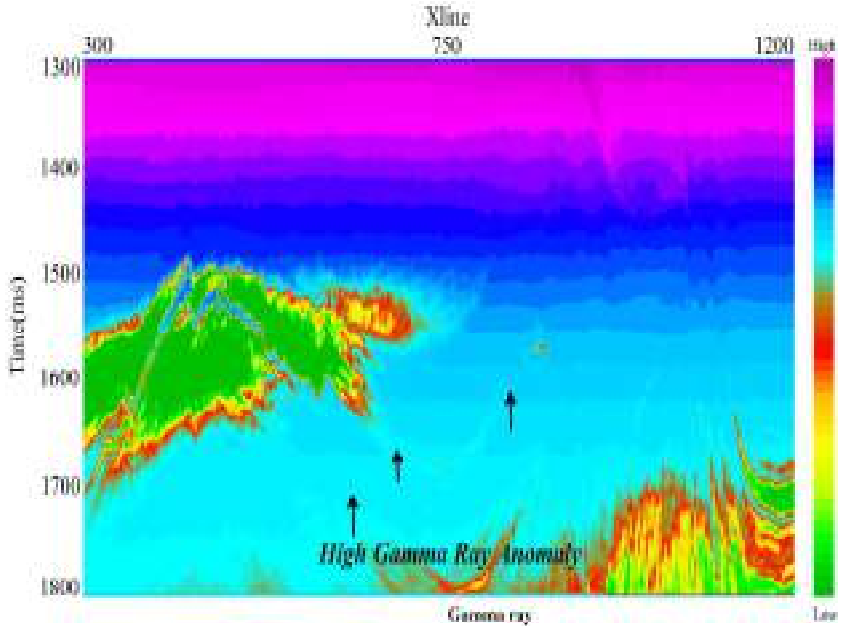

FIGURE 5.88: Predicted gamma ray (at Inline 244) using MLFN technique

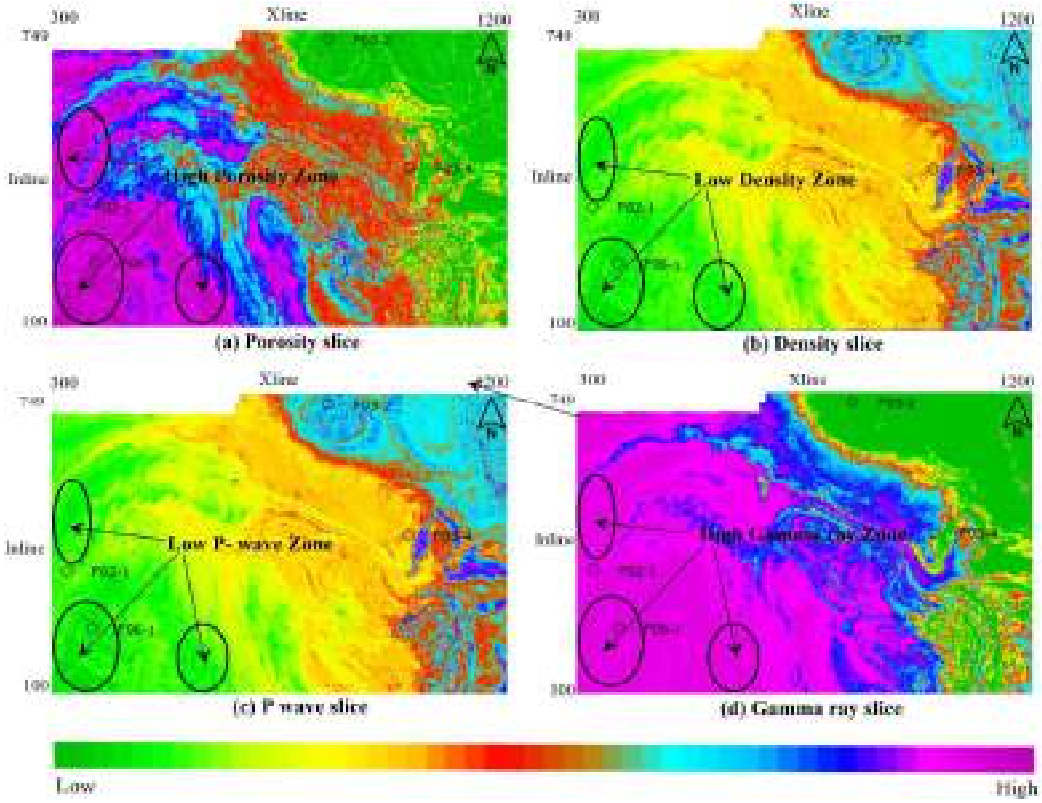

FIGURE 5.89: Predicted data slices using MLFN technique for (a) porosity, (b) density, (c) P-wave and (d) gamma ray at 1700ms time interval

The four geostatistical techniques, namely, single attribute, multi attribute analysis, PNN and MLFN to predict the porosity, density, P-wave and gamma ray volumes utilizing MBI derived results as an external attribute. The single attribute was not able to link between well log porosity and seismic attributes because the correlation coefficients are low. Cross-plots between predicted petrophysical parameters and actual petrophysical parameters performing multi-attribute analysis, PNN and MLFN reveal mutually consistent results. Using single attribute analysis, multi attribute analysis, PNN and MLFN techniques, a low-density value, high porosity values, low P-wave values and high gamma ray values indicate the existence of anomalous zone, which is found between 1680ms and 1700ms time intervals. The predicted petrophysical parameters using PNN provided more accurate results compared to multi-attribute analysis and MLFN methods when MBI derived impedance is used as an external attribute.

5.4 Verification of results

The results obtained from post-stack inversion methods and geostatistical techniques for F3 block, the Netherlands, have clearly revealed that various methods and techniques used in the present research work provide appropriate findings for the existence of reservoir between 1680ms to 1700ms time intervals. This time interval zone is equivalent to 1680m of the depth of occurrence of the reservoir, from the ground surface. The horizontal and vertical extents of the reservoir have been determined from the inline and crossline. The reservoir exists from inlines 200 to 300 and from crosslines 630 to 880. Therefore, the horizontal extent of the reservoir in inline and crossline directions may be estimated as 3687m and 4445m, respectively.

The internet resources and geological studies (de Jager and Geluk, 2007) also stated the presence of accumulation of oil and gas in the F3 block of the Netherlands. However, the resources and references have not stated anything about the extent of this reservoir. Also, the presence of fault plane as established in this block, by the present research work finds a clear mention in the geological studies by various authors in their

books (Kabaca, 2018; Wong et al., 2007; De Bruin and Bouanga, 2007; Wolak et al., 2013).

Furthermore, the porosity values of the rock mass in this research have been found to be varying from 0.20 to 0.40 (fraction), which is equivalent to the porosity values predicted by Mojeddifar et al. (2015) for F3 block, the Netherlands by using different prediction methods.

For the Penobscot field, Canada, various methods used in the estimation of petrophysical properties of this field have been unable to detect any reservoir present in the study area. Not one but a good number of methods and techniques have provided the basis for concluding this fact unanimously after critically examining the petrophysical properties provided by each technique and method. Nevertheless, due to limitations on data availability between inlines 1200 to 1400 and cross lines 1161 to 1200, the results may be considered to be specific to this zone only. The presence of the reservoir in the other part of the Penobscot region, beyond the study region, cannot be ruled out.